Hydroacoustic Modeling of a Cavitation Vortex Rope for a Francis Turbine

THÈSE N^{O} 6547 (2015)

PRÉSENTÉE LE 17 AVRIL 2015
À LA FACULTÉ DES SCIENCES ET TECHNIQUES DE L'INGÉNIEUR
LABORATOIRE DE MACHINES HYDRAULIQUES
PROGRAMME DOCTORAL EN ENERGIE

ÉCOLE POLYTECHNIQUE FÉDÉRALE DE LAUSANNE

POUR L'OBTENTION DU GRADE DE DOCTEUR ÈS SCIENCES

PAR

Christian LANDRY

acceptée sur proposition du jury:

Prof. J. R. Thome, président du jury
Prof. F. Avellan, directeur de thèse
Dr A. Bergant, rapporteur
Dr J. Koutnik, rapporteur
Prof. A. Schleiss, rapporteur

ÉCOLE POLYTECHNIQUE
FÉDÉRALE DE LAUSANNE

Suisse
2015

Energy and persistence conquer all things.
— Benjamin Franklin

Acknowledgements

I would first like to thank the members of the jury, Prof. John Thome, Prof. François Avellan, Prof. Anton Schleiss, Dr Jiri Koutnik and Dr Anton Bergant for their valuable time and inspiring comments during the private defense. This thesis was realized thanks to financial support of The Ark, the foundation for innovation of Valais Canton, through the project HydroVS, as well as the European Commission (HYPERBOLE research project, ERC/FP7-ENERGY-2013-1-Grant 608532). I would like also to acknowledge all the partners of the HYPERBOLE research project for the constructive discussions during the past two years.

Pour la suite des remerciements, je me permets de poursuivre en français. Tout d'abord, je souhaite remercier mon directeur de thèse, Prof. François Avellan, pour son encadrement et sa disponibilité tout au long de ma thèse. Il m'a offert l'opportunité unique d'associer la recherche expérimentale au développement de modèles numériques. Je le remercie aussi sincèrement de m'avoir permis de présenter mes travaux lors de multiples congrès internationaux et d'échanger des points de vue avec les principaux constructeurs de machines hydrauliques.

Je souhaite ensuite exprimer toute ma gratitude à toutes les équipes du laboratoire sans qui rien n'aurait été possible et avec qui j'ai eu beaucoup de plaisir à travailler. Tout d'abord, un merci tout particulier à Isabelle Stoudmann-Schmutz pour son aide précieuse dans le monde tumultueux de l'administration et des notes de frais.

Je remercie également tous les mécaniciens: Victor Rivas, David Buzzi, Christian Sierro, Louis Vina, dirigés successivement par Louis Besançon et Maxime Raton. Cette équipe de professionnels n'a jamais rechigné à la tâche, malgré un agenda très variable durant les campagnes expérimentales. Un merci tout particulier à Maxime pour ses éternelles phrases "d'encouragement" durant ma thèse et son "intérêt" non dissimulé pour le Valais. Je remercie aussi Victor et David pour les parties de beach-volley (parfois périlleuses) et les traditionnelles grillades estivales.

Ensuite, je tiens aussi à remercier tous les membres du bureau d'étude encadré par Philippe Cerrutti : Vincent Berruex, Philippe Faucherre et Alain Renaud. Ils ont permis l'élaboration et la mise en place du système d'excitation présenté dans ce document.

De plus, les différentes campagnes expérimentales n'auraient pas été possibles sans l'équipe d'ingénieurs d'essai dirigée par Henri-Pascal Mombelli et composée d'Ambrosio Acal, Alberto Bullani, Sébastien Bourgeois, Lillie Croft et Monica Suarez. Un merci tout particulier à Georges Crittin pour son aide inestimable durant les campagnes de mesure. Quel que soit le problème, ses compétences en électronique et en hydraulique ont toujours permis de trouver des solutions, même dans les situations les plus inextricables.

Je remercie également toutes les personnes ayant contribué au développement de SIMSEN et plus particulièrement Dr Christophe Nicolet et Dr Sébastien Alligné pour leurs conseils avisés tout au long de ma thèse et leur éternelle disponibilité. Cette thèse n'aurait pas été possible sans l'excellent travail qu'ils ont fourni en amont. Leur bienveillance et leur expérience se sont aussi étendues hors du laboratoire, lors de jeudredis arrosés ou de soirées post-conférences endiablées. Un grand merci aussi à Philippe Allenbach pour avoir intégré de nouveaux modèles numériques dans SIMSEN et grandement réduit mes temps de calcul en facilitant la communication avec Matlab.

La réalisation de cette thèse fut aussi possible grâce à la formidable ambiance qui réside entre les doctorants, toutes générations confondues. C'est pourquoi je souhaite aussi remercier tous mes collègues doctorants que j'ai côtoyés durant 4 ans. Merci à Dr Cécile Alligné-Münch, Dr Steven Roth et Dr Vlad Hasmatuchi, les anciens locataires du plus beau bureau du laboratoire pour leurs conseils avisés dès mon arrivée au labo. Maintenant, ce sanctuaire a été repris par la nouvelle génération de post-doc, Audrey et Loïc. Je remercie particulièrement ce dernier pour son talent artistique dans la réalisation de collines de rendement.

Merci à Martino, notre ex-chef cuisinier et le MacGyver du labo. Ce fut un plaisir de partager le bureau avec toi. Ta *playlist* musicale m'a souvent donné la force de persévérer lors de journées déprimantes. Merci aussi à Matthieu, le second locataire du bureau. Ton imagination débordante dans le monde du *mobbing* m'a permis de développer un esprit machiavélique et d'améliorer mes aptitudes dans le lancer d'élastiques et la construction de catapulte. Je te remercie d'avoir essayé de m'instruire à la vraie musique après des années de torture sur les toits de suisse-romande, mais aussi pour ton soutien durant la phase de rédaction.

Merci à Christian Vessaz, notre fonctionnaire vaudois pure souche. Malgré ton talent incontestable au fourneau, j'ai étonnement réussi à garder un poids stable tout au long de la thèse. Ce fut un véritable plaisir d'avoir parcouru toutes mes études à l'EPFL avec toi. Je garderai toujours à l'esprit nos parties de cartes, de puissance quatre et les escapades dans la Broye. Je te souhaite bonne chance au Canada où, je l'espère, tu pourras réaliser ton rêve. Merci à Andres, notre tour opérateur suisse-allemand. Je garderai toujours à l'esprit la seconde signification des acronymes LMH et LDV, engendrant une nouvelle tradition le vendredi qui pimentait bien les pauses café. Ce fut toujours un plaisir de travailler avec toi et j'espère arriver un jour à te faire prononcer une phrase positive sur le beau canton du Valais. Merci à Arthur, notre futur écrivain. Ce fut un plaisir de préparer la campagne expérimentale de

2013 avec toi et je te remercie encore pour l'idée de la vanne rotative. Cette illumination a grandement bouleversé cette thèse. Merci à Olivier, notre coach sportif en volley-ball, pour ton éternelle bonne humeur. Ton aisance durant les présentations restera toujours un exemple à suivre. Je remercie Marc, notre fribourgeois hyperactif, pour toutes les discussions sur le tennis durant les pauses café. Merci à Ebrahim, notre iranien fan de raclette. Je remercie aussi Keita d'avoir préparé la campagne expérimentale de 2015 avec Arthur. Merci à Elena, notre italienne végétarienne. Je te souhaite bonne chance pour ta thèse et j'attends toujours avec impatience un prosciutto. Merci aussi à la nouvelle génération: Simon Pasche, Outi Supponen, Quentin Fabien et Emmanuel Dorel. J'ai vraiment apprécié nos discussions à la cafétéria ou sur la passerelle.

De plus, la vie d'un doctorant ne s'arrête pas aux murs du laboratoire. Je remercie Jérémy Binder, Pierre-Alain Blanc et Axel Brunk pour nos jeudredis inoubliables et nos escapades dans les capitales européennes. Je remercie aussi mes amis de toujours, Fabien, Hervé, Romain, Antoine et Mathieu pour ces nouvels ans épiques, les cours de vulgarisation sur la terrasse du *Great* et vos encouragements inconditionnels durant toutes ces années. Je remercie aussi mes collègues de master pour les fameux apéros du lundi, la découverte d'Etna Pizza et les fêtes de Noël inoubliables.

Finalement, je souhaite aussi remercier mes parents, Jean-Claude et Denise, pour leur soutien perpétuel et indépendant de mes choix de carrière. Je remercie également mes deux sœurs, Marie-Claude et Chantal, pour leurs encouragements et leur bienveillance depuis bientôt 30 ans.

Lausanne, 20 Mars 2015 Christian Landry

Abstract

The stochastic nature of renewable energy resources has a significant impact on the balance between energy generation and consumption in current power systems. The most typical instances are solar and wind power, which are both heavily influenced by weather conditions. Therefore, to enable the energy balancing process, it is necessary to ensure power plants have enough storage capacity as well as primary and secondary grid control capabilities. Pumped storage power plants are able to store large amounts of electricity with a full cycle of pumping and generation, which may achieve unrivaled efficiencies above 80%. Additionally, hydropower plants are offering the advantage of exploiting renewable primary source energy with hardly any emission of greenhouse gas. Thus, in Europe, hydraulic turbines and pump-turbines are key components in energy conversion technologies, achieving both load balancing tasks, and primary and secondary power network control. Nevertheless, frequent changes of power generation by the renewable energy resources is directly impacting the required operating range of hydro units. During operation of hydraulic turbines and pump-turbines over a large operating range, high levels of vibrations and large fluctuations of pressure and power are likely to occur. As a consequence, life expectancy of the hydraulic machinery may be significantly reduced, eventually leading to the loss of structural integrity.

Hydraulic machines subject to off-design operation involve the presence of cavitating flow regimes in the draft tube. The cavitation vortex rope at part load conditions is described as an excitation source for the hydraulic system, and interactions between this excitation source and system eigenfrequency may result in resonance phenomena and induce a draft tube surge and electrical power swings. To accurately predict and simulate a part load resonance, proper modeling of the draft tube is critical. The presence of this cavitation vortex rope requires a numerical pipe element taking into account the complexity of the two-phase flow. Among the parameters describing the numerical model of the cavitating draft tube flow, three hydroacoustic parameters require a special attention. The first hydroacoustic parameter is called cavitation compliance. This dynamic parameter represents the variation of the cavitation volume with respect to a variation of pressure and implicitly defines the local wave speed in the draft tube. The second parameter corresponds to the bulk viscosity and is related to internal processes breaking a thermodynamic equilibrium between the cavitation volume and the surrounding liquid. The third parameter is the excitation source induced by the precessing vortex rope.

The methodology to identify these hydroacoustic parameters is based on the direct link that exists between the natural frequency of the hydraulic system and the wave speed in the draft tube. First, the natural frequency is identified with the help of an external excitation system. Then, the wave speed is determined thanks to an accurate numerical model of the experimental hydraulic system. By applying this identification procedure for different values of Thoma number, it is possible to quantify the cavitation compliance and the void fraction of the cavitation vortex rope. In order to determine the energy dissipation induced by the cavitation volume, the experimental hydraulic system is excited at the natural frequency. With a Pressure-Time method, the amount of excitation energy is quantified and is injected into the numerical model. A spectral analysis of the forced harmonic response is used to identify the bulk viscosity and the pressure source induced by vortex rope precession.

Thus, the identification of the hydroacoustic parameters requires the development of a new numerical draft tube model taking into account the divergent geometry and the convective terms of the momentum equation. Different numerical draft tube models are compared to determine the impact of convective and divergent geometry terms on identification of the hydroacoustic parameters. Furthermore, to predict the hydroacoustic parameters for non-studied operating conditions and to break free from the dependence upon the level setting of the Francis turbine, dimensionless numbers are proposed. They have the advantage of being independent from the selected numerical model and they define a behavior law of hydroacoustic parameters when the cavitation volume oscillates at resonance operating conditions.

Finally, to investigate the stability operation of the prototype, the hydroacoustic parameters need to be transposed to the prototype conditions according to transposition laws. By assuming both Thoma similitude and Froude similitude conditions, transposition laws are developed and the hydroacoustic parameters are predicted for the prototype. This study is part of the *HYPERBOLE* collaborative research project in association with the world major turbine manufacturers. The transposition of the experimental measurements of the reduced-scale physical model will be compared against the real generating unit located in a hydropower plant in the Canadian province of British Columbia.

Keywords: Francis turbine, Draft tube flow, Cavitation vortex rope, Hydroacoustic modeling, Experimental investigation

Résumé

La nature stochastique des énergies renouvelables a un impact significatif sur la régulation des réseaux électriques. Les énergies solaire et éolienne, largement influencées par les conditions météorologiques, en sont des exemples éloquents. Ainsi, afin de garantir la stabilité du réseau électrique soumis à des variations imprévisibles de puissance, il devient nécessaire de s'assurer que certaines centrales électriques possèdent des capacités suffisantes de stockage d'énergie et de réglage du réseau électrique. Pour exemple, les centrales de pompage-turbinage sont en mesure de stocker une large quantité d'énergie électrique, tout en garantissant un rendement de cycle de pompage-turbinage pouvant être supérieur à 80%. De plus, les centrales hydrauliques offrent l'avantage d'exploiter une source d'énergie renouvelable, sans quasiment émettre aucune émission de gaz à effet de serre. Par conséquent, en Europe, les machines hydrauliques sont devenues des composants technologiques majeurs dans la conversion d'énergie. Cependant, les fréquentes variations de puissance imposées par les énergies renouvelables influencent directement la gamme de fonctionnement des centrales hydrauliques. Ces nouvelles conditions d'exploitation hors-nominales peuvent engendrer de fortes vibrations et de larges fluctuations de pression et de puissance pouvant réduire significativement l'espérance de vie de la machine hydraulique.

Les machines hydrauliques sujettes à des conditions d'exploitation hors-nominales engendrent l'apparition d'écoulements cavitants dans l'aspirateur. La torche de cavitation à charge partielle peut être décrite comme une source d'excitation pour le système hydraulique et des interactions entre cette source d'excitation et la fréquence propre du système peuvent induire un phénomène de résonance et engendrer de grandes fluctuations de puissance sur le réseau électrique. Pour prédire et simuler avec précision un phénomène de résonance à charge partielle, la modélisation de l'aspirateur est critique. En effet, la présence d'une torche de cavitation requiert un modèle numérique prenant en compte la complexité d'un écoulement diphasique. Parmi les paramètres caractérisant la torche de cavitation, trois paramètres hydroacoustiques requièrent une attention toute particulière. Le premier modélise la variation du volume de cavitation en fonction de la pression et définit implicitement la vitesse d'onde locale dans l'aspirateur. Le deuxième décrit un amortissement représentant la dissipation d'énergie lors d'un changement de phase entre le liquide et le gaz. Finalement, le troisième modélise la source de pression induite par la précession de la torche de cavitation dans l'aspirateur.

La méthodologie pour identifier ces trois paramètres hydroacoustiques est fondée sur le lien direct qui existe entre la fréquence propre du système hydraulique et la vitesse d'onde dans l'aspirateur. Par conséquent, la première étape de cette méthodologie consiste à identifier la fréquence propre à l'aide d'un système d'excitation externe. Puis, la vitesse d'onde est déterminée grâce à un modèle numérique précis modélisant le système hydraulique étudié. En appliquant cette procédure d'identification pour plusieurs nombres de Thoma, il est possible de quantifier le volume de la torche de cavitation et le taux de vide associé. La seconde étape de cette méthodologie consiste à identifier la dissipation d'énergie induite par le volume de cavitation en excitant le système hydraulique à sa fréquence propre. Avec une méthode analytique, la quantité d'énergie excitant le système est quantifiée et injectée dans le modèle numérique. Une analyse spectrale de la réponse forcée harmonique est finalement utilisée pour identifier l'amortissement et la source de pression induite par la précession de la torche de cavitation.

Ainsi, l'identification des paramètres hydroacoustiques requiert le développement d'un système d'excitation externe et d'un modèle numérique précis du système hydraulique étudié. Dans ce document, différents modèles numériques de l'aspirateur ont été comparés afin de déterminer l'impact du terme convectif et de la géométrie divergente de l'aspirateur présent dans l'équation de quantité de mouvement sur l'identification des paramètres hydroacoustiques. En outre, pour prédire ces paramètres pour des conditions d'exploitation non-étudiées et pour outrepasser la dépendance intrinsèque des résultats avec l'implémentation de la turbine hydraulique, des nombres adimensionnels sont proposés pour chaque paramètre. Ces nombres adimensionnels possèdent l'avantage d'être indépendants du modèle numérique choisi. De plus, ils permettent de définir des lois de comportement des paramètres hydroacoustiques nécessaires pour la simulation dynamique de phénomènes non-linéaires.

Finalement, pour déterminer la stabilité du prototype, les paramètres hydroacoustiques doivent être transposés à l'aide de lois de similitudes. En admettant des valeurs du nombre de Thoma et du nombre de Froude similaires entre le prototype et le modèle réduit, des lois de similitude sont développées et les paramètres hydroacoustiques sont prédits à l'échelle prototype. En outre, cette étude a été développée dans le cadre d'un projet européen, nommé *HYPERBOLE*, en collaboration avec les grands constructeurs de turbines hydrauliques. La transposition des mesures expérimentales obtenues en laboratoire pourra alors être comparée avec les données réelles d'une centrale hydraulique localisée dans la province de Colombie britannique au Canada afin de valider les lois de similitude.

Mots clefs : Turbine Francis, Écoulement diphasique, Torche de cavitation, Modélisation hydroacoustique, Étude expérimentale

Contents

Cover page i

Acknowledgements i

Abstract (English/Français) v

List of figures xiii

List of tables xvii

Nomenclature xix

1 Introduction 1
- 1.1 Current energy context 1
- 1.2 Off-design operating condition of hydraulic machines 2
  - 1.2.1 Part load condition 4
  - 1.2.2 Full load condition 5
- 1.3 State of the art 5
- 1.4 Thesis objective 8
- 1.5 Document structure 9

2 Cavitation vortex rope modeling **11**
- 2.1 One-dimensional hydroacoustic equations 11
  - 2.1.1 The axial momentum equation 12
  - 2.1.2 The continuity equation 14
- 2.2 Equivalent electrical scheme representation 17
- 2.3 Summary and discussion 20

3 Methodology for identification of hydroacoustic parameters **21**
- 3.1 Analytical analysis of a simplified hydraulic system 22
- 3.2 Experimental identification of the natural frequency 24
- 3.3 Experimental identification of wave speed 24
- 3.4 Experimental identification of bulk viscosity 26
  - 3.4.1 Pressure-Time method 27
- 3.5 Experimental identification of the pressure source 28

3.6 Description of the identification algorithm 30
  3.6.1 Algorithm for wave speed and bulk viscosity 30
  3.6.2 Algorithm for the pressure source 34
3.7 Summary and discussion 35

4 Experimental Instrumentation Setup **37**
4.1 Model Testing Facilities 37
4.2 Pressure Measurements Instrumentation 38
4.3 Overview of pressure fluctuations 38
4.4 Excitation system 41
  4.4.1 Design of the excitation system 41
  4.4.2 Characterization of the rotating valve 42
  4.4.3 Test rig excitation 46
4.5 Summary and discussion 47

5 Test rig hydroacoustic model **49**
5.1 Viscoelastic pipe model without cavitation 49
5.2 Francis turbine runner model 52
5.3 Spiral casing model 53
5.4 Energy losses model 54
5.5 Validation of the test rig hydroacoustic model for a steady flow 55
5.6 Summary and discussion 57

6 Identification of the hydroacoustic parameters **59**
6.1 Identification of wave speed 59
  6.1.1 Computation of cavitation volume 60
  6.1.2 Validation of void fraction 61
  6.1.3 Development of a dimensionless parameter for wave speed 63
6.2 Identification of bulk viscosity 66
  6.2.1 Influence of the degassing procedure on harmonic response 67
  6.2.2 Development of a dimensionless parameter for bulk viscosity 67
6.3 Identification of pressure source 74
  6.3.1 Study of standard deviation *e* of pressure source 75
  6.3.2 Study of pressure source location *L* 77
  6.3.3 Study of pressure source amplitude *A* 78
6.4 Simulation at resonance operating condition 82
6.5 Comparison of different draft tube models 84
  6.5.1 Model influence on wave speed 85
  6.5.2 Model influence on bulk viscosity 85
  6.5.3 Model influence on the pressure source 86
  6.5.4 Model influence on void fraction 86
  6.5.5 Model influence on dimensionless wave speed 86
  6.5.6 Model influence on dimensionless bulk viscosity 88

6.6 Transposition to the prototype 89
    6.6.1 Similitude law of wave speed 89
    6.6.2 Similitude law of bulk viscosity 90
    6.6.3 Similitude law of the pressure source 91
6.7 Summary and discussion 92

7 Simplified methodology for identification of the hydroacoustic parameters 95

7.1 Hydroacoustic model 96
7.2 Test installation 97
7.3 Acquisition and processing of the data 97
7.4 Test procedures 98

8 Conclusions and Perspectives 101

8.1 Conclusions 101
8.2 Perspectives 103

A Hill chart of the reduced-scale model 105

B Dynamic pressure sensors location 107

Bibliography 113

Curriculum Vitae 115

List of Figures

1.1 Structure of electricity production in 2012. 2
1.2 Mean annual growth rates 2002-2012. 2
1.3 Cavitation vortex rope in a Francis turbine. 3
1.4 Reference altitudes on a Francis turbine outline. 4
1.5 Velocity triangles at turbine outlet for partial, BEP and full load operations. . . 5

2.1 Balances of forces for the momentum equation (Left) and overlapping of momentum and continuity control volumes (Right) 12
2.2 Representation of the draft tube with a cavitation vortex rope and its equivalent circuit 20

3.1 Representation of the simplified hydraulic system. 22
3.2 Equivalent circuit of the simplified hydraulic system. 22
3.3 Setup for the visualisation of the cavitation vortex rope, synchronized with acquisition from pressure sensors. 26
3.4 Representation of the Gaussian curve (Left) and the axis along the draft tube (Right). 29
3.5 Behavior of the natural frequency as a function of wave speed (Left) and bulk viscosity (Right). 31
3.6 Error on the natural frequency as a function of wave speed and bulk viscosity. . 32
3.7 Error on the forced harmonic response as a function of bulk viscosity. 33
3.8 Synoptic scheme of the algorithm to identify wave speed and bulk viscosity. . . 34
3.9 Synoptic scheme of the genetic algorithm used to identify the pressure source. 35

4.1 EPFL test rig PF3 drawn with the excitation system and locations of dynamic pressure sensors. 37
4.2 Close view of the draft tube. 39
4.3 Cross spectral density function of the *P1* and *C1N* pressure sensors at $\sigma = 0.11$ and Fr = 8.75 over loads ranging from of 40% to 120%. 39
4.4 Evolution of vortex rope precession as a function of discharge factor Q_{ED} for a Froude number Fr = 8.75. 40
4.5 CAD model of the excitation system. 41
4.6 Side view of EPFL test rig PF4. 42
4.7 Rotating valve of the excitation system. 43

4.8 Location of measurement sections on EPFL test rig PF4. 43
4.9 Experimental characteristic curve of the rotating valve. 44
4.10 Location of the flush-mounted pressure sensors on EPFL test rig PF4. 45
4.11 Comparison of cross spectral density functions from experimental data and numerical values, at excitation frequency equal to 2.75 Hz. 45
4.12 Cross spectral density function of *P1* and *ES1* pressure sensors, divided by the one-sided autospectral density function of the reference sensor *P1* located at the turbine inlet. 46
4.13 The hydraulic response on EPFL test rig PF3 for first and second eigenmodes. . 47
4.14 Evolution of natural frequency as a function of Thoma number for operating conditions *PL1* and *PL2*. 48

5.1 Viscoelastic pipe model without cavitation. 52
5.2 Francis turbine runner model. 52
5.3 Spiral casing modeled by seven viscoelastic pipes. 53
5.4 Measurement locations in the spiral casing. 54
5.5 Wave speed evolution along the angular position of the spiral casing. 55
5.6 Layout of EPFL test rig PF3 modeled with the SIMSEN software. 56

6.1 Evolution of wave speed as a function of Thoma number (Left) or void fraction (Right) for different Froude numbers. 60
6.2 Evolution of cavitation compliance as a function of the Thoma number for different Froude numbers. 61
6.3 Comparison between mean void fraction computed analytically and local void fraction determined with a high-speed visualization. 63
6.4 Evolution of pressure and vortex rope volume for $Q_{ED} = 0.128$ and Fr = 8.75 at the resonance operating condition. 64
6.5 Draft tube evolution of dimensionless wave speed as a function of void fraction β. 65
6.6 Evolution of the dimensionless wave speed in the draft tube as a function of void fraction β. 66
6.7 Comparison of experimental and numerical responses to an excitation source for different second viscosities at operating point *PL1*, Fr = 6.56 and $\sigma = 0.08$. . 67
6.8 Comparison of forced harmonic response for different wave speeds a_{PF} on the test rig at the operating point *PL2*, Fr = 7.66 and $\sigma = 0.13$. 68
6.9 Evolution of dimensionless bulk viscosity as a function of Thoma number. . . . 69
6.10 Evolution of dimensionless bulk viscosity as a function of the void fraction. . . 69
6.11 Evolution of dimensionless bulk viscosity as a function of the void fraction. . . 70
6.12 Comparison between experimental and numerical forced harmonic responses for the operating condition *PL1* at natural frequency 72
6.13 Comparison between experimental and numerical forced harmonic responses for the operating condition *PL2* at the natural frequency 73
6.14 Global error as a function of pressure source location L and standard deviation e. 75
6.15 Amplitude of the pressure source as a function of pressure source location L. . 76

6.16 Error for all Thoma numbers as a function of pressure source location L. 76
6.17 Global error for $e = 0.03$ m as a function of pressure source location L. 77
6.18 Representation of the Gaussian curve (Left) and x-axis along the draft tube (Right). 77
6.19 Evolution of amplitude as a function of pressure source location L. 78
6.20 Evolution of amplitude A as a function of the Thoma number. 79
6.21 Evolution of dimensionless amplitude as a function of Thoma number. 79
6.22 Comparison between experimental and numerical forced harmonic responses for the operating condition *PL1* at vortex rope frequency $f_{\text{Vortex rope}} = 2.563$ Hz 80
6.23 Comparison between experimental and numerical forced harmonic responses for the operating condition *PL1* at vortex rope frequency $f_{\text{Vortex rope}} = 2.930$ Hz 81
6.24 Time evolution of the hydroacoustic parameters. 82
6.25 Comparison between the experimental data and the numerical values at resonance operating condition. 83
6.26 Model influence on wave speed. 85
6.27 Model influence on bulk viscosity. 86
6.28 Model influence on the pressure source with a standard deviation $e = 0.03$ for the operating condition *PL1* and a Froude number $\mathrm{Fr} = 6.56$. 87
6.29 Model influence on void fraction. 87
6.30 Model influence on dimensionless wave speed. 88
6.31 Model influence on the dimensionless bulk viscosity. 89

7.1 Methodology developed for assessing pressure fluctuations experienced by hydraulic power plant. 96

A.1 Hill chart of the reduced-scale Francis turbine physical model on the EPFL test rig PF3 as a function of n_{ED} and Q_{ED} 105

B.1 Location of the dynamic pressure sensors on the EPFL test rig PF3. 107

List of Tables

4.1 Piezoresistive pressure sensors characteristics. 38
4.2 Selected Francis turbine operating conditions. 40

5.1 Comparison of experimental and numerical results for a steady flow. 56

6.1 Selected Francis turbine operating points for high-speed visualization analysis. 62
6.2 Summary of pressure source information. 82
6.3 Transposition of the hydroacoustic parameters for operating condition *PL1*. . . 92

Nomenclature

Acronyms

BEP	Best Efficiency Point
EPFL	École polytechnique fédérale de Lausanne
EU	European Union
FHR	Force Harmonic Response
FL	Full Load
IEC	International Electrotechnical Commission
LMH	Laboratoire de machines hydrauliques
LDV	Laser Doppler Velocimetry
NPSE	Net Positive Suction Head
OP	Operating Point
PIV	Particle Image Velocimetry
PL	Part Load

Latin letters

a	Wave speed	$[\mathrm{m \cdot s^{-1}}]$
A	Amplitude of the Gaussian curve	[m]
A	Constant	[-]
A	Cross-section	$[\mathrm{m^2}]$
B	Constant	[-]
C	Absolute flow velocity	$[\mathrm{m \cdot s^{-1}}]$
C	Compliance	$[\mathrm{m^2}]$
C_m	Meridional velocity component	$[\mathrm{m \cdot s^{-1}}]$
C_u	Peripheral component of the absolute flow velocity	$[\mathrm{m \cdot s^{-1}}]$
D	Pipe diameter	[m]
e	Pipe thickness	[m]
e	Standard deviation of the Gaussian curve	[m]
e	Strain rate tensor	$[\mathrm{s^{-1}}]$
E	Specific turbine energy	$[\mathrm{J \cdot kg^{-1}}]$
E	Young modulus	[Pa]

f	Force	[N]
f	Frequency	[s^{-1}]
g	Gravitational acceleration	[$\mathrm{m} \cdot \mathrm{s}^{-2}$]
h	Piezometric head	[m]
h_s	Level setting	[m]
$H_{D,v}$	Velocity head	[m]
H_{turb}	Turbine head	[m]
J_{turb}	Rotational inertia	[$\mathrm{kg} \cdot \mathrm{m}^2$]
J_u	Diffusion term	[s^{-2}]
k	Vitkovský friction coefficient	[-]
K_x	Cross-section expansion rate	[m]
K_v	Singular specific energy loss coefficient	[-]
L	Hydraulic inductance	[$\mathrm{s}^2 \cdot \mathrm{m}^{-2}$]
L	Length	[m]
L	Location of the center of the pressure source	[m]
m	Mass	[kg]
n	Runner revolution per second	[s^{-1}]
p	Static pressure	[Pa]
p_v	Saturation vapor pressure	[Pa]
Q	Discharge	[$\mathrm{m}^3 \cdot \mathrm{s}^{-1}$]
R	Ideal gas constant	[$\mathrm{J} \cdot \mathrm{mol}^{-1} \cdot \mathrm{K}^{-1}$]
R	Pipe radius	[m]
R_d	Hydraulic divergent resistance	[$\mathrm{s} \cdot \mathrm{m}^{-2}$]
R_{ve}	Viscoelastic resistance	[$\mathrm{s} \cdot \mathrm{m}^{-2}$]
R_λ	Hydraulic resistance	[$\mathrm{s} \cdot \mathrm{m}^{-2}$]
R_μ	Thermodynamic resistance	[$\mathrm{s} \cdot \mathrm{m}^{-2}$]
S_h	Pressure source	[m]
T	Water temperature	[K]
T	Torque	[$\mathrm{N} \cdot \mathrm{m}$]
U	Peripheral flow velocity	[$\mathrm{m} \cdot \mathrm{s}^{-1}$]
V	Volume	[m^3]
W	Relative flow velocity	[$\mathrm{m} \cdot \mathrm{s}^{-1}$]
Z	Elevation	[m]

Greek letters

α	Absolute flow angle	[°]
β	Relative flow angle	[°]
β	Void fraction	[-]
ϵ	Rotational speed gain factor	[$\mathrm{m}^2 \cdot \mathrm{s}$]
ζ	Relative damping	[-]
θ	Relaxation time	[s]

λ	Local loss coefficient	[-]
μ	Dynamic viscosity	$[\mathrm{Pa}\cdot\mathrm{s}]$
μ'	Second viscosity	$[\mathrm{Pa}\cdot\mathrm{s}]$
μ''	Bulk viscosity	$[\mathrm{Pa}\cdot\mathrm{s}]$
ν	Kinematic viscosity	$[\mathrm{m}^2\cdot\mathrm{s}^{-1}]$
ρ	Density	$[\mathrm{kg}\cdot\mathrm{m}^{-3}]$
σ	Thoma number	[-]
τ_{rx}	Tangential viscous stresses	[Pa]
τ_{xx}	Normal stresses	[Pa]
χ	Mass flow gain factor	[s]
ω	Angular velocity	$[\mathrm{rad}\cdot\mathrm{s}^{-1}]$

Subscripts

0	Without cavitation
1	Runner inlet reference section
$\bar{1}$	Runner outlet reference section
I	Machine high pressure section
$\bar{I}$	Machine low pressure section
$\bar{B}$	Tail water reservoir reference section
c	Cavitation
DTM	Draft tube model
exp	Experimental
L	Liquid
num	Numerical
p	Pipe wall
ref	Reference section
$visco$	Viscoelastic model
w	Water
β	Void fraction

Superscripts

$\bar{y}$	Mean part
$\tilde{y}$	Fluctuating part
M	Referred to reduced-scale physical model
P	Referred to full-scale prototype

Non-dimensional variables

Fr	Froude number	$Fr = \sqrt{\frac{E}{gD_{ref}}}$
M”	Dimensionless bulk viscosity	$\mathrm{M”} = \frac{\mu'' f_{natural}}{p_{Outlet} - p_v}$
n_{ED}	Speed factor	$n_{ED} = \frac{nD_{ref}}{\sqrt{E}}$
Q_{ED}	Discharge factor	$Q_{ED} = \frac{Q}{D_{ref}^2\sqrt{E}}$
Re	Reynolds number	$Re = \frac{CD_{ref}}{\nu}$
β	Void fraction	$\beta = \frac{V_c}{V_{tot}}$
ν	Specific speed	$\nu = \frac{\omega\sqrt{Q}}{\sqrt{\pi}(2E)^{\frac{3}{4}}}$
χ_E	Cavitation factor	$\chi_E = \frac{p_{\bar{\imath}x} - p_v}{\rho_w E}$
Π	Dimensionless wave speed	$\Pi = \frac{\rho_w a^2}{p_{Outlet} - p_v}$

1 Introduction

1.1 Current energy context

In recent years, energy policies have led to a transition where a massive penetration of alternative renewable energies and a broad deployment of energy efficiency technologies have occurred. For instance, the European Union (EU) has recently defined three major goals under the *2020 climate and energy package* [1] set of legislations:

- A 20% reduction in EU greenhouse gas emissions from 1990 levels,
- Raising the share of EU energy consumption produced from renewable resources to 20%,
- A 20% improvement in the EU's energy efficiency.

Political will has therefore increased gross electricity production from renewable sources by 1739 TWh between 2002 and 2012, and passed the threshold of 20 % share of the total output in 2012. Fossil energy remained the baseload of global electricity production with more than two-thirds of the total output, see Figure 1.1 [2]. Hydropower aside, renewable electricity increased by 3 percentage points in its share of global electricity production, rising from a 1.6% contribution in 2002 to 4.6% in 2012. A detailed bar chart illustrated in Figure 1.2 reveals that the best mean annual growth over the same period was performed by the solar sector (50.6%).

However, the stochastic nature of the renewable energy production directly impacts the energy balance between generation and consumption. The most typical instances are solar and wind power, which are both heavily influenced by weather conditions. In order to maintain balanced production at any time, it has to be ensured the grid has sufficient reserve capacity, as well as primary and secondary control capabilities. Both gas-fired and hydropower plants present the abilities for flexible generation of peak power and regulation ancillary services at a large scale. Still, hydropower plants can boast of harnessing a primary source of renewable energy

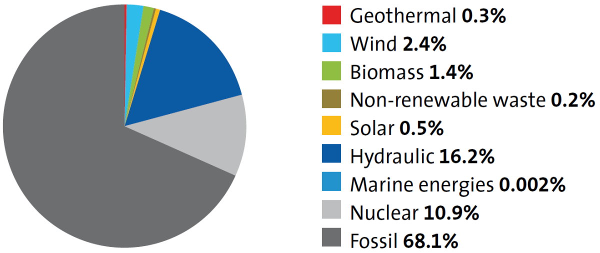

Figure 1.1: Structure of electricity production in 2012.

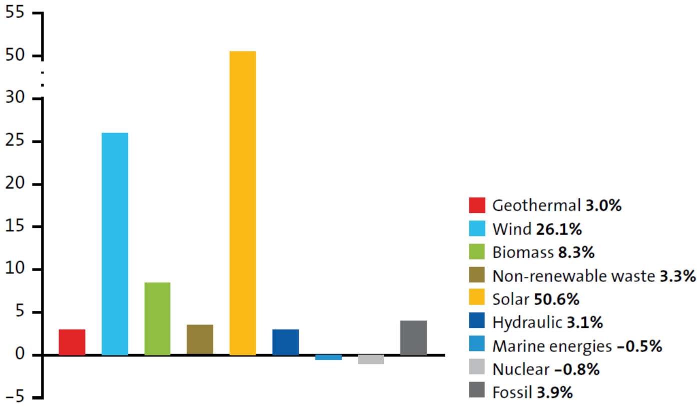

Figure 1.2: Mean annual growth rates 2002-2012.

with comparatively low specific emissions of greenhouse gases. Additionally, pumped storage power plants act as energy reservoir systems able to store and later release large amounts of electricity thanks to cycles of pumping and generation, which regularly achieve unrivaled efficiencies above 80%. Thus, in Europe, hydraulic turbines and pump-turbines are the key components in energy conversion technologies, achieving both load balancing and primary and secondary control over the power network. However, the frequent power transients to be met in production by hydropower plants and imposed by other renewable energy producers require hydraulic units to have their operating range widened. During operation of hydraulic turbines and pump-turbines over a large operating range, high levels of vibration and large fluctuations of pressure and power are likely to occur. As a consequence, life expectancy of pump-turbine machinery is sometimes significantly reduced, eventually leading in the worst occurrences to the accidental loss of structural integrity.

1.2 Off-design operating condition of hydraulic machines

Extreme operating points lead the water turbine to experience complex two-phase flow phenomena, which are sources of dynamic loading of the turbine components as well as of the complete hydraulic system. Examples of the development of dynamic vortex rope in the draft tube at part load and full load are shown in Figure 1.3 in the case of a reduced-scale physical model testing of a Francis turbine.

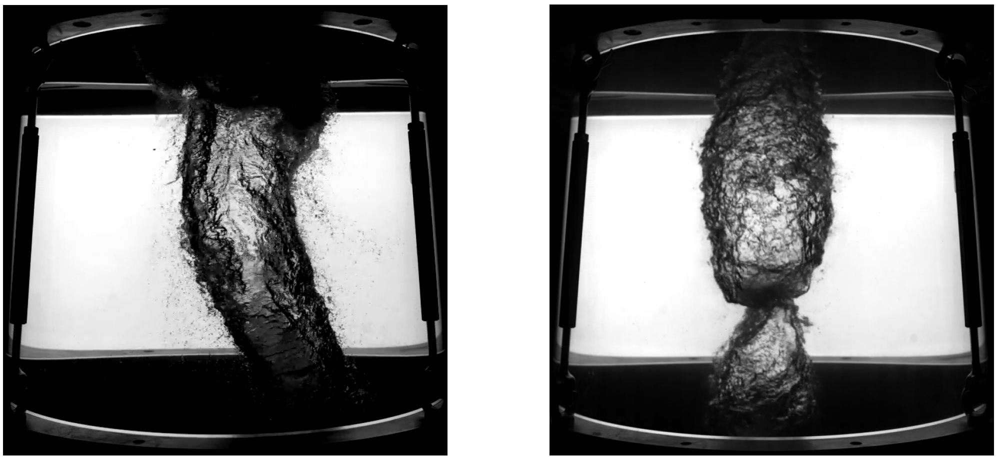

(a) Part load operating point

(b) Full load operating point

Figure 1.3: Cavitation vortex rope in a Francis turbine.

The decrease in tailrace pressure level makes the vortex core visible as a gaseous vortex rope. This phenomenon, referred to as cavitation, corresponds to vaporization at constant temperature due to pressure decrease. The occurrence of the cavitation may induce a drop in efficiency, a risk of erosion, and mechanical vibrations that could jeopardize the safety of mechanical and hydraulic systems [27]. In order to avoid cavitation development at the runner outlet for the best operating condition, the notion of Net Positive Suction Energy (NPSE) is introduced, defining the maximum setting level of a turbine:

$$NPSE = \frac{p_{\bar{B}}}{\rho_w} - \frac{p_v}{\rho_w} - gh_s + \frac{C_{\bar{I}}^2}{2} \tag{1.1}$$

where p_v is the vaporization pressure, ρ_w represents the water density and $C_{\bar{I}}$ defines the flow velocity at the turbine outlet. The level setting h_s, defined in Figure 1.4 is decisive in characterizing the onset of cavitation phenomena. A dimensionless number called the Thoma number σ and defined by the IEC is described as:

$$\sigma = \frac{NPSE}{E} \tag{1.2}$$

Thus, the higher the setting level, the lower the Thoma number. A low value of the Thoma number indicates high risks of cavitation. In turbine mode, E represents the specific energy of the turbine and is defined as a difference of specific hydraulic energies between the inlet I

and the outlet $\bar{I}$ of the turbine, see Figure 1.4.

$$E = gH_I - gH_{\bar{I}} = g\left(\frac{p}{\rho_w} + gZ + \frac{C^2}{2}\right)_I - g\left(\frac{p}{\rho_w} + gZ + \frac{C^2}{2}\right)_{\bar{I}} \tag{1.3}$$

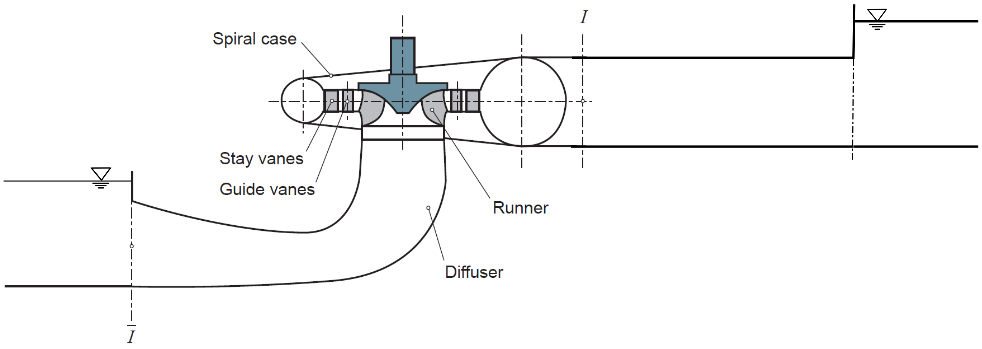

Figure 1.4: Reference altitudes on a Francis turbine outline.

Using the Thoma number, it is possible to define a local cavitation factor χ_E [27]:

$$\chi_E = \frac{p_{\bar{1}x} - p_v}{\rho_w E} = \sigma + \frac{1}{Fr^2}\frac{Z_{ref} - Z_{\bar{1}x}}{D_{\bar{1}}} - \frac{C^2_{\bar{1}x}}{2E} - \frac{E_{r\bar{I}\div x}}{E} \tag{1.4}$$

This factor indicates that the local pressure $p_{\bar{1}x}$ in the draft tube depends on the Thoma number, the Froude number Fr, the energy losses $E_{r\bar{I}\div x}$ and the operating condition of the hydraulic machine defined by the speed factor n_{ED} and the discharge factor Q_{ED}. Physically, the Froude number determines the pressure gradient with respect to the size of the machine and affects the distribution of cavitation in the flow.

$$Fr = \sqrt{\frac{E}{gD_{ref}}} \tag{1.5}$$

1.2.1 Part load condition

The part load condition is characterized by a lower discharge factor than the best efficiency point (BEP). The velocity triangle for the part load condition defined in Figure 1.5 illustrates the relative and the absolute flow velocity vectors $\vec{W}_{\bar{1}}$ and $\vec{C}_{\bar{1}}$ at the runner outlet as well as the peripheral velocity $\vec{U}_{\bar{1}}$. The angle $\beta_{\bar{1}}$ is set by the geometry of the runner blade. The direction of swirl is defined by the peripheral component of the absolute flow velocity $\vec{Cu}_{\bar{1}}$.

For partial load operation, a positive value of this parameter indicates a positive swirling flow, defined as revolving in the same direction as the runner. Qualitatively, the vortex rope features a helical shape and is described as an excitation source for the hydraulic system with a frequency ranging from 0.2 to 0.4 times the rotational frequency [44]. Eigenfrequencies of the hydraulic system decrease with the Thoma number σ and resonance is to be expected if precession frequency matches one of the system's eigenfrequencies, which are linked to the amount of cavitation, i.e. the volume of the vortex rope [45, 26]. Finally, at resonance, pressure oscillations will prematurely damage mechanical and hydraulic systems.

1.2.2 Full load condition

The full load condition is characterized by a higher discharge factor than the BEP. As illustrated in Figure 1.5, the flow at the runner outlet is defined by a negative swirling flow motion in the opposite direction of the runner revolution. Qualitatively, the cavitation vortex rope features an axisymmetric shape. As opposed to the part load conditions, self-oscillations may occur in full load conditions, implying independence of the phenomenon from a periodic external excitation. These self-oscillations are experienced as an axial pulsation of the cavitation volume corresponding to the one of the eigenfrequency of the system. Finally, self-oscillations may cause negative damping, feeding oscillations with more energy [33].

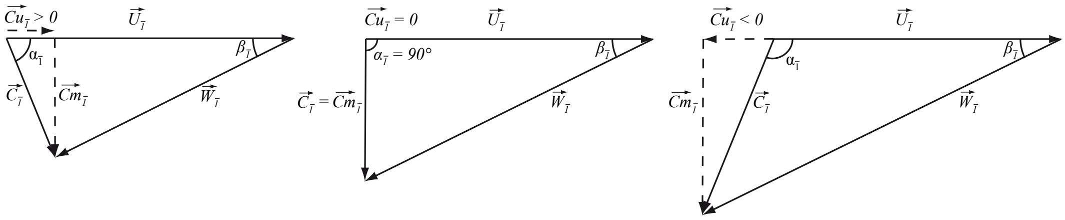

$Q < Q_{BEP}$ $Q = Q_{BEP}$ $Q > Q_{BEP}$

Figure 1.5: Velocity triangles at turbine outlet for partial, BEP and full load operations.

1.3 State of the art

Hydraulic machines are increasingly subject to off-design operation, involving the presence of cavitating flow regimes in the draft tube. The cavitation vortex rope at part load conditions is described as an excitation source for the hydraulic system and interactions between this excitation source and a system's eigenfrequency may result in resonance phenomena and induce a draft tube surge and electrical power swings. To predict and simulate a part load resonance, the method of the transfer matrices was extensively used. Eigenfrequencies and eigenmodes shapes of the pressurized piping systems inclined to reach resonance by excitation from the vortex rope can be derived with this method, see Zielke et al. [65]. However, different hydroacoustic parameters have to be added to predict cavitation surge phenomena.

The first hydroacoustic parameter is called cavitation compliance. This dynamic parameter represents the variation of the cavitation volume with respect to a variation of pressure, and it implicitly defines the local wave speed in the draft tube influencing the traveling time of pressure waves. In 1973, Brennen and Acosta [13] presented theoretical calculations of this parameter and showed influence from blade angle, blade thickness and Thoma number. In 1982, Dörfler [19] was one of the first to measure the cavitation compliance for a Francis turbine vortex rope as a function of the Thoma number. However, his transfer-matrix model [17, 19] for the prediction of pressure and torque fluctuations is restricted to low frequency phenomena [15, 49]. The new model proposed by Couston and Philibert requires the experimental measurement of two parameters: the wave speed, assumed constant along the draft tube, and the vortex rope length. Arpe et al. [7] extended this distributed approach by defining a wave speed depending on the curvilinear abscissa in the draft tube.

Several numerical models were developed to define the wave speed for hydraulic systems with a bubbly air-water mixture. A review about one-dimensional bubbly flow is given by van Wijngaarden [58]. The simplest model described by Wood [62] assumes a homogeneous mixture containing small, isothermal, non-diffusing gas bubbles of uniform radii and devoid of surface tension effects. The isothermal assumption was investigated by Hsieh - Plesset[31] who, always assuming equal pressure in mixture and gas phase, included the equations for conservation of momentum and energy in their analysis, however leaving aside viscous dissipation and viscous forces as well as the velocity difference between the phases. Several investigations about a single oscillating bubble in a liquid have shown that the influence of both the fluid and the gas compressibility and the surface tension can be strong. Thus, Rath [50] developed a theoretical definition linking the wave speed with the void fraction, taking into account these influences for a homogeneous air-water bubbly mixture flow. However, experimental and theoretical wave speeds published by Henry et al. [30] showed significant differences between bubbly flow, slug flow and stratified flow. Consequently, these theoretical models were only validated for homogeneous bubbly flow and cannot be directly transposed to a cavitation vortex rope without validation.

The second hydroacoustic parameter is related to the dissipation due to the cavitation. Alligné [3] assumed that most of the energy dissipation is associated with the cavitation compliance and it represents internal processes breaking a thermodynamic equilibrium between the cavitation volume and the surrounding liquid. A bulk viscosity was used to model this dissipation. Many authors tried to set up a mathematical model to quantify this bulk viscosity for cavitating pipe flows. Bartolini and Siccardi [9] considered the formulation of an additional dissipation term in unsteady cavitating flows taking into account local relaxation processes. Later, Ewing [24] derived an analytical bulk viscosity considering small variations of temperature of gas bubbles due to heat exchange between gas and surrounding liquid. It has been shown that this thermodynamic approach does not always systematically explain the energy dissipations observed in cavitating water hammer flows. Pezzinga [48] used the same approach as Ewing and validated his model by reproducing results of experimental measurements of water hammer transients with cavitation. This model indicates that the bulk viscosity depends on the wave speed and the pressure. However, this model is only validated for homogeneous bubbly flow and cannot be directly transposed to a cavitation vortex rope without validation.

The third hydroacoustic parameter is the excitation source induced by the precessing vortex rope. The pressure fluctuations measured in the cone are composed of two different components: a rotating part due to the transit of the cavitation vortex rope near the wall, and a synchronous part with an equal phase and amplitude for all locations in the same cross-section. Nishi *et al.* [44] introduced this distinction and devised an analytical method for the separation of the two components. Experimental computation of the rotating and synchronous parts of pressure fluctuations was confirmed by Angelico *et al.* [6] by using three pressure sensors located in a same cross-section of the cone. Dörfler [19] assumed that this synchronous part is a component resulting from the excitation source and is transmitted to the hydraulic circuit. Thus, Dörfler experimentally identified this pressure source without cavitation vortex rope and assumed that the excitation source is independent of the Thoma number. Finally, recent numerical flow simulations of the helical vortex rope [51, 52, 54, 66] computed the synchronous component of the pressure fluctuations. Alligné [3] in 2011 described a methodology to predict part load resonance and full load instability induced by the Francis turbine excitation. The identification of the excitation sources was performed with numerical simulations based on a three dimensional incompressible model. Finally, Dörfler *et al.* [21] introduced a new stochastic component for the excitation source and developed a statistical method to separate it from the two others components.

At full load condition, an additional parameter is introduced: the mass flow gain factor. This parameter represents the rate of change of the cavitation volume as a function of the change in discharge. Koutnik and Pulpitel [36] applied this modeling approach to Francis turbines and derived a stability diagram to explain a full load surge occurring on a power plant. A similar approach was also successfully applied to explain inducer instabilities by Tsujimoto *et al.* in 1993 [56]. The model assumed a mass flow gain factor linked to a downstream flow rate of the cavitation volume. Chen *et al.* [14] derived a more general model taking into account both upstream and downstream flow rates of the cavity. They analyzed the influence of the swirl intensity related to the upstream flow rate and the diffuser factor related to the downstream flow rate on the system stability. Dörfler [20] showed that the choice between the upstream or the downstream flow rate is decisive to predict the stability limit of the system. He proposed a new model [22] by using a weight function between the upstream and the downstream flow rates. He also introduced a time delay on the upstream flow rate. This time delay effect has been also introduced by Tsujimoto *et al.* [57] for the analysis of rotating cavitation in the inducers. They found out that this parameter allows for the accurate determination of the amplitude of the rotating modes. Finally, extensive experimental investigations were performed by Müller [40] to increase the understanding of its underlying causes and key sustaining mechanisms. Müller [39] concluded in 2014 that the modification of the flow swirl in the draft tube inlet through the appearance of cavitation on the runner blade plays an important role in the feedback mechanism of the self-excited pressure and vortex rope oscillation.

1.4 Thesis objective

It was noted above that the numerical models for identification of wave speed and bulk viscosity of a bubbly flow cannot be directly transposed to a cavitation vortex rope without validation. Additionally, the modeling of the pressure source induced by the precession of the cavitation vortex rope is still unknown and its connection with the Thoma number and the Froude number is not well defined yet.

The main purpose of the current thesis is to establish a methodology to determine the various hydroacoustic parameters necessary for numerical simulation. Using these parameters, the numerical model will be able to predict the unsteady pressure and torque fluctuations of a hydraulic power plant in operation.

The methodology is based on the direct link between the natural frequency of the hydraulic system and the wave speed in the draft tube. With the identification of the natural frequency, it is possible to quantify the wave speed, the cavitation compliance and the void fraction of the cavitation vortex rope with an accurate numerical model. In order to determine the energy dissipation induced by the cavitation volume, it is important to experimentally inject a known amount of energy in the hydraulic system at the natural frequency. A spectral analysis of the forced harmonic response is used to identify the bulk viscosity and the pressure source induced by the vortex rope precession.

However, the methodology presented in this thesis is only applicable to an off-resonance system to avoid any energy exchange between the excitation frequency and the vortex rope frequency. Therefore, the method has only been applied to part load operating conditions. Indeed, at full load operating conditions, the system may be self-excited and the volume of cavitation may oscillate at the natural frequency of the hydraulic system. Additionally, it is assumed that the mass flow gain factor is negligible for an off-resonance system at part load operating condition and it will not be taken into account in this methodology.

Identification of hydroacoustic parameters requires the development of a numerical model of the studied hydraulic system, as well as an experimental excitation system for identifying the natural frequency of the hydraulic system. With the help of several pressure sensors located along the hydraulic system, hydroacoustic parameters of the numerical model are calibrated to reproduce the forced harmonic response measured in experiments. Afterward, the numerical results are generalized through the use of dimensionless relations in order to predict the hydroacoustic parameters for different Thoma and Froude numbers, and then to predict the pressure and torque fluctuations of a reduced scale model of a Francis turbine.

Finally, the dimensionless relations are transposed to the prototype in order to predict the dynamic behavior of a hydropower plant. The current study is part of the *HYPERBOLE* collaborative research project in association with the world major turbine manufacturers. The transposition of the hydroacoustic parameters will be compared against the real generating unit located in a hydropower plant in the Canadian province of British Columbia.

1.5 Document structure

Chapter 2 introduces and expands the fundamental equations used for the hydroacoustic modeling of the cavitation vortex rope. The discretization of these equations produces a system of nonlinear ordinary equations. An equivalent electrical scheme representation of the equations provides a high level of abstraction and allows for a rigorous formalism to model the dynamic behavior of a hydraulic power system. Among the parameters modeling the cavitation vortex rope, the wave speed, the bulk viscosity and the pressure source are the three hydroacoustic parameters requiring a special methodology to determine their value.

Chapter 3 presents a simple and inexpensive method to identify the three unknown hydroacoustic parameters. This methodology is based on the direct link that exists between the natural frequency of the hydraulic system and the wave speed in the draft tube. To highlight this important link, an analytical analysis of a simplified hydraulic system is presented. Then, the experimental identification of the natural frequency and the three hydroacoustic parameters are described. A sensibility analysis finally justifies the existence of one or several local minimum and therefore the type of algorithm used for the identification.

Chapter 4 concerns the description of the experimental instrumentation setup. First, the test rig and the reduced-scale physical model of a Francis turbine are described. Then, the design of the excitation system and the location of all flush-mounted piezoresistive pressure sensors are presented. After the characterization of the rotating valve and a detailed description of the measurement techniques and post-processing tools, the eigenfrequencies for several operating conditions are identified. Finally, this chapter also contains a validation of the Pressure-Time method necessary to identify the bulk viscosity.

Chapter 5 presents the modeling of the test rig with EPFL SIMSEN software. All hydraulic components of the test rig such as viscoelastic pipes, Francis turbine and spiral casing are described. A comparison between the numerical and experimental results suggests very good accuracy of the numerical model for a steady flow.

Chapter 6 applies the methodology described in Chapter 3 to the reduced-scale physical model of a Francis turbine presented in Chapter 4. The three hydroacoustic parameters are identified for different operating conditions and the influence of the Thoma and the Froude numbers is analyzed. It is shown that the formulation to describe the wave speed in bubbly flows can be used in a cavitation vortex rope by dividing the obtained values by an empirical constant. An analytical equation is also developed to predict the bulk viscosity as a function of the void fraction. Furthermore, a sensitivity analysis determines the location and the shape of the pressure source. Different numerical draft tube models are also compared to determine the impact of convective and divergent geometry terms of the momentum equation on the identification of the hydroacoustic parameters. Finally, to investigate the stability operation of the prototype, the hydroacoustic parameters are transposed to the prototype conditions according to similitude laws.

Chapter 7 provides a simplified methodology to identify the hydroacoustic parameters. Using the dimensionless curves and sensitivity analyzes developed in Chapter 6, the methodology presented in Chapter 3 can be simplified and applied to any type of hydraulic test rig.

2 Cavitation vortex rope modeling

Extreme operating conditions lead the water turbine to experience complex two-phase flow phenomena, which are sources of dynamic loading of the turbine components as well as of the complete hydraulic system. At part load operation, the flow at the runner outlet is animated by a positive swirling flow in the same direction as the runner revolution. Qualitatively, the vortex rope features a helical shape and is described as an excitation source for the hydraulic system. Interactions between this excitation source and eigenfrequencies of the system may result in resonance phenomena and induce a draft tube surge and electrical power swings. To precisely predict and simulate a part load resonance, proper modeling of the draft tube is critical. The presence in it of a cavitation vortex rope requires a numerical pipe element taking into account the complexity of the two-phase flow [5].

The present chapter introduces and expands the momentum and continuity equations describing a cavitating draft tube flow. The discretization of these equations produces a system of nonlinear ordinary differential equations that can be represented as a T-shaped equivalent scheme. Among the parameters describing the numerical model of the cavitating draft tube flow, three hydroacoustic parameters require a special attention: the wave speed, the bulk viscosity and the pressure source.

2.1 One-dimensional hydroacoustic equations

A mathematical model based on mass and momentum conservation is well suited to describing the dynamic behavior of a cavitating draft tube flow. Since wave lengths are greater than cross-sectional dimensions, it is justified to use a one-dimensional approach. The model assumes a flow normal to the cross-section A, and uniform distributions of pressure p and velocity C in the cross-section.

2.1.1 The axial momentum equation

The momentum equation states that the resultant component of forces acting on a control volume, described in Figure 2.1 (Left), is equal to the material derivative.

Due to the cavitation development in the draft tube, a homogeneous fluid model is assumed and a density mixture ρ is considered.

$$\rho \frac{D\overrightarrow{C}}{Dt} = -\overrightarrow{\nabla} p + \overrightarrow{\nabla} \cdot \tau + \overrightarrow{f} \tag{2.1}$$

The pressure gradient $\overrightarrow{\nabla} p$ arises from the isotropic part of the Cauchy stress tensor. The deviatoric stress τ is straightforwardly defined as the difference between the pressure and the total stress tensor. The vector field $\overrightarrow{f}$ represents body forces.

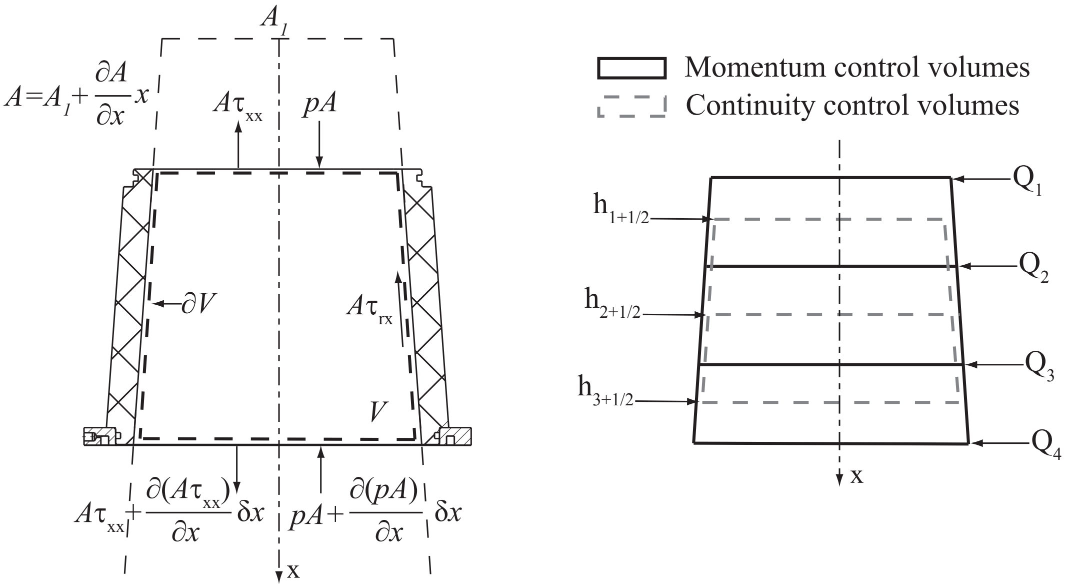
A_1
$A = A_1 + \frac{\partial A}{\partial x} x$
$A\tau_{xx}$
pA
∂V
$A\tau_{rx}$
V
$A\tau_{xx} + \frac{\partial (A\tau_{xx})}{\partial x} \delta x$
$pA + \frac{\partial (pA)}{\partial x} \delta x$
x
Momentum control volumes
Continuity control volumes
$h_{1+1/2}$
Q_1
Q_2
$h_{2+1/2}$
Q_3
$h_{3+1/2}$
Q_4
x

Figure 2.1: Balances of forces for the momentum equation (Left) and overlapping of momentum and continuity control volumes (Right)

Assuming cylindrical coordinates, projection along the pipe axis x prompts the following formulation:

$$\rho \frac{DC}{Dt} = -\frac{\partial p}{\partial x} + \frac{1}{r}\frac{\partial}{\partial r}(r\tau_{rx}) + \frac{\partial}{\partial x}(\tau_{xx}) \tag{2.2}$$

where τ_{rx} are the tangential viscous stresses and τ_{xx} are the normal viscous stresses. In the case of Newtonian fluids, components of the stress tensor depend linearly on components of the tensor of strain rate e:

$$e_{ij} = \frac{1}{2}\left(\frac{\partial C_j}{\partial x_i} + \frac{\partial C_i}{\partial x_j}\right) \quad \text{where} \quad tr\left(e_{ij}\right) = \overrightarrow{\nabla} \cdot \overrightarrow{C} \tag{2.3}$$

For isotropic fluid, *i.e.* fluids whose mechanical properties are direction-invariant, the tangential viscous stresses and the normal stresses can be rewritten as:

$$\tau_{rx} = \mu \frac{\partial C}{\partial r} \quad \text{and} \quad \tau_{xx} = \left(2\mu + \mu'\right)\frac{\partial C}{\partial x} \tag{2.4}$$

μ is the dynamic viscosity and μ' is the second viscosity. These two viscosity coefficients are similar to the Lamé parameters in linear elasticity. According to the equation 2.4, the momentum equation can be defined as:

$$\rho\frac{DC}{Dt} = -\frac{\partial p}{\partial x} + \frac{1}{r}\frac{\partial}{\partial r}\left(r\mu\frac{\partial C}{\partial r}\right) + \frac{\partial}{\partial x}\left(\left(2\mu + \mu'\right)\frac{\partial C}{\partial x}\right) \tag{2.5}$$

Integration of Equation 2.5 over the control volume V of length dx yields:

$$\int_V \rho\frac{DC}{Dt}dV = -\int_V \frac{\partial p}{\partial x}dV + \int_V \frac{1}{r}\frac{\partial}{\partial r}\left(r\mu\frac{\partial C}{\partial r}\right)dV + \int_V \frac{\partial}{\partial x}\left(\left(2\mu + \mu'\right)\frac{\partial C}{\partial x}\right)dV \tag{2.6}$$

Regarding the tangential component of the stress tensor, the Darcy-Weisbach formulation is used with $\tau_0 = \frac{\rho\lambda|C|C}{8}$. The simplification of the last equation by $\left(\rho g A dx\right)$ yields:

$$\frac{1}{g}\frac{\partial C}{\partial t} + \frac{C}{g}\frac{\partial C}{\partial x} = -\frac{1}{\rho g}\frac{\partial p}{\partial x} - \frac{\pi D\tau_0}{\rho A g} + \frac{1}{\rho g}\frac{\partial}{\partial x}\left(\left(2\mu + \mu'\right)\frac{\partial C}{\partial x}\right) \tag{2.7}$$

Equation 2.7 can be rewritten by using the flow rate Q and the piezometric head h as state variables. $K_x = \frac{\partial A}{\partial x}$ is the cross-section expansion rate along the x axis of the draft tube geometry and the divergent geometry is assumed to be constant, $\frac{\partial^2 A}{\partial x^2} = 0$. Moreover, since the draft tube wall is solid, $\frac{\partial A}{\partial t} = 0$, hence:

$$\frac{1}{gA}\frac{\partial Q}{\partial t} + \frac{Q}{gA^2}\frac{\partial Q}{\partial x} - \frac{K_x Q^2}{gA^3} = -\frac{\partial h}{\partial x} - \frac{\pi D\tau_0}{\rho g A} + \frac{\left(2\mu + \mu'\right)}{\rho g}\left(\frac{-2K_x}{A^2}\frac{\partial Q}{\partial x} + \frac{1}{A}\frac{\partial^2 Q}{\partial x^2} + \frac{2K_x^2}{A^3}Q\right) \tag{2.8}$$

The homogeneous bulk viscosity μ'' is then introduced and defined as:

$$\mu'' = \mu' + \frac{2}{3}\mu \tag{2.9}$$

Finally, swapping the terms and assuming only a distribution of the bulk viscosity μ'' in the normal stress component [48], Equation 2.8 can be rewritten as:

$$\frac{1}{gA}\frac{\partial Q}{\partial t} + \left(\frac{Q}{gA^2} - \frac{2K_x \cdot \mu''}{\rho g A^2}\right)\frac{\partial Q}{\partial x} + \left(\frac{\lambda |Q|}{2gDA^2} - \frac{K_x Q}{gA^3} + \frac{2K_x^2 \mu''}{\rho g A^3}\right)Q + \frac{\partial h}{\partial x} - \frac{\mu''}{\rho g A}\frac{\partial^2 Q}{\partial x^2} = 0 \tag{2.10}$$

In the model developed by Alligné *et al.* [5], only the dissipation due to the velocity gradient induced by the compressibility of the cavitation volume is taken into account. He assumed that the dissipation induced by the variation of the cross-section is negligible and therefore the momentum equation becomes:

$$\frac{1}{gA}\frac{\partial Q}{\partial t} + \left(\frac{Q}{gA^2}\right)\frac{\partial Q}{\partial x} + \left(\frac{\lambda |Q|}{2gDA^2} - \frac{K_x Q}{gA^3}\right)Q + \frac{\partial h}{\partial x} - \frac{\mu''}{\rho g A}\frac{\partial^2 Q}{\partial x^2} = 0 \tag{2.11}$$

In order to verify the assumption proposed by Alligné *et al.*, results obtained from both the general equation 2.10 and the simplified equation 2.11 will be compared in Chapter 6.

2.1.2 The continuity equation

The continuity balance is performed on a control volume V of length dx including a fluctuating cavitation volume V_c. The control volume is defined as the sum of the cavitation volume and the liquid phase volume V_L:

$$V = V_c + V_L \tag{2.12}$$

Additionally, the mass variation of the liquid phase volume m_L can be described as:

$$\frac{dm_L}{dt} = V_L \frac{d\rho_L}{dt} + \rho_L \frac{dV_L}{dt} \tag{2.13}$$

where ρ_L is the density of the liquid phase. The variation rate of the liquid mass corresponds to the difference between the mass inflow and the mass outflow. Using Equation 2.12, the variation rate of mass of the liquid phase volume becomes:

$$\frac{dm_L}{dt} = \rho_L (Q_1 - Q_2) = V_L \frac{d\rho_L}{dt} + \rho_L \frac{dV}{dt} - \rho_L \frac{dV_c}{dt} \tag{2.14}$$

Introducing the void fraction β defined as the fraction of a reference volume V that is occupied by the gas phase volume V_c, the previous equation can be rewritten as:

$$\rho_L (Q_1 - Q_2) = \left(1-\beta\right) V \frac{d\rho_L}{dt} + \rho_L \frac{dV}{dt} - \rho_L \frac{dV_c}{dt} \quad \text{where} \quad \beta = \frac{V_c}{V} \tag{2.15}$$

The liquid phase is assumed to have a barotropic behavior, *i.e.* liquid phase density is a function of only pressure $\rho_L = \rho_L\left(p\right)$. From this assumption, it results:

$$\frac{1}{\rho_L}\frac{d\rho_L}{dt} = \frac{1}{E_L}\frac{dp}{dt} \tag{2.16}$$

with E_L as the liquid phase bulk modulus. The elastic behavior of the pipe wall sets a relation between the cross-section variation and the pressure variation with e, D and E_p defined as the thickness, the diameter and the Young modulus of the elastic pipe wall, respectively.

$$\frac{1}{A}\frac{dA}{dt} = \frac{D}{eE_p}\frac{dp}{dt} \tag{2.17}$$

Combining Equations 2.16 and 2.17 in Equation 2.15 and defining the volume $V = Adx$, it results:

$$(Q_1 - Q_2) = \left(1-\beta\right)\frac{Adx}{E_L}\frac{dp}{dt} + \frac{AdxD}{eE_p}\frac{dp}{dt} - \frac{dV_c}{dt} \tag{2.18}$$

For a pipe free of cavitation, the wave speed a_0 is defined as:

$$a_0^2 = \frac{1}{\rho_L\left(\frac{1}{E_L} + \frac{D}{eE_p}\right)} \tag{2.19}$$

Using the definition of the wave speed in a cavitation-free flow, the wave speed in the liquid phase can be written as:

$$a_\beta^2 = \frac{1}{\rho_L\left(\frac{1-\beta}{E_L} + \frac{D}{eE_p}\right)} \tag{2.20}$$

With the help of equation 2.20 and by using the piezometric head h as state variable, Equation 2.18 becomes:

$$(Q_1 - Q_2) = \frac{gAdx}{a_\beta^2}\frac{dh}{dt} - \frac{dV_c}{dt} \tag{2.21}$$

Besides, the dynamic behavior of the cavitation volume fluctuations $\frac{dV_c}{dt}$ can be described with the help of three parameters as follows [5]:

- The cavitation compliance : $C_c = -\frac{\partial V_c}{\partial h}$
- The mass flow gain factor : $\chi = -\frac{\partial V_c}{\partial Q_1}$
- The rotational speed gain factor : $\epsilon = -\frac{\partial V_c}{\partial U_1}$

Hence:

$$-\frac{dV_c}{dt} = \epsilon\frac{dU_1}{dt} + \chi\frac{dQ_1}{dt} + C_c\frac{dh}{dt} \tag{2.22}$$

By assuming a constant rotational speed of the turbine, the previous equation becomes:

$$-\frac{dV_c}{dt} = \chi\frac{dQ_1}{dt} + C_c\frac{dh}{dt} \tag{2.23}$$

Merging Equations 2.21 and 2.23 produces the new continuity equation:

$$(Q_1 - Q_2) = \left(\frac{gAdx}{a_\beta^2} + C_c\right)\frac{dh}{dt} + \chi\frac{dQ_1}{dt} \tag{2.24}$$

2.2 Equivalent electrical scheme representation

The hydroacoustic draft tube model is implemented with the help of SIMSEN, an EPFL software that was initially developed for transient simulations of electrical power systems [53]. The software was extended to hydraulic components in order to simulate the transient behavior of a complete hydroelectric power plants. An exhaustive description of the most common hydraulic components are described in reference [41]. The modeling of the hydraulic components is based on T-shaped equivalent electrical scheme representation. The terms in the momentum equation 2.11 and the continuity equation 2.24 can be represented by the following electric components:

- The terms of fluid inertia and the energy losses present in the momentum equation can be represented by a hydraulic inductance L and a hydraulic resistance R_λ, respectively.

$$R'_\lambda = \frac{\lambda |Q|}{2gDA^2} \qquad L' = \frac{1}{gA} \tag{2.25}$$

- The divergent geometry of the draft tube has a destabilizing effect and is modeled through a negative resistance $-R'_d$.

$$R'_d = \frac{K_x Q}{gA^3} \tag{2.26}$$

- The occurrence of cavitation volumes in the draft tube strongly decreases the wave speed and therefore the convective terms of the Navier-Stokes equations have to be taken into account. The modeling of this effect is represented by an electrical source and is described by the parameter J'.

$$J' = \frac{Q}{gA^2} \tag{2.27}$$

- The dissipation representing internal processes breaking a thermodynamic equilibrium between the cavitation volume and the surrounding liquid is described by a hydraulic resistance defined as R'_μ, where μ'' represents the bulk viscosity.

$$R'_\mu = \frac{\mu''}{\rho g A} \tag{2.28}$$

- At part load conditions, the cavitation vortex rope is considered as an external forcing function for the hydraulic system. The equivalent electrical scheme is modified by integrating an additional pressure source S_h corresponding to the forced induced by the helical vortex rope precession on the draft tube walls. Dörfler [19] experimentally identified this pressure source in cavitation-free conditions for vortex rope and assumed that the excitation source is independent of the Thoma number.

- Finally, the storage effects can be represented by the equivalent hydraulic capacitance C_{equ} defined in the continuity equation:

$$C_{equ} = \left(\frac{gAdx}{a_\beta^2} + C_c \right) = C_\beta + C_c \tag{2.29}$$

The first term corresponds to the storage effects due to wall deflection and fluid compressibility. In the case of cavitation-free conditions, the void fraction $\beta = 0$, and this term defines the general hydraulic capacitance C for a pipe:

$$C = \left(\frac{gAdx}{a_0^2} \right) \tag{2.30}$$

The second term of Equation 2.29 is defined as a cavitation compliance C_c and represents the variation of the cavitation volume V_c with respect to a variation of pressure. Moreover, according to the general definition of the hydraulic capacitance, an equivalent wave speed can be introduced:

$$C_{equ} = \left(\frac{gAdx}{a_\beta^2} + C_c \right) = \frac{gAdx}{a_{equ}^2} \tag{2.31}$$

It will be proven in Chapter 6 that the most of the energy dissipation is due to the cavitation compliance rather than the wall deflection or the compressibility of the liquid. Therefore, the dissipation due to the wall deflection is neglected and an homogeneous approach of the fluid including the liquid and cavitation is considered [48]. Thus, the equivalent capacitance indirectly defines the wave speed in the cavitation draft tube.

Using these definitions, the momentum and the continuity equations can be rewritten as:

$$\begin{cases} L'\frac{\partial Q}{\partial t} + J'\frac{\partial Q}{\partial x} + \left(R'_\lambda - R'_d\right)Q + \frac{\partial h}{\partial x} - R'_\mu \frac{\partial^2 Q}{\partial x^2} + S_h = 0 \\ (Q_1 - Q_2) = C_{equ}\frac{dh}{dt} + \chi \frac{dQ_1}{dt} \end{cases} \tag{2.32}$$

The momentum and the continuity equations are solved using the Finite Difference Method with 1^{st} order centered scheme discretization in space and a Lax scheme for the discharge state variable. This discretization produces a system of nonlinear ordinary differential equations that can be represented as a T-shaped equivalent scheme [42], see Figure 2.2. It is important to note that the control volumes for the continuity and the momentum balances overlap in space as illustrated in Figure 2.1 (Right) on a straight divergent pipe in order to allow for the spatial discretization of both the state variables Q and h. Considering the above-mentioned spatial discretization, the Navier-Stokes equations expressed for a lumped draft tube model are expressed as follows:

$$\begin{pmatrix} L/2 & 0 & 0 \\ 0 & L/2 & 0 \\ \chi & 0 & C_{equ} \end{pmatrix} \cdot \frac{d}{dt} \begin{pmatrix} Q_1 \\ Q_2 \\ h_{1+\frac{1}{2}} \end{pmatrix} +$$

$$\begin{pmatrix} \frac{1}{2}\left(R_\lambda - R_d - J_1\right) + R_\mu & 1 & \frac{J_1}{2} - R_\mu \\ \frac{J_2}{2} - R_\mu & \frac{1}{2}\left(R_\lambda - R_d - J_2\right) + R_\mu & -1 \\ -1 & 1 & 0 \end{pmatrix} \cdot \begin{pmatrix} Q_1 \\ Q_2 \\ h_{1+\frac{1}{2}} \end{pmatrix} = \begin{pmatrix} h_1 - S_{h1} \\ -h_2 + S_{h2} \\ 0 \end{pmatrix} \tag{2.33}$$

This set of equations is written using the hydroacoustic parameters obtained for an element of length dx given by:

$$L = L' dx, \qquad R_\lambda = R'_\lambda dx, \qquad J = J', \qquad R_d = R'_d dx, \qquad R_\mu = \frac{R'_\mu}{dx} \tag{2.34}$$

The first and the second equations of 2.33 correspond to the two momentum equations of the T-shaped equivalent electrical scheme while the third equation describes the continuity equation. This set of equations can be rewritten as:

$$A\frac{d\mathbf{X}}{dt} + \left[B\left(\mathbf{X}\right)\right]\mathbf{X} = \mathbf{V}\left(\mathbf{X}\right) \tag{2.35}$$

where A and B are the global state matrices, $\mathbf{X}$ and $\mathbf{V}(\mathbf{X})$ are the state vector and the boundary conditions vector with n components, respectively.

Among the parameters modeling the cavitation vortex rope, only three parameters are difficult to quantify: the cavitation compliance C_c depending only on the wave speed a, the bulk viscosity μ'' and the pressure source S_h. The other parameters mainly depend on the geometry of the draft tube and state variables. To quantify the wave speed, the bulk viscosity and the pressure source, a methodology will be applied in resonance-free conditions at part load

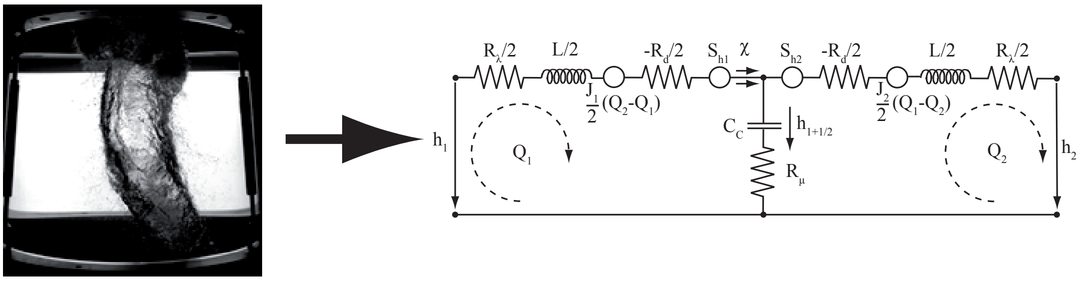

Figure 2.2: Representation of the draft tube with a cavitation vortex rope and its equivalent circuit

condition in order to prevent interactions between the vortex rope frequency and the natural frequency. Therefore, it is assumed that the mass flow gain factor χ is negligible and it will not be taken into account in the methodology presented in Chapter 3.

2.3 Summary and discussion

The proposed mathematical model based on mass and momentum conservations was exposed in this chapter to describe the dynamic behavior of a cavitating flow in a draft tube. This model assumes an isotropic fluid with liquid phase having a barotropic behavior. The dissipation induced by the compressibility of the cavitation volume is the only dissipation term being taken into account. The dissipation due to the wall deflection is neglected and an homogeneous approach of the fluid embodying both the liquid and cavitation volumes is considered.

With a 1^{st} order centered scheme discretization in space and a Lax scheme for the discharge state variable, the discretization produces a system of nonlinear ordinary differential equations that can be represented as a T-shaped equivalent scheme. Among the parameters modeling the cavitation vortex rope, only three parameters are difficult to quantify: the wave speed a, the bulk viscosity μ'' and the pressure source S_h. To identify these hydroacoustic parameters, a methodology based on spectral analysis was developed and is presented in the next chapter.

3 Methodology for identification of hydroacoustic parameters

A simple and inexpensive method has been developed to identify physical parameters such as wave speed, bulk viscosity and pressure source induced by the cavitation vortex rope in complex unsteady flows of a draft tube. The methodology is based on the direct link that exists between the natural frequency of the hydraulic system and the wave speed in the draft tube. This identification requires the development of a numerical model of the studied hydraulic system including the modeling of a draft tube with the SIMSEN software, as well as an external excitation system for identifying the natural frequency of the hydraulic system. After a detailed description of the experimental equipment in Chapter 4, the numerical model will be presented in Chapter 5.

First, the natural frequency is identified with the help of an external excitation system. Then the wave speed is determined thanks to an accurate numerical model of the experimental hydraulic system. By applying this identification procedure for different values of Thoma number, it is possible to quantify the cavitation compliance and the void fraction of the cavitation vortex rope. In order to determine the energy dissipation induced by the cavitation volume, the experimental hydraulic system is excited at the natural frequency. With a Pressure-Time method, the amount of excitation energy is quantified and is injected in the numerical model. A spectral analysis of the forced harmonic response is used to identify the bulk viscosity and the pressure source induced by the vortex rope precession.

In order to precisely determine the amount of energy exiting the system, this methodology is only applicable to an off-resonance system to avoid any energy exchange between the excitation frequency and the vortex rope frequency. Therefore, the method has only been applied to partial operating conditions. Indeed, at full load operating conditions, the system may be self-excited and the volume of cavitation may oscillate at the natural frequency of the hydraulic system. Finally, the hydroacoustic parameters are generalized with dimensionless relations in order to predict their values for different operating points and to predict the pressure and torque fluctuations on the reduced-scale physical model.

3.1 Analytical analysis of a simplified hydraulic system

To identify the link between the wave speed and the natural frequency, an analytical analysis is applied to a simplified hydraulic system. It is composed of a Francis turbine and a draft tube connected between two reservoirs, as illustrated in Figure 3.1. The cavitation development is modeled using the equation 2.24.

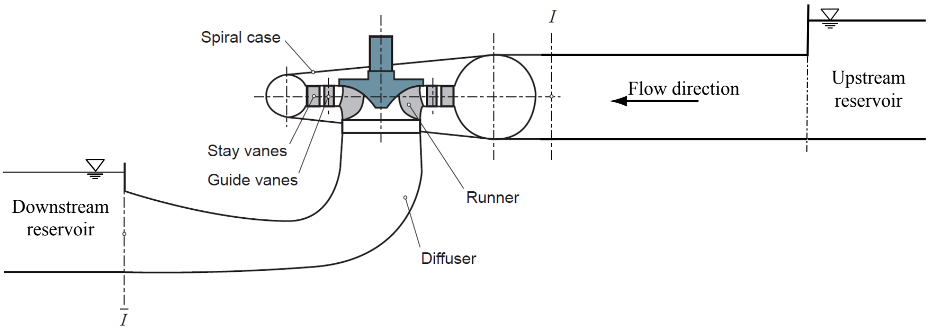

Figure 3.1: Representation of the simplified hydraulic system.

To simplify the analytical development, the geometric characteristics and the materials of the pipes are considered as similar. According to the definition of the hydraulic capacitance, it is now possible to rewrite the equation 2.31 as:

$$C_c = \left(\frac{gAdx}{a_{equ}^2} - \frac{gAdx}{a_{\beta}^2} \right) \approx \frac{gAdx}{a_{equ}^2} \tag{3.1}$$

The wave speed for cavitating flow described in the literature indicates values dropping below 100 m/s for a pressure in the vicinity of 1 bar [50]. Thus, it is assumed that the compressibility of the pipe is negligible compared to a capacitance related to the cavitation compliance. Thus, the equivalent model of the pipe is made of a resistance R and an inductance L. For sufficient guide vane openings, the Francis turbine is modeled as a pressure source driven by the turbine characteristics and also as a function of the rotational speed N, the discharge Q and the guide vane opening y [3]. The equivalent model of the simplified hydraulic system is presented in Figure 3.2.

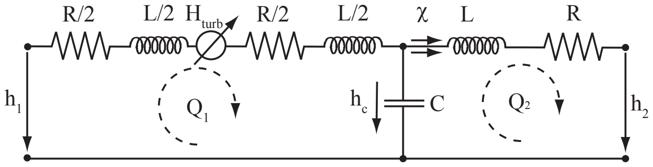

Figure 3.2: Equivalent circuit of the simplified hydraulic system.

The system of differential equations of the equivalent scheme for the hydraulic system is given by the following set of equations:

$$\begin{cases} \chi\frac{\partial Q_2}{\partial t} + C\frac{\partial h_c}{\partial t} = Q_1 - Q_2 \\ H_{turb} + RQ_1 + L\frac{\partial Q_1}{\partial t} + h_c = h_1 \\ h_c = L\frac{\partial Q_2}{\partial t} + RQ_2 + h_2 \end{cases} \tag{3.2}$$

Eigenvalues extraction from this set of differential equations is provided after a linearization around a solution point [3], [37].

$$\begin{pmatrix} C & 0 & \chi \\ 0 & L & 0 \\ 0 & 0 & L \end{pmatrix} \cdot \frac{d}{dt} \begin{pmatrix} \delta h_c \\ \delta Q_1 \\ \delta Q_2 \end{pmatrix} + \begin{pmatrix} 0 & -1 & 1 \\ 1 & 2R + \frac{\delta H_{turb}}{\delta Q} & 0 \\ -1 & 0 & 2R \end{pmatrix} \cdot \begin{pmatrix} \delta h_c \\ \delta Q_1 \\ \delta Q_2 \end{pmatrix} = \begin{pmatrix} 0 \\ h_1 \\ -h_2 \end{pmatrix} \tag{3.3}$$

The determinant of this set of equations leads to the characteristic equation 3.4, where s is the eigenvalue.

$$\left(\frac{2R}{L} + s\right)\left(s^2 + s\left(\frac{\chi}{LC} + \frac{1}{L}\left(2R + \frac{\delta H_{turb}}{\delta Q}\right)\right) + \frac{2}{LC} + \frac{\chi}{L^2C}\frac{\delta H_{turb}}{\delta Q}\right) + \frac{1}{L^2C}\frac{\delta H_{turb}}{\delta Q}\left(1 - \frac{2R\chi}{L}\right) = 0 \tag{3.4}$$

Since for operating conditions at part load, it can be assumed that the mass flow gain factor is equal to zero, and the previous equation can be rewritten as:

$$\left(\underbrace{\frac{2R}{L}}_{\frac{1}{\tau}} + s\right)\left(s^2 + s\underbrace{\left(\frac{1}{L}\left(2R + \frac{\delta H_{turb}}{\delta Q}\right)\right)}_{2\mu} + \underbrace{\frac{2}{LC}}_{\omega_0^2}\right) + \frac{1}{L^2C}\frac{\delta H_{turb}}{\delta Q} = 0 \tag{3.5}$$

τ corresponds to a free motion time constant. The stability criterion of the system is given by $2\mu > 0$ and depends on the hydraulic resistance, the hydraulic inductance and the gradient of the turbine characteristic. The frictionless eigenpulsation is function of the hydraulic inductance and hydraulic capacitance. From this relation, the frictionless natural frequency can be inferred:

$$f_0 = \frac{1}{2\pi}\sqrt{\frac{2}{LC}} = \frac{1}{2\pi}\sqrt{\frac{2a^2}{l^2}} = \frac{a}{\sqrt{2}\pi l} \tag{3.6}$$

There is therefore, for this simplified case, a direct link between the frictionless natural frequency and wave speed [32]. It is consequently possible to derive an approximation of the wave speed by identifying the natural frequency of the simplified hydraulic system.

3.2 Experimental identification of the natural frequency

To experimentally identify the natural frequency of a hydraulic system, an excitation system was designed, engineered and constructed to inject or extract a periodical discharge at a given frequency. The excitation frequency is generated by the rotation of a cylindrical valve and the amplitude is controlled by a feeding pump. For each excitation frequency, the forced harmonic response of the hydraulic system is measured with pressure sensors densely located along the hydraulic circuit. A spectral analysis of the forced harmonic response for all excitation frequencies is used to identify the eigenfrequencies of the system.

However, with the excitation system and the dissipation induced by the cavitation vortex rope, the system can be considered as excited and damped. Thus, the experimental frequency f_{exp} is slightly different than the undamped case defined by f_0 . Therefore, it is important to calculate the wave speed related to the natural frequency and the dissipation parameter simultaneously.

$$f_{exp} = f_0\sqrt{1-\zeta^2} \tag{3.7}$$

3.3 Experimental identification of wave speed

Instead of using Equation 3.6, a numerical model of the hydraulic system was developed and the wave speed is adjusted in the distributed draft tube modeling to obtain a numerical natural frequency similar to the experimental natural frequency. To identify the natural frequency of the numerical model, an eigenvalue study of the non-linear hydraulic system is conducted. The hydroacoustic modeling of the hydraulic system dynamics model is cast as a first order differential equation system in the following matrix form:

$$[A]\frac{d\vec{x}}{dt} + [B(\vec{x})]\cdot\vec{x} = \vec{V}(\vec{x}) \tag{3.8}$$

where $[A]$ and $\left[B\left(\vec{x}\right)\right]$ are the global state matrices of dimension $[n \times n]$, $\vec{x}$ and $\vec{V}\left(\vec{x}\right)$ are the state vector and the boundary conditions vector with n components, respectively. The eigenvalues are based on the linearization of the set of equations around the operating point [4]. Damping and oscillation frequency of the eigenmodes are given by the real part and the imaginary part of the eigenvalues, respectively.

Additionally, by injecting the value of the wave speed in Equation 3.1, the cavitation compliance can be determined:

$$C_c = \frac{-\partial V_c}{\partial h_{\bar{1}}} = \frac{gAdx}{a_{equ}^2} \tag{3.9}$$

By using the definition of the NPSE, see Equation 1.1, the previous equation can be rewritten as:

$$C_c = \frac{-\partial V_c}{\partial h_{\bar{1}}} = \frac{-\partial V_c}{\partial NPSE}\frac{\partial NPSE}{\partial h_{\bar{1}}} \approx -g\frac{\partial V_c}{\partial \sigma E} \tag{3.10}$$

For a given operating condition, E is considered as constant and the cavitation compliance can be defined as:

$$C_c = \frac{gAdx}{a_{equ}^2} \approx -\frac{1}{H_{turb}}\frac{\partial V_c}{\partial \sigma} \tag{3.11}$$

Thus, identifying the wave speed for several Thoma numbers for a constant operating condition and by integrating the previous equation, the volume of cavitation can be deduced:

$$V_c = -E\int \frac{Adx}{a_{equ}^2}\,\mathrm{d}\sigma \tag{3.12}$$

Now, dividing the volume of cavitation V_c by the total volume of the draft tube V_{tot} leads to the mean void fraction:

$$\beta = \frac{V_c}{V_{tot}} = -E\int \frac{1}{a_{equ}^2}\,\mathrm{d}\sigma \tag{3.13}$$

This value can be confirmed by analyzing the visualization of the cavitation vortex rope with a high speed camera, see Figure 3.3. The Plexiglas cone provides an optical access to the flow in the draft tube of the reduced scale physical model. Moreover, a highly uniform LED screen is installed as a backlight to produce good contrast between the gaseous and the liquid phases. To minimize the optical distortion effect, water-filled compartments with a flat surface are installed perpendicularly to the camera axis.

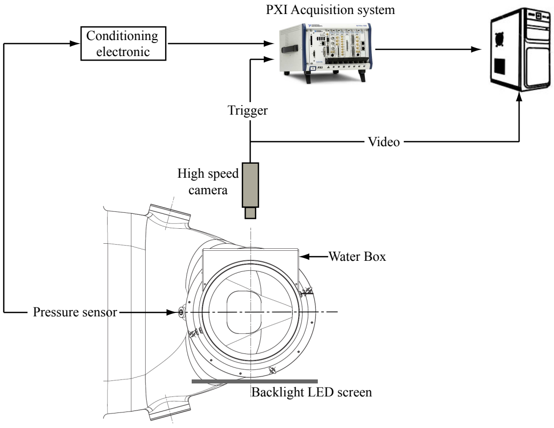

Figure 3.3: Setup for the visualisation of the cavitation vortex rope, synchronized with acquisition from pressure sensors.

Finally, this method allows to link the wave speed to the natural frequency, the Thoma number and the void fraction. This link also appears in the theoretical development of Rath [50] for bubbly flows. A comparison between the theoretical and experimental values will confirm whether the model for bubbly flows can be applied to a cavitation vortex rope in a Francis turbine or not.

3.4 Experimental identification of bulk viscosity

The bulk viscosity represents internal processes breaking a thermodynamic equilibrium between the cavitation volume and the surrounding liquid. To identify the energy dissipation induced by the bulk viscosity, it is essential to quantify the amount of energy injected in the hydraulic system at a given frequency. This measurement is performed with a Pressure-Time method using two pressure sensors located before the injection flow [28] and is described in the next subsection.

By injecting the same amount of energy in the numerical model, the bulk viscosity is simply adjusted in the draft tube modeling to obtain the same forced harmonic response measured experimentally. This comparison is focused on circular pipes connecting the upstream reservoir to the Francis turbine to reduce the uncertainty related to the experimental measurements. Indeed, on the one hand, without a draft tube, and therefore without vortex rope, it is not necessary to separate the synchronous from the convective part in experimental measurements.

On the other hand, without a Francis turbine, the pressure gradient associated with the hydraulic machine is not taken into account. It is also worth noting that for each calculated bulk viscosity, the wave speed is also adapted to retain a correct natural frequency, in accordance with Equation 3.7.

Moreover, the shape of the forced harmonic response depends essentially on the wave speed in the hydraulic pipes. This wave speed is related to the amount of gas dissolved in the water and therefore depends on the quality of the degassing procedure. By knowing the amount of gas dissolved in water, the wave speed is calculated using Rath's equation [50].

Finally, this method is applied to an off-resonance system to avoid energy transfer between the precession of the vortex rope and the excitation source. Therefore, this method can only be applied to partial load conditions. At full load operating conditions, the system may be self-excited and the volume of cavitation may oscillate at the natural frequency of the hydraulic system. However, the numerical results will be generalized with dimensionless relations in Chapter 6 in order to predict the hydroacoustic parameters for different Thoma and Froude numbers and thus predict the pressure and torque fluctuations of a reduced scale model of a Francis turbine.

3.4.1 Pressure-Time method

This procedure uses the conservation of momentum for inviscid, irrotational and incompressible pipe flows [28]. Neglecting the friction in a horizontal pipe without cavitation, the equation 2.7 can be rewritten as:

$$\frac{\partial C}{\partial t} + C\frac{\partial C}{\partial x} + \frac{1}{\rho_w}\frac{\partial p}{\partial x} = 0 \tag{3.14}$$

The integration of Equation 3.14 between two arbitrary points *1* and *2*, distant of L meters from one another, for a constant cross-section A produces:

$$\frac{\partial Q}{\partial t} = \frac{A}{\rho_w L}\left(p_1 - p_2\right) \tag{3.15}$$

Pressure and discharge variables can be represented as the sum of their mean and fluctuating parts:

$$Q = \bar{Q} + \tilde{Q} \qquad\qquad p = \bar{p} + \tilde{p} \tag{3.16}$$

With equations 3.15 and 3.16, the fluctuation part of the discharge is obtained by calculating the following integral:

$$\tilde{Q} = \frac{A}{\rho L}\int \left(\tilde{p}_1 - \tilde{p}_2\right) dt \tag{3.17}$$

Then, a spectral analysis of $\tilde{Q}$ is used to define the amount of energy injected into the hydraulic system for each excitation frequency. The accuracy of this method is discussed by Kashima *et al.* [34] and will be proven in Chapter 4.

3.5 Experimental identification of the pressure source

The methodology used to identify the pressure source is based on the excitation generated by the precession of the vortex rope. The excitation results from a strong interaction between the vortex rope and the elbow, leading to the pressure source located in the inner part of the elbow [7]. The use of an external excitation source is therefore not required for the identification of this hydroacoustic parameter. As the location of the pressure source is not perfectly defined, several locations along the draft tube will be tested. Moreover, the pressure source is modeled as a distributed source to reduce the impact of the discretization on the forced harmonic response. To reduce the number of dimensions of the problem and ease the optimization process, the pressure source S_h is modeled by a Gaussian curve.

$$S_h = Ae^{\left(-\frac{(x-L)^2}{2e^2}\right)} \tag{3.18}$$

This source, distributed in the cone and the elbow of the draft tube, is described by three mathematical parameters along the x-axis, see Figure 3.4.

- L represents the location of the center of the pressure source
- e corresponds to the standard deviation of the Gaussian curve
- A defines the amplitude of the Gaussian curve

To determine these three parameters, the experimental forced harmonic response of the hydraulic system excited by the precession of the vortex rope is compared with the response of the numerical model. The comparison is quantified for three different objectives to be met:

- The first objective compares the experimental forced response with the response of the numerical model with a specific focus on circular pipes connecting the upstream

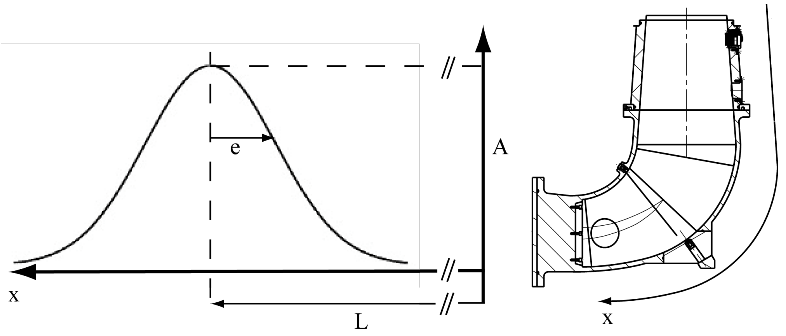

Figure 3.4: Representation of the Gaussian curve (Left) and the axis along the draft tube (Right).

reservoir to the Francis turbine. The advantage of focusing on this subset of the hydraulic system reduces the uncertainty related to the experimental measurements and thus increases the weight of this objective. Indeed, on the one hand, without a draft tube, and therefore without vortex rope, it is not necessary to separate the synchronous from the convective part in experimental measurements. On the other hand, without a Francis turbine, the pressure gradient associated to the hydraulic machine is not taken into account.

- With four pressure sensors in a section of the cone, it is possible to separate the synchronous part from the convective part and to compare the synchronous value with the numerical model. The weight of this objective is significant because of its low uncertainty.
- The pressure sensors located in the elbow and the diffuser of the draft tube can also be used as a benchmark to identify the pressure source induced by the vortex rope. Due to the non-circular sections, the uncertainty of the pressure measurements is high and the weight of this objective is reduced.

Given the number of objectives and the number of unknown parameters, several local minima may exist and a dichotomy or a multigrid algorithm is not guaranteed to converge to the global minimum. Therefore, a multi-objective genetic algorithm has been implemented to quantify the pressure source. In a genetic algorithm, a population of candidate solutions to an optimization problem is evolved towards better solutions. The evolution usually starts from a population of randomly generated individuals and in each generation, the suitability of every individual in the population is evaluated with the objectives defined above. The most relevant individuals are selected from the current population and form a new generation. The new generation of candidate solutions is then used in the next iteration of the algorithm. Commonly, the algorithm comes to an end when a satisfactory acceptability level has been reached for the population.

This algorithm is applied to different discharge factors Q_{ED} and Thoma and Froude numbers to study their impact. However, to decrease the number of solution satisfying the different objectives, it is assumed that the shape of the pressure source is independent of the Thoma number. In other words, the precession of the flow is not affected by the pressure level at the turbine outlet. This assumption is coherent because, for a constant Q_{ED} and Froude numbers, the outlet velocity triangle is not affected by the setting level h_s. Therefore, the location of the pressure source L and the standard deviation e will be evaluated by minimizing the error on all Thoma numbers, for a constant pair of discharge factor and Froude number.

Moreover, the analysis of the amplitude A as a function of Thoma number will validate or disprove the Dörfler's assumption whereby the amplitude of the pressure source is independent of the Thoma number. He assumes that the swirl momentum induced by the runner is only slightly affected by the cavitation [46].

Finally, the study of the standard deviation e will determine whether the pressure source must be lumped or distributed in the draft tube to better simulate the vortex rope.

3.6 Description of the identification algorithm

The identification of the hydroacoustic parameters is performed in the frequency domain by using two different excitation systems. In the first of them, the wave speed and the bulk viscosity are identified using an external excitation system generated by the rotation of a cylindrical valve. In the second of them, the pressure source characterized by three parameters is determined using the excitation generated by the precession of the vortex rope. As the methodology is applied to an off-resonance system to avoid energy transfer between the precession of the vortex rope and the external excitation source, there is no interaction between the vortex rope and the natural frequency in the frequency domain. Hence, the wave speed and the bulk viscosity can be identified separately from the pressure source.

3.6.1 Algorithm for wave speed and bulk viscosity

For a given operating condition, an external excitation system is designed to identify the experimental natural frequency. The hydraulic system being excited and damped, the natural frequency and the dissipation are coupled and must be calculated simultaneously. Thus, the algorithm minimizes two different objectives:

- Identification of the wave speed value in the distributed draft tube modeling to obtain a numerical natural frequency similar to the experimental natural frequency.

- Identification of the bulk viscosity value in the draft tube modeling to obtain the same forced harmonic response measured experimentally.

Algorithm for wave speed

The first objective is to identify a couple (a, μ'') for which the numerical model exhibits a natural frequency similar to that of experimental measurements. To choose the most efficient algorithm, a sensitivity analysis is required.

The behavior of the natural frequency as a function of the wave speed for a non-dissipative system is shown in Figure 3.5 (Left). As highlighted in equation 3.6 for low wave speeds, the natural frequency changes linearly. However, for high wave speed, assumption 3.1 is no longer valid, the hydraulic capacitance of the pipes is no longer negligible and the curve approaches a horizontal asymptote. Thus, the function between the wave speed and the natural frequency is strictly increasing for cavitating flow. It exists a unique global minimum and therefore a unique wave speed for a given natural frequency. Moreover, knowing neither the analytical function nor its derivative, simple and robust algorithms such as the dichotomy or the multi-grid algorithms can be used to determine the global minimum for a non-dissipative system.

The behavior of the natural frequency as a function of the bulk viscosity for a constant wave speed is described in Figure 3.5 (Right). The quadratic behavior of this curve is related to the equation 3.7. It exists a unique global minimum and therefore a unique bulk viscosity for a given wave speed. Simple and robust algorithms such as the dichotomy or the multi-grid algorithms can also be used to identify the unique global minimum.

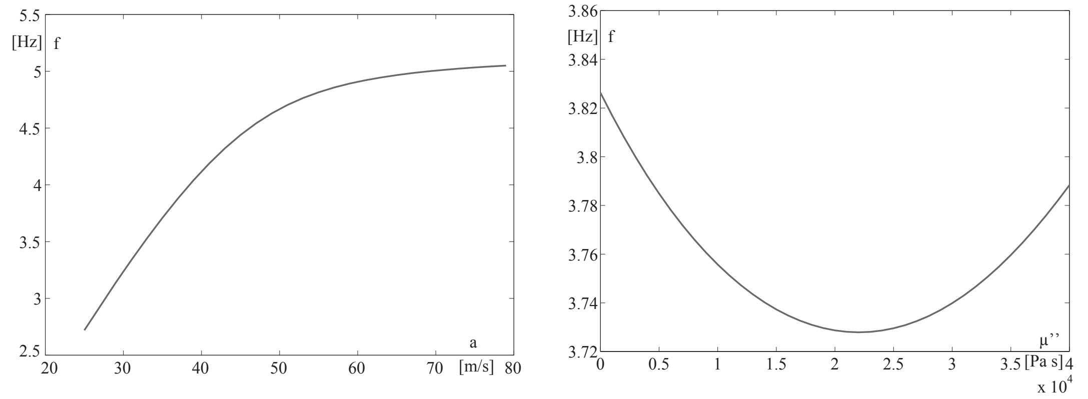

(a) For an undamped hydraulic system

(b) For a constant wave speed

Figure 3.5: Behavior of the natural frequency as a function of wave speed (Left) and bulk viscosity (Right).

The error on the numerical natural frequency f_{num} as a function of the wave speed and the bulk viscosity is defined by Equation 3.19 and is shown in Figure 3.6 (Left).

$$Error = \frac{|f_{num} - f_{exp}|}{f_{exp}} \tag{3.19}$$

Thus, the increase in bulk viscosity is accompanied with an increase in wave speed to maintain a constant natural frequency. Moreover, for a given bulk viscosity, the behavior of the error is similar to the case without dissipation and therefore there is a unique wave speed to minimize the error on the natural frequency. The use of a dichotomy algorithm is, thus, justified. Finally, the coupling between the wave speed and the bulk viscosity is highlighted by the red curve in Figure 3.6 (Right), illustrating the minimum error for each bulk viscosity.

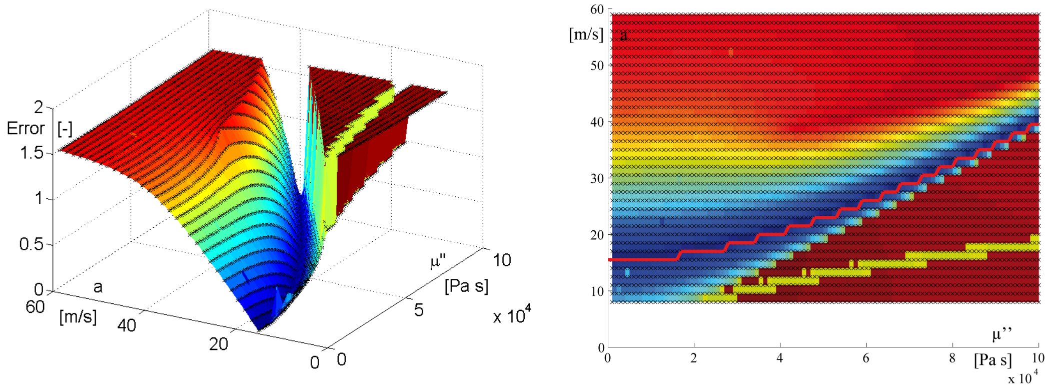

(a) 3D view of the error on natural frequency

(b) View in the XY Plane

Figure 3.6: Error on the natural frequency as a function of wave speed and bulk viscosity.

Algorithm for bulk viscosity

The second objective of this algorithm is to determine the bulk viscosity to obtain a forced harmonic response of the numerical model similar to the experimental forced harmonic response. The amount of energy exciting the hydraulic system is quantified with the Pressure-Time method, see Equation 3.17, and is injected into the numerical model. This identification is applied out of resonance to avoid any exchange of energy between the vortex rope excitation and the external excitation system. The error on the forced harmonic response (FHR) for a pressure sensor at the turbine inlet is defined by the equation 3.20 and shown in Figure 3.7.

$$Error = \frac{|FHR_{num} - FHR_{exp}|}{FHR_{exp}} \tag{3.20}$$

At high bulk viscosity, all the injected energy is dissipated and the function approaches a horizontal asymptote. For low bulk viscosities, the function is convex and has therefore a unique global minimum. Then, this second objective can be minimized with a simple and robust algorithm such as the dichotomy.

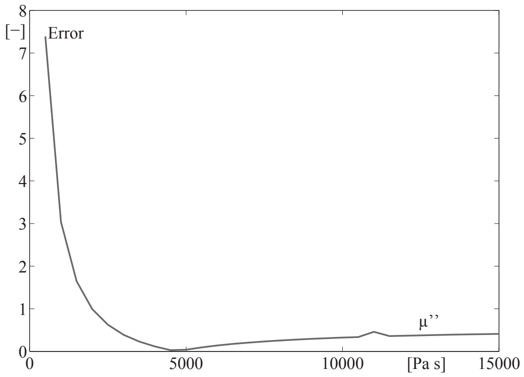

Figure 3.7: Error on the forced harmonic response as a function of bulk viscosity.

Description of the procedure

The algorithm to identify the wave speed and the bulk viscosity is illustrated in Figure 3.8 and described by the following procedure:

1. **Identification of the experimental natural frequency** f_{exp} with an external excitation system for a given operating condition.

2. **Calculation of the amount of energy** S_{exp} exciting the hydraulic system with the Pressure-Time method.

3. **Selection of an initial bulk viscosity** μ''. The numerical value of this parameter is small for large cavitation volumes.

4. **Selection of an initial wave speed** with Equation 3.7.

5. **Application of a dichotomy algorithm to identify the wave speed** for a given bulk viscosity μ'' and a given frequency f_{exp}. The error must be less than the frequency resolution required for the spectral analysis.

6. **Application of a dichotomy algorithm to identify the bulk viscosity**. The error on the forced harmonic response must be less than a tolerance defined according to the studied hydraulic system.

7. **Identification of the wave speed and the bulk viscosity**. The procedure described in points 1 to 6 can be reapplied to a different Thoma number.

8. **Calculation of the mean cavitation volume and the void fraction** for different Thoma number with Equations 3.12 and 3.13.

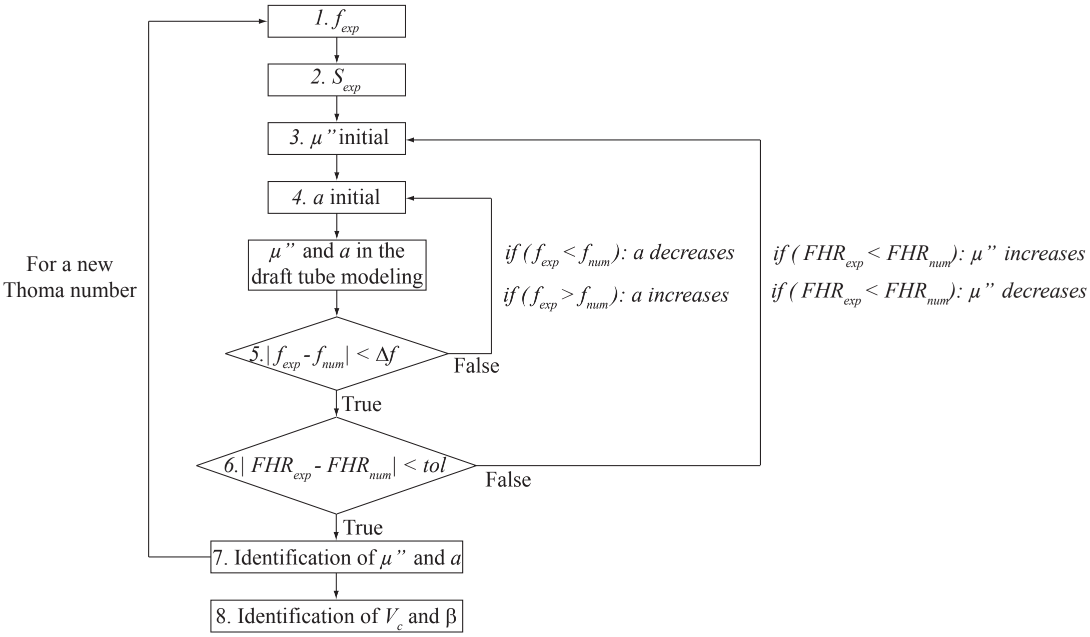
1. f_{exp}
2. S_{exp}
3. μ'' initial
4. a initial
μ'' and a in the draft tube modeling
5. $|f_{exp} - f_{num}| < \Delta f$
False
True
6. $|FHR_{exp} - FHR_{num}| < tol$
False
True
7. Identification of μ'' and a
8. Identification of V_c and β
For a new Thoma number
if ($f_{exp} < f_{num}$): a decreases
if ($f_{exp} > f_{num}$): a increases
if ($FHR_{exp} < FHR_{num}$): μ'' increases
if ($FHR_{exp} < FHR_{num}$): μ'' decreases

Figure 3.8: Synoptic scheme of the algorithm to identify wave speed and bulk viscosity.

3.6.2 Algorithm for the pressure source

The pressure source is modeled by a Gaussian curve characterized by three linearly dependent parameters. Therefore, several local minima may exist and simple algorithms such as the dichotomy cannot be used because of their strong dependence on the initial point provided. To locate the global minimum, the three parameters are identified with a multi-objectives genetic algorithm. This method of numerical analysis can be summarized in five steps, see Figure 3.9 :

1. **Initially, many individual solutions are randomly generated** to form an initial population. Population size and search space are defined by the nature of the problem (length of the cone and the elbow, amplitude of the excitation induced by the vortex rope, ...)
2. **The suitability of every individual in the population is evaluated** with the objective functions. In this context, the objective functions depend on the forced harmonic response measured by pressure sensors located throughout the hydraulic system. Depending on the location of the pressure sensors and thus their quality measurement, the objectives are given more or less weight in the evaluation.
3. **A proportion of the existing population is selected** to breed a new generation.
4. **A new population of solutions is generated** from those selected. The solutions of the new generation, named “children”, share many characteristics with the previous gen-

eration, named “parents”. Thus, new parents are selected for each new child and this process continues until the new generation of solutions reaches the appropriate size.

5. **This generational process is repeated** until a solution is found that satisfies minimum criteria, or until the maximum number of generations is reached.

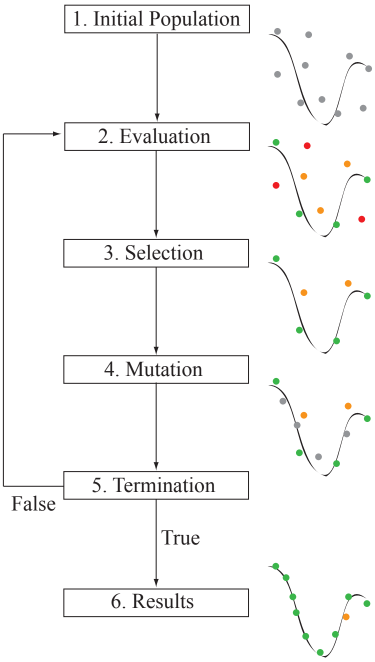

Figure 3.9: Synoptic scheme of the genetic algorithm used to identify the pressure source.

3.7 Summary and discussion

The methodology to identify the hydroacoustic parameters at part load conditions was presented in this chapter. The wave speed and the bulk viscosity are determined in the frequency domain and need the development of an external excitation source and the characterization of the experimental natural frequency. A sensibility analysis justified the existence of a global minimum and therefore the use of a simple and robust algorithm such as the dichotomy.

The pressure source is modeled by a Gaussian curve characterized by three linearly dependent parameters. Therefore, several local minima may exist and simple algorithms such as the dichotomy cannot be used because of their strong dependence on the initial point. To identify the global minimum, the three parameters are identified with a multi-objective genetic algorithm. However, to decrease the number of solutions satisfying the different objectives, it is assumed that the location of the pressure source L and the standard deviation e are independent of the Thoma number.

Finally, this methodology can be applied to any hydraulic system comprised of a Francis turbine and a draft tube. Using a rotating valve and a few pressure sensors located along the hydraulic system, the harmonic forced response and the natural frequency are measured. Then, with an accurate numerical model, the wave speed, the bulk viscosity, the cavitation volume, the void fraction and the pressure source induced by the vortex rope can be identified. A generalization of these hydroacoustic parameters with dimensionless relations will allow predicting the hydroacoustic parameters for different Thoma and Froude numbers and thus allow predicting the pressure and torque fluctuations of a reduced-scale physical model of a Francis turbine for different operating conditions.

4 Experimental Instrumentation Setup

4.1 Model Testing Facilities

A reduced-scale physical model of a Francis turbine with a specific speed of $\nu = 0.27$ was installed on the EPFL test rig PF3 of the Laboratory for Hydraulic Machines, shown in Figure 4.1. The prototype generating unit, featuring a rated power of 444 MW, is located in a power plant in the Canadian province of British Columbia. The test rig allows for performance assessments within an accuracy of 0.2 %, complying with the IEC standards [55]; these performance assessments are usually performed to predict and evaluate the behavior of hydraulic prototypes. The test rig is operated in a closed loop configuration driven by two 400 kW centrifugal pumps connected in series and applying a maximum head of 100 m. The rotating speed of the runner is regulated by a generator and the discharge is controlled by the guide vane opening. Finally, the pressure level in the draft tube is set by adjusting the pressure in the downstream reservoir with a vacuum pump.

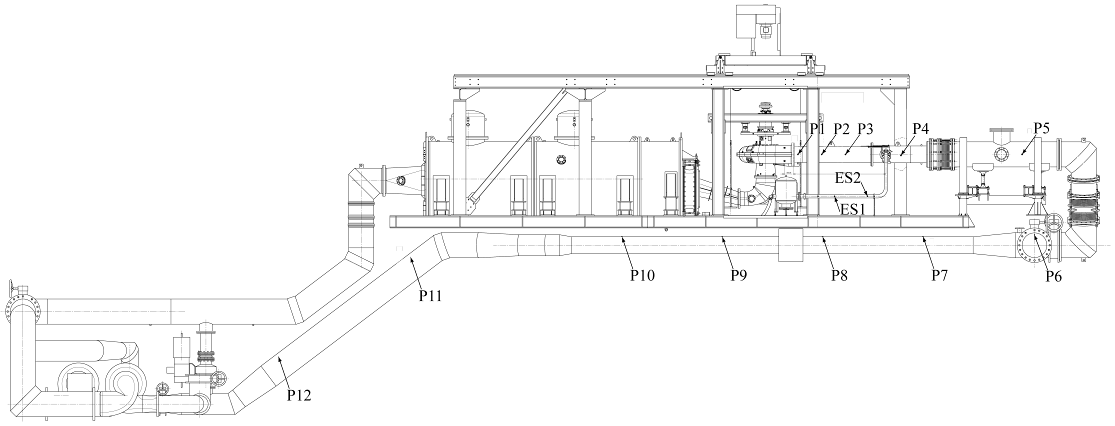

Figure 4.1: EPFL test rig PF3 drawn with the excitation system and locations of dynamic pressure sensors.

4.2 Pressure Measurements Instrumentation

Dynamic wall pressure measurements are carried out by making use of flush-mounted piezoresistive pressure sensors [25]. Their main characteristics are summarized in Table 4.1. Output signals of the pressure sensors are amplified with a gain of either 10 or 100 depending on the pressure measurements range, and then are simultaneously acquired during three-minute runs on a NI PXI-1033 acquisition device. The sampling frequency is set to 1000 Hz to capture all physical phenomena that could influence hydroacoustic parameters. Finally, since pressure signals for a part load operating condition are not perfectly periodic, a Hamming window is applied to the spectral analysis. This window is commonly used in practice to eliminate the discontinuities at the beginning and end of records. Overlapped processing techniques are also used to counteract the increase in variability caused by the time history tapering for side-lobe suppression [10]. A common selection in overlapped processing is a 50% overlap.

Table 4.1: Piezoresistive pressure sensors characteristics.

Characteristic	Value
Measurement range	0 ÷ 5 bars
Maximum measurement uncertainty	0.7 ‰
Bandwidth	0 ÷ 25 kHz

Wall pressure measurements are performed in the draft tube, in the turbine, and in the test rig. The location of the dynamic pressure sensors on the EPFL test rig PF3 are summarized in Appendix B. Twelve pressure sensors are located along the test rig pipe (*P1-P12*), 8 pressure sensors are located in the cone on two different sections turned 90° from one another, 2 pressure sensors are installed in the elbow (*E1-E2*) and finally 4 pressure sensors are located in the diffuser (*D1-D4*), see Figure 4.2. The two last pressure sensors (*GV-NE* and *GV-SW*) are located between the guide vanes. The pressure sensor *P1* at the turbine inlet will be considered thereafter as the reference sensor for all analyzes in the frequency domain. It is interesting to note that the location of the sensors is deliberately concentrated in the draft tube and on the first part of the test rig to reduce the error of the eigenshape measurements. These measurements are synchronized with the test rig parameters measurement, such as Thoma number, head, discharge and torque.

4.3 Overview of pressure fluctuations

A waterfall diagram with a cross spectral density function of the *P1* and *C1N* pressure sensors at plant value of Thoma number is illustrated in Figure 4.3. The discharge factor Q_{ED} is divided by the Q_{ED} at the best efficiency point (BEP). The resonance phenomenon observed at Q_{ED} = 77.6% of the discharge at the BEP occurs when the frequency of the vortex rope precession matches the first eigenfrequency of the test rig, as reported by Favrel *et al.* [26].

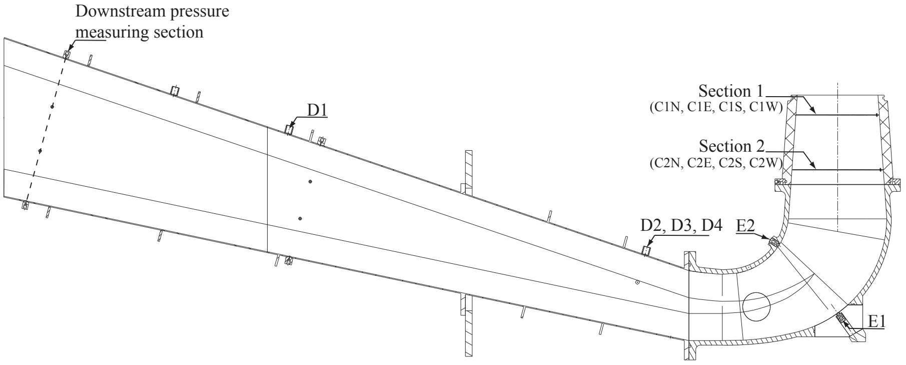
Downstream pressure measuring section
D1
Section 1
(C1N, C1E, C1S, C1W)
Section 2
(C2N, C2E, C2S, C2W)
D2, D3, D4
E2
E1

(a) Cut through Section A-A

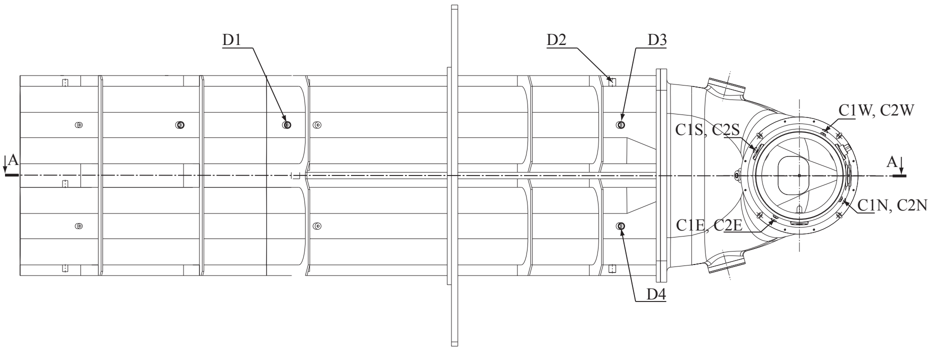
D1
D2
D3
A
A
C1W, C2W
C1S, C2S
C1N, C2N
C1E, C2E
D4

(b) Top view

Figure 4.2: Close view of the draft tube.

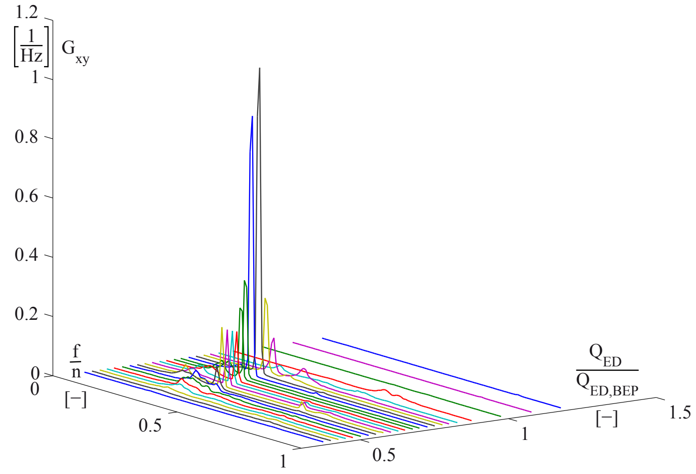

Figure 4.3: Cross spectral density function of the *P1* and *C1N* pressure sensors at $\sigma = 0.11$ and Fr = 8.75 over loads ranging from of 40% to 120%.

Globally, the discharge factor reduction imposes an almost linear increase of vortex rope precession frequency for a constant rotating speed, see Figure 4.4. Nevertheless, a first level occurs between 45 and 55 % of Q_{ED} at BEP. A second level is also present near BEP. Finally, according to Yamamoto *et al.* [64], a linear increase in vortex rope frequency also occurs at deep part load with a steeper slope. Because of this change in behavior from the vortex rope frequency, the study is conducted in two different operating ranges: the first operating condition *PL1* is located at 80% of the Q_{ED} at BEP, the second operating condition *PL2* is located at 64% of the Q_{ED} at BEP. The analysis of these two operating conditions is realized in both cavitation-free and cavitating conditions for different Froude number. A summary of the operating conditions is described in the Table 4.2.

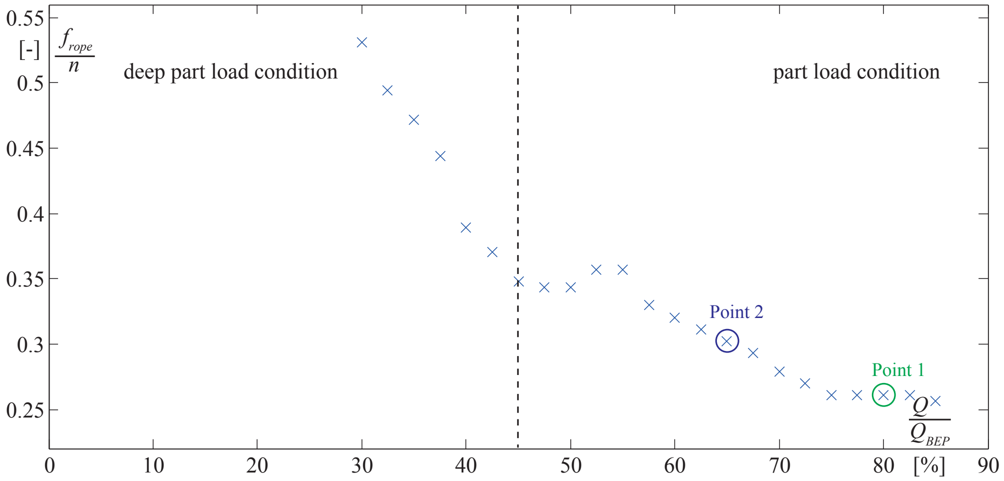

Figure 4.4: Evolution of vortex rope precession as a function of discharge factor Q_{ED} for a Froude number Fr = 8.75.

Table 4.2: Selected Francis turbine operating conditions.

		$n_{ED}/n_{ED,BEP}$	$Q_{ED}/Q_{ED,BEP}$	Fr	σ
PL1	Part Load	1	0.80	[6.56, 7.66, 8.75, 9.85]	[0.06 - 0.15]
PL2	Part Load	1	0.64	[7.66, 8.75, 9.85]	[0.11 - 0.20]

By studying data from pressure sensors in the frequency domain, it is possible to identify the natural frequency of the hydraulic system if the measurements are carried out near resonance. Indeed, under these conditions, the energy present at vortex rope frequency is sufficient to excite the first eigenmode of the test rig. Away from resonance, it becomes impossible to determine with certainty the natural frequency of the test rig. Thus, as this information is essential to identify hydroacoustic parameters, an excitation system is set up.

4.4 Excitation system

4.4.1 Design of the excitation system

Characterization of test rig eigenmodes is determined in a spectral analysis with an external excitation source. This excitation source is designed and constructed to inject or extract a periodical discharge at a given frequency in the upstream pipe, see Figure 4.5. A similar excitation system with the same rotating valve has been studied by Blommaert in 2000 [11] to actively reduce hydraulic fluctuations at a precise frequency. The excitation system uses a variable speed pump KSB Movichrom G 15/5 which allows to control the amplitude of excitation. This pump features a rated power of 5.5 kW and a rated rotating speed of 2'900 rpm. The pump location is 4 m below the reservoir to prevent local occurrence of cavitation and respect the NPSH value imposed by the manufacturer. This particularity is not represented in Figure 4.5 for simplicity. The modulation of the discharge is achieved through a custom-made rotating valve. This valve is driven by a variable speed motor enabling to excite the hydraulic test rig at frequencies ranging from 1 Hz to 15 Hz. Moreover, an air vessel ensures hydroacoustic decoupling between the injection pump and the entire hydraulic circuit. Finally, two pressure sensors (*ES1* and *ES2*) are installed on the excitation system pipe to measure the fluctuating discharge with a Pressure-Time method. This excitation system is mainly composed of simple elements and may be easily modeled. Only the custom-made rotating valve is difficult to characterize and requires further study.

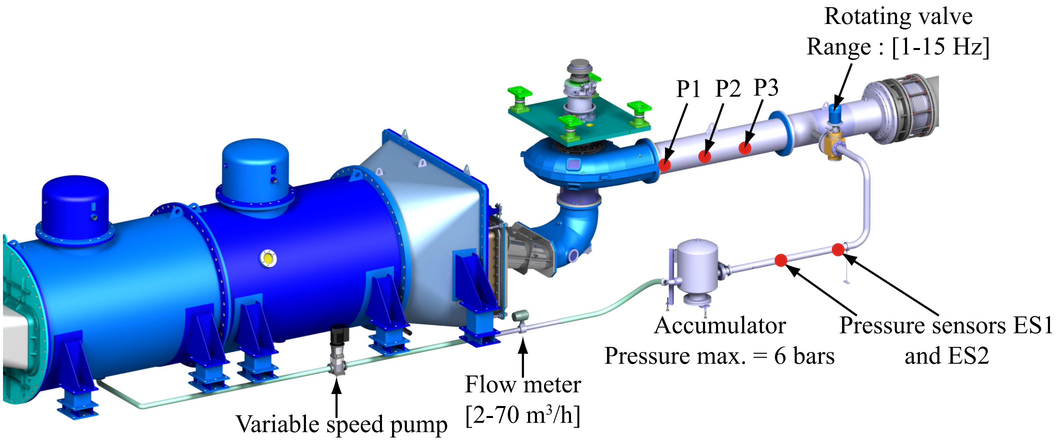

Figure 4.5: CAD model of the excitation system.

4.4.2 Characterization of the rotating valve

To model the rotating valve illustrated in Figure 4.7, the characteristic curve is determined on the EPFL test rig PF4 of the Laboratory for Hydraulic Machines, shown in Figure 4.6 [29]. Different components constitute this independent close hydraulic loop:

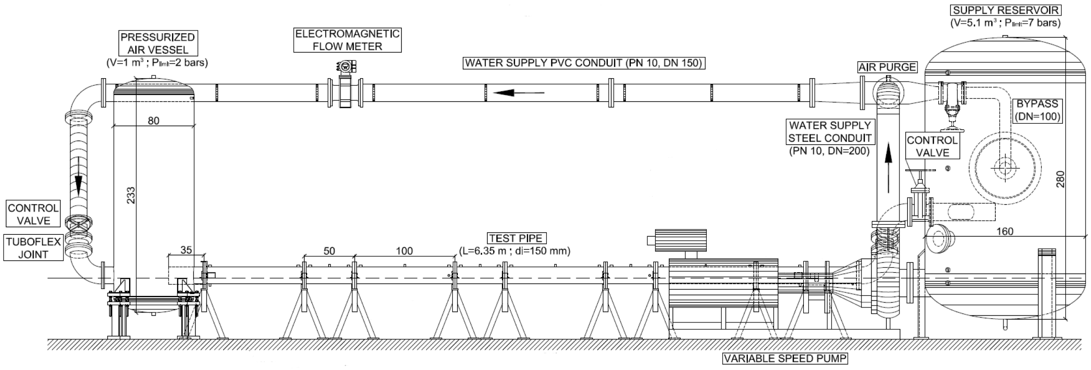
SUPPLY RESERVOIR
(V=5.1 m³ ; Plimit=7 bars)
PRESSURIZED AIR VESSEL
(V=1 m³ ; Plimit=2 bars)
ELECTROMAGNETIC FLOW METER
WATER SUPPLY PVC CONDUIT (PN 10, DN 150)
AIR PURGE
BYPASS (DN=100)
WATER SUPPLY STEEL CONDUIT (PN 10, DN=200)
CONTROL VALVE
80
233
280
160
CONTROL VALVE
TUBOFLEX JOINT
35
50
100
TEST PIPE
(L=6.35 m ; di=150 mm)
VARIABLE SPEED PUMP

Figure 4.6: Side view of EPFL test rig PF4.

- The variable speed pump of test rig is of type "*Sulzer G7 200-500*" with a maximum rotating speed of 1000 rpm. The pump is controlled by an electrical drive with a manual potentiometer for rotating speed adjustments.
- The supply reservoir is made of steel and has a cylindrical shape of 2.8 m in height and 1.6 m in diameter. Its capacity is equal to 5.1 m^3.
- The pressurized air vessel is a cylindrical tank having a water capacity of 1 m^3. The maximum admissible internal pressure inside the vessel is limited to 2 bars. It dynamically decouples the injection pump from the entire hydraulic circuit.
- A 10 m long PVC supply pipe of internal diameter 0.15 m connects the pump to the pressurized air vessel.
- Integrated in the PVC supply is a "*Proline Promag 50 W*" electromagnetic flow meter, providing a mean value of the discharge.
- Steel pipes connect the pressurized air vessel to the supply reservoir. A reduced section is imposed 0.65 m before the rotating valve to prevent recirculation close to the valve.

For steady flow, measurements of mean discharge and mean pressure upstream and downstream of the valve are used to quantify the energy loss coefficient for different opening angles of the valve. Five measurement sections are used to determine energy losses imposed by the valve for different opening angles, see Figure 4.8. Each section is composed of 4 pressure taps connected together to a dynamic pressure sensor. This configuration allows for mean pressure

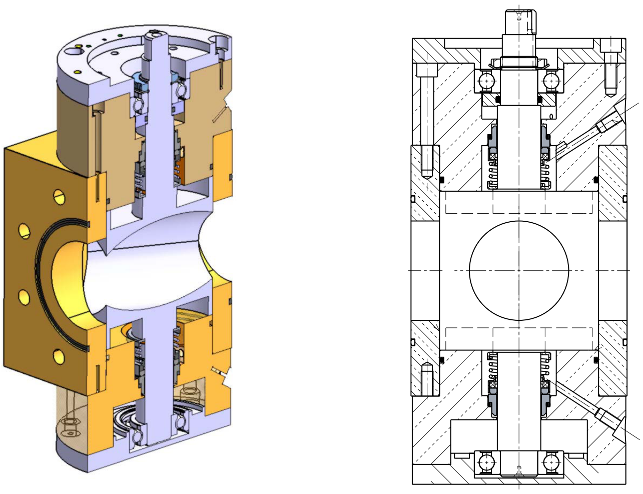

Figure 4.7: Rotating valve of the excitation system.

measurement for each instrumented section. For several opening angles, the mean discharge and the mean pressure are measured for five rotating speed of the pump: 300, 350, 400, 450, and 500 rpm.

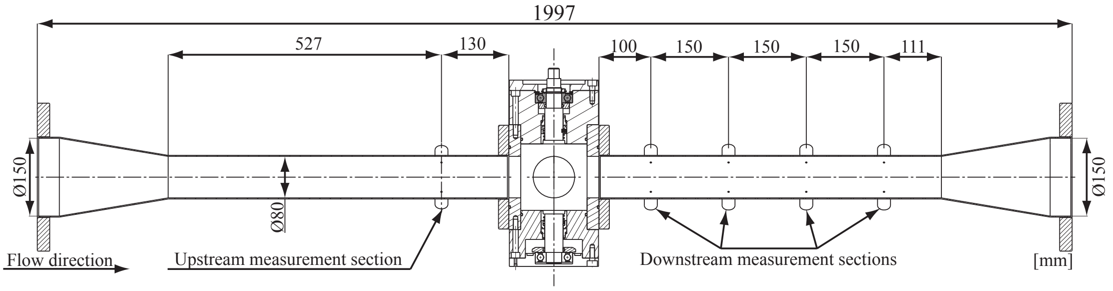
1997
527
130
100
150
150
150
111
Ø150
Ø80
Ø150
Flow direction
Upstream measurement section
Downstream measurement sections
[mm]

Figure 4.8: Location of measurement sections on EPFL test rig PF4.

Using different measurement sections located downstream of the valve, it is possible to verify that the energy loss for a stationary homogeneous flow in a circular steel pipe can be approximated with the Darcy-Weisbach friction equation 4.1 [63] and the Moody chart to compute the friction factor λ.

$$gH_r = \frac{\lambda Q|Q|}{2gDA^2} \tag{4.1}$$

where D is the diameter of the pipe and A defines pipe area. By applying this formulation, the pressures at inlet and outlet of the valve are computed and therefore specific energy losses of the valve ΔgH_v are determined. According to Avellan [8], the singular specific energy loss coefficient between inlet and outlet of the valve is defined as:

$$K_v = \frac{\left(\frac{p_{inlet}}{\rho_w} + gZ_{inlet}\right) - \left(\frac{p_{outlet}}{\rho_w} + gZ_{outlet}\right)}{\frac{Q^2}{2A^2}} = \frac{\Delta g H_v}{\frac{Q^2}{2A^2}} \tag{4.2}$$

The results obtained are presented in Figure 4.9a for five rotating speeds of the pump and several opening angles between 0 and 60 °. For larger openings, discharge falls to zero and the valve is considered closed. Thus, discharge fluctuations imposed by the rotating valve will not be sinusoidal and will certainly generate harmonics.

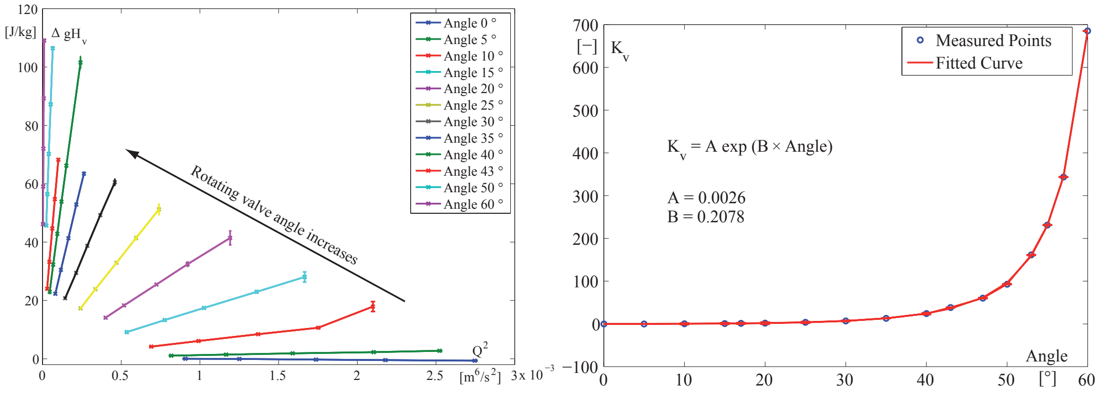

(a) Specific energy losses $\Delta g H_v$ as a function of Q^2

(b) Specific energy loss coefficient K_v as a function of opening angle

Figure 4.9: Experimental characteristic curve of the rotating valve.

Thus, as mentioned in equation 4.2, the relation between Q^2 and the specific energy loss is constant, whatever the rotating speed of the pump. These relatively clear results confirm the method used to determine the energy loss coefficient as a function of opening angle. Finally, numerical values of the energy loss coefficient for different opening angles may be approximated by an exponential curve defined in Figure 4.9b. With this characteristic curve, the rotating valve behavior can be modeled.

Finally, to validate the characteristic curve of the rotating valve, the methodology is to compare the experimental dynamic behavior with a numerical model of EPFL test rig PF4. To obtain an unsteady flow, the valve is driven by a variable speed motor at a given frequency and the dynamic pressure and discharge are measured. To describe the unsteady flow, eight dynamic pressure sensors are this time flush-mounted on the steel pipes, see Figure 4.10. For each section, two pressure sensors are placed turned 180° from one another. The measurement section downstream of the valve is located farther than seven times the pipe diameter in order to avoid recirculation zones.

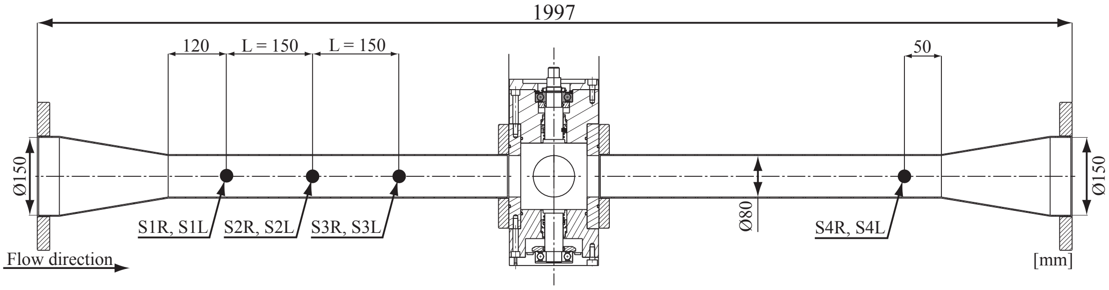

Figure 4.10: Location of the flush-mounted pressure sensors on EPFL test rig PF4.

In addition to instantaneous pressure, three sections upstream of the valve determine the fluctuating discharge of the pipe. This computation can be determined with the Pressure-Time method derived from the Navier-Stokes equations and defined by Equation 3.17. Thus, with the two pressure sensors, the fluctuating discharge and fluctuating pressure can be measured experimentally.

A numerical model of the PF4 test rig is derived by using the software SIMSEN. The model simply consists of two infinite tanks connected by steel pipes; the difference of water level is defined by the head of the pump. The modeling of pipes and tanks are widely described in the next chapter. Pressure losses caused by the rotating valve are modeled by the characteristic curve defined by the static study. A comparison of fluctuating pressure and fluctuating discharge experimentally and numerically obtained with a rotating valve are presented in Figure 4.11 in the frequency domain.

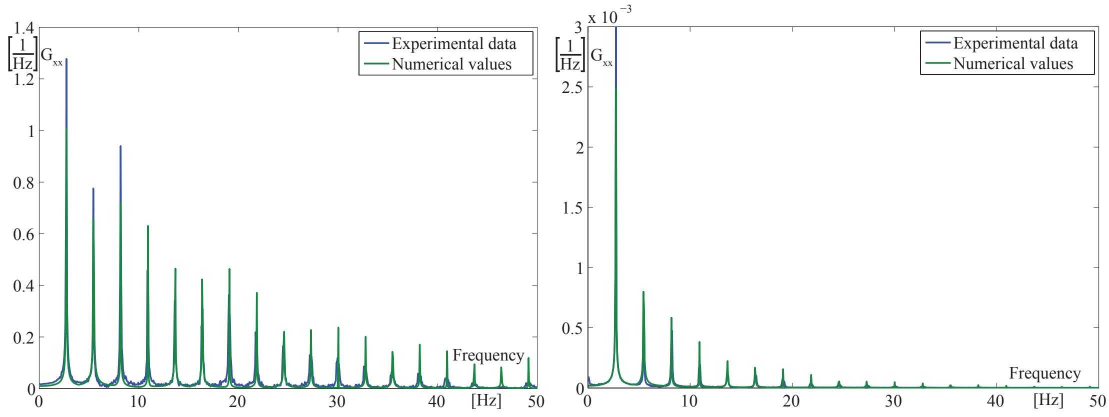

(a) For pressure measurement

(b) For discharge measurement

Figure 4.11: Comparison of cross spectral density functions from experimental data and numerical values, at excitation frequency equal to 2.75 Hz.

The good agreement between experimental and numerical G_{xx} for the pressure sensor *S1R* indicates a good characterization of the rotating valve. Moreover, as previously pointed out, the fact that no flow can pass through the valve at an opening angle greater than 60 degrees, generates the occurrence of harmonic. It will therefore be important to excite the first eigenmode of EPFL test rig PF3 with a frequency close to the first natural mode to avoid any interaction with the harmonics originating from the valve. Finally, the good agreement between experimental and numerical G_{xx} discharge indicates that the presented method to experimentally compute the fluctuating discharge provides good results. Thus, the assumptions described in Subsection 3.4.1 do not influence the computation of the fluctuating discharge much. Therefore, this Pressure-Time method will be used to calculate the discharge source injected in the PF3 test rig by using two experimental signals of the dynamic pressure sensors.

Since the modeling of the rotating valve is now known and validated, it is possible to excite the EPFL test rig PF3 with the subsystem described in subsection 4.4.1 to determine the eigenmodes of the hydraulic system.

4.4.3 Test rig excitation

With the excitation system, it is possible to determine the first eigenfrequencies for all operating conditions of the Francis turbine. For instance, for given Q_{ED}, Froude and Thoma numbers, the hydraulic system is experimentally excited in a frequency range to determine the eigenmode of the test rig. For each excitation frequency, the forced harmonic response is measured with 27 pressure sensors located on the test rig. The number of channels in the acquisition system being limited to 28 pressure sensors, the use of sensors *ES1* and *ES2* to quantify the fluctuating discharge injected by the excitation system requires the disconnection of two other pressure sensors: *E2* and *D4*. Moreover, the use of a flowmeter to determine the mean flow injected by the excitation system requires the disconnection of a sensor from the turbine: *GW-NE*.

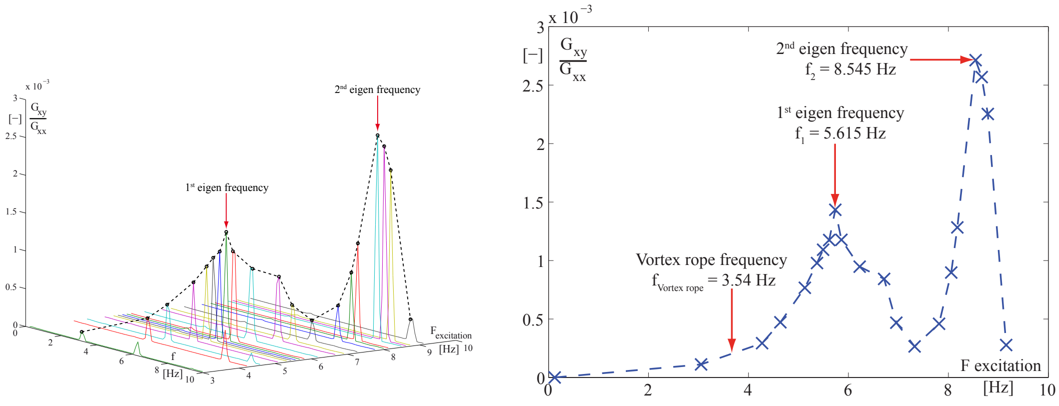

(a) Spectrum obtained for each excitation frequency (b) Amplitude obtained for each excitation frequency

Figure 4.12: Cross spectral density function of *P1* and *ES1* pressure sensors, divided by the one-sided autospectral density function of the reference sensor *P1* located at the turbine inlet.

The cross spectral density function G_{xy} of the two pressure sensors, named *P1* and *ES1*, is computed and divided by the one-sided autospectral density function G_{xx} of the reference sensor *P1*, located at turbine inlet. For instance, Figure 4.12a shows the hydraulic test rig response for 21 excitation frequencies for the *PL1* operating condition with a Froude number equal to 8.75 and a Thoma number equal to 0.15. The amplitude obtained for each given excitation frequency is plotted in Figure 4.12b. The two peaks highlighted by the red arrows indicate the first and second eigenfrequencies of the hydraulic system.

Figure 4.13 described the shape of the hydraulic EPFL test rig PF3 response for the first and the second eigenfrequencies. Each value represents the cross spectral density function G_{xy} of a pressure sensor with the reference sensor *P1*, divided by the one-sided autospectral density function G_{xx} of the reference sensor.

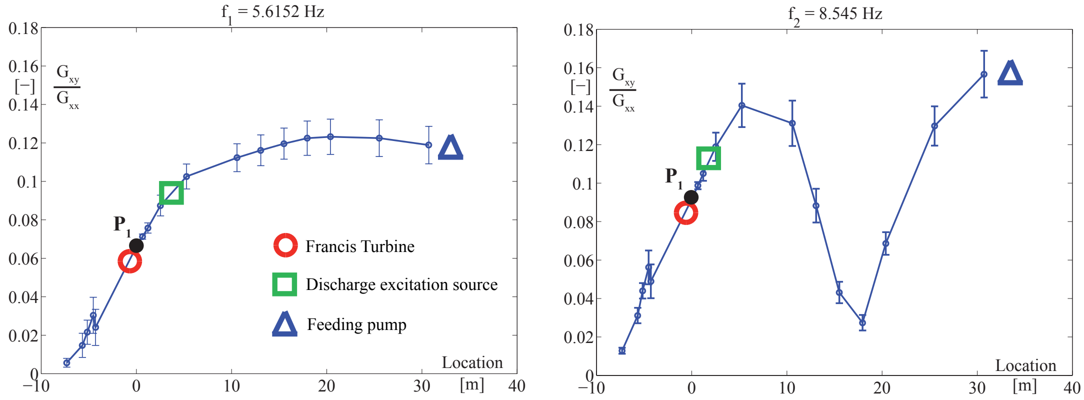

Figure 4.13: The hydraulic response on EPFL test rig PF3 for first and second eigenmodes.

Figure 4.14 shows the relation between the Thoma number and the first eigenfrequency of the hydraulic system obtained by applying the same methodology for all Thoma numbers, Froude numbers and Q_{ED} values. Globally, the natural frequency increases relatively linearly as a function of Thoma number when the volume of cavitation decreases. In addition, Froude number influence remains small and its decrease causes a slight reduction in eigenfrequency. Physically, the Froude number affects the distribution of cavitation in the flow as it determines the pressure gradient relatively to the size of the machine. Finally, the difference between the two operating conditions *PL1* and *PL2* is related to the pressure level in the draft tube.

4.5 Summary and discussion

A reduced-scale physical model of a Francis turbine was installed on EPFL test rig PF3 of the Laboratory for Hydraulic Machines. This test rig allows for performance assessments within an accuracy of 0.2 %, complying with the IEC standards. A waterfall diagram at Thoma number of the power plant indicates a resonance phenomenon at Q_{ED} = 77.6% of discharge at BEP. Evolution of vortex rope precession frequency as a function of Q_{ED} is linear at part load and

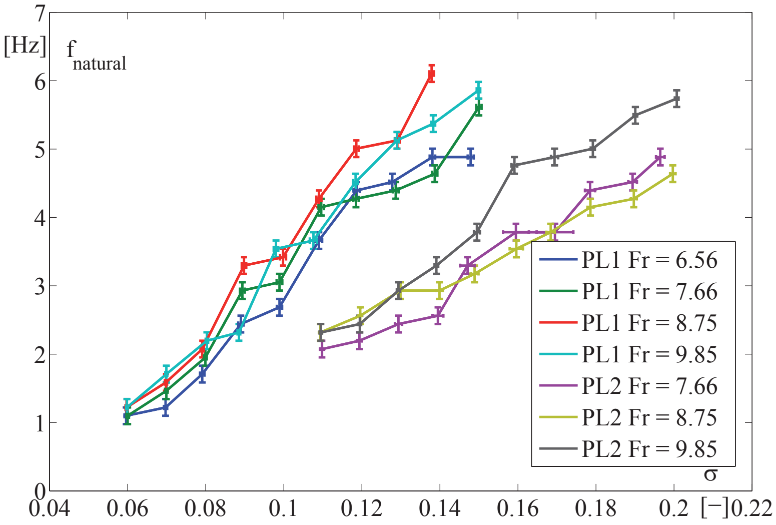

Figure 4.14: Evolution of natural frequency as a function of Thoma number for operating conditions *PL1* and *PL2*.

deep part load conditions. Two levels are nevertheless present: the first one near BEP and the second one between 45 and 55 % of the Q_{ED} at BEP. Because of this change in behavior from the vortex rope frequency, the study is conducted in two different operating ranges: the first operating condition *PL1* is located at 80% of the Q_{ED} at BEP, the second operating condition *PL2* is located at 64 % of the Q_{ED} at BEP. The analysis of these two operating conditions is realized in both cavitation-free and cavitating conditions for different Froude numbers.

Identification of eigenfrequencies is essential to the determination of hydroacoustic parameters of cavitation vortex rope. Thus, an excitation system is set up to define the natural frequency for every operating condition. The forced harmonic response of the hydraulic system is measured with 27 pressure sensors and a spectral analysis identifies the shape and the frequency of the first eigenfrequency. It is important to excite the first eigenmode of EPFL test rig PF3 with a frequency close to the first natural mode to avoid any interaction with the harmonics originating from the valve. It was demonstrated that the natural frequency increases relatively linearly as a function of Thoma number when the volume of cavitation decreases. Froude number influence remains small and the difference between the two operating conditions *PL1* and *PL2* is related to the pressure level in the draft tube.

These systematic measurements for different operating conditions will help in knowing the influence of the Q_{ED}, Thoma and Froude numbers on the hydroacoustic parameters of cavitation vortex rope. Thus, it will be possible to predict these hydroacoustic parameters for every operating condition of a reduced-scale physical model. Finally, according to the methodology presented in Chapter 3, it is necessary to develop a one-dimensional numerical model of the hydraulic circuit.

5 Test rig hydroacoustic model

In accordance with the methodology presented in Chapter 3, a modeling of the EPFL test rig PF3 is necessary to identify the hydroacoustic parameters of the draft tube model. The one-dimensional model of the hydraulic system is setup with the EPFL SIMSEN software. The most common hydraulic and electrical components are implemented in this software to simulate the transient behavior of a complete hydroelectric power plant. The modeling of the hydraulic components is based on equivalent electrical scheme representation which is widely described by Nicolet [41].

This chapter is focused on the modeling of the hydraulic components of EPFL test rig PF3 such as viscoelastic pipes, Francis turbine and spiral casing. Finally, a validation of the model is presented for a steady flow.

5.1 Viscoelastic pipe model without cavitation

The viscoelastic model is derived from momentum and continuity equations with a one-dimensional approach. As for the cavitation vortex rope modeling, the model assumes an isotropic fluid, a flow normal to the cross-section A and uniform distributions of pressure p and velocity C in the cross-section. Without a cavitation vortex rope, the set of equations 2.32 can be simplified:

- Without vortex rope, the pressure source S_h corresponding to the force induced by the helical vortex rope precession on the draft tube wall disappears.
- Cavitation-free flow induces a significantly higher wave speed, on the order of 1000 m/s. Thus, convective terms present in the momentum equation can be simplified.
- Test rig pipes do not have a divergent geometry and, therefore, the parameter R'_d can be removed.
- Without cavitation, dissipation induced by the compressibility of the cavitation volume

disappears and only wall deflection and compressibility of the liquid is taken into account.

Additionally, the dissipation induced by both the fluid and pipe material cannot be defined with quasi-steady state one-dimensional model, such as the Darcy–Weisbach friction equation. This model is known for underestimating friction forces and overestimating pressure oscillations during fast transient events [63]. Indeed, velocity profiles in unsteady-flow conditions show greater gradients, and thus greater shear stresses, than the corresponding values in steady-flow conditions [60]. To compensate for this lack of damping, the unsteady friction model J_u is introduced. The basic hyperbolic partial differential equations for one-dimensional unsteady pipe flow for an elementary pipe of length dx, and wave speed a_0 can be rewritten as:

$$\begin{cases} L'\frac{\partial Q}{\partial t} + R'_\lambda Q + \frac{\partial h}{\partial x} + J_u = 0 \\ \frac{\partial h}{\partial t} + \frac{a_0^2}{gA}\frac{\partial Q}{\partial x} = 0 \end{cases} \tag{5.1}$$

The RLC parameters of the equivalent scheme are given by:

$$R_\lambda = \frac{\lambda|\bar{Q}|dx}{2gDA^2} \qquad L = \frac{dx}{gA} \qquad C = \frac{gAdx}{a_0^2} \tag{5.2}$$

where λ is the local loss coefficient and D is the diameter of the elementary pipe. The hydraulic resistance R_λ, the hydraulic inductance L and the hydraulic capacitance C correspond to energy losses, inertia and storage effects, respectively.

From the normal viscous stresses τ_{xx} definition in cylindrical coordinates, the diffusion term J_u is derived:

$$J_{u,v} = \frac{\mu'}{\rho AD}\frac{\partial^2 Q}{\partial x^2} \tag{5.3}$$

This additional dissipation leads to a resistance in series with the capacitance. This viscoelastic resistance is accounting for both fluid and pipe material viscoelasticity and can be expressed as:

$$R_{ve} = \frac{\mu'}{\rho Agdx} \tag{5.4}$$

with μ' the equivalent viscoelastic damping of both the fluid and the wall. Currently, this viscoelastic parameter is difficult to quantify and comparison with experimental data is often essential to define its numerical value.

This new viscoelastic parameter has a direct impact on the damping, but it does not take into account the complete physics of the flow. Wave passage induces significant flow reversal near the wall. This flow reversal induces a large velocity gradient and thus a significant unsteady shear at pipe wall. It is widely recognized that the treatment of the wall friction as a static function of the mean velocity underestimates the wave attenuation at moderate and high frequencies. Inasmuch as the wall shear stress is not in phase with the mean velocity in pulsatile flow, the inertia term is modified by a factor ζ which is dependent on Reynolds number. A first approximation of the ζ parameter is given by Wylie and Streeter [63]. Another definition of this parameter is developed by Landry *et al.* [38] and is described as:

$$L_v = \frac{\zeta}{gA} \cong \frac{1+k}{gA} \tag{5.5}$$

where k is the Vítkovský friction coefficient [61]. This coefficient is defined using the Vardy analytically deduced shear decay coefficient C^* [59] defined as:

$$k = \sqrt{C^*}/2 \tag{5.6}$$

where

- for laminar flow: $C^* = 0.00476$
- for turbulent flow: $C^* = \frac{12.86}{Re^{log_{10}\left(15.29/Re^{0.0567}\right)}}$

Finally, the unsteady friction J_u may be represented by a viscoelastic resistance R_{ve} taking into account the fluid and pipe material viscoelasticity, and by an inertia term L_v induced by the phase difference between wall shear stress and mean velocity in pulsatile flow, see Figure 5.1. Experimentally, according to Covas *et al.* [16], it is very difficult to make the distinction between the frictional and viscoelastic behaviors. According to Duan *et al.* [23], the contribution of unsteady friction damping is important for small-scale (laboratories systems) but not for large-scale water supply and transmission lines. Clearly, the relaxation of the velocity gradient diminishes the role of unsteady shear. Indeed, the faster is the relaxation time, the less important is unsteady shear. Nevertheless, even when unsteady friction is not important for the wave envelope, it still imposes its signature on the wave shape.

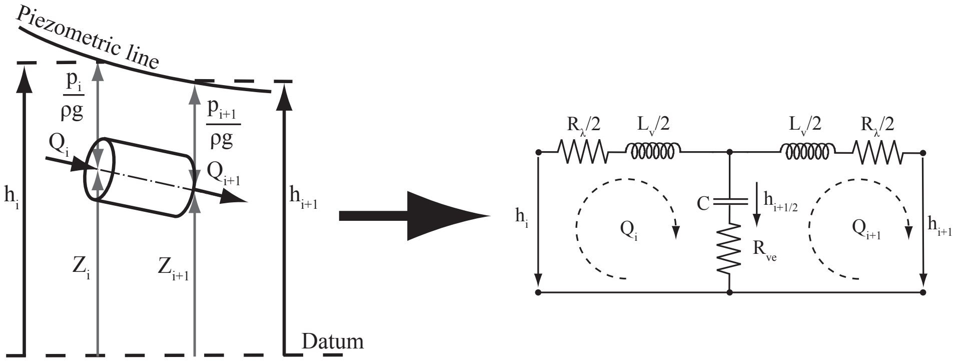
Piezometric line
$\frac{p_i}{\rho g}$
Q_i
h_i
$\frac{p_{i+1}}{\rho g}$
Q_{i+1}
h_{i+1}
Z_i
Z_{i+1}
Datum
$R_\lambda/2$
$L_v/2$
$L_v/2$
$R_\lambda/2$
h_i
Q_i
C
$h_{i+1/2}$
R_{ve}
Q_{i+1}
h_{i+1}

Figure 5.1: Viscoelastic pipe model without cavitation.

5.2 Francis turbine runner model

Francis turbines essentially behave as pressure sources converting hydraulic energy into mechanical work. A hydraulic inductance L_{turb} related to the inertia effects of the water and the hydraulic resistance R_{turb} modeling the head losses through the guide vanes closure complete the numerical model. This hydraulic resistance is only effective for small discharges, below 5 % of the nominal value. Pressure source H_{turb} and mechanical torque T_{turb} are driven by turbine characteristics which are nonlinear functions of guide vane opening y, rotational speed ω and discharge Q. The resulting equivalent model of the Francis turbine runner is described with an inductance, a resistance and a pressure source in series and is represented in Figure 5.2

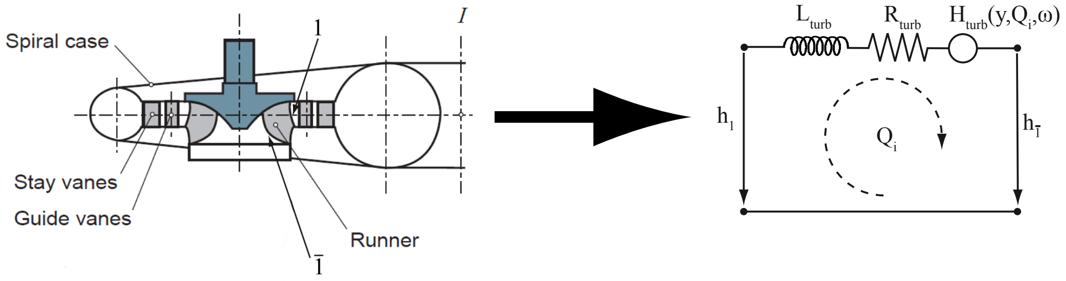
Spiral case
Stay vanes
Guide vanes
1
$\bar{1}$
Runner
L_{turb}
R_{turb}
$H_{turb}(y,Q_i,\omega)$
h_1
Q_i
$h_{\bar{1}}$

Figure 5.2: Francis turbine runner model.

The resulting differential equation is defined as:

$$L_{turb}\frac{dQ_i}{dt} + R_{turb}Q_i = -H_{turb} + h_1 - h_{\bar{1}} \tag{5.7}$$

where h_1 and $h_{\bar{1}}$ are piezometric heads at the runner inlet and runner outlet, respectively.

Finally, the rotational speed ω is obtained with the momentum equation applied to the rotational inertia J_{turb}:

$$J_{turb}\frac{d\omega}{dt} = T_{turb} - T_{elect} \tag{5.8}$$

T_{elect} represents the electromagnetic torque of the generator.

To improve the model of the Francis turbine, the dynamic behavior of the spiral casing is taken into account. Such an approach is suitable for transient purposes and has been successfully validated by Bolleter in the case of a pump [12].

5.3 Spiral casing model

The spiral casing consists in a composite material made of fiberglass in an Epoxy resin matrix. The hydroacoustic model of the spiral casing is composed of seven different viscoelastic pipes, represented in Figure 5.3. The star connection models the flow distribution on the runner.

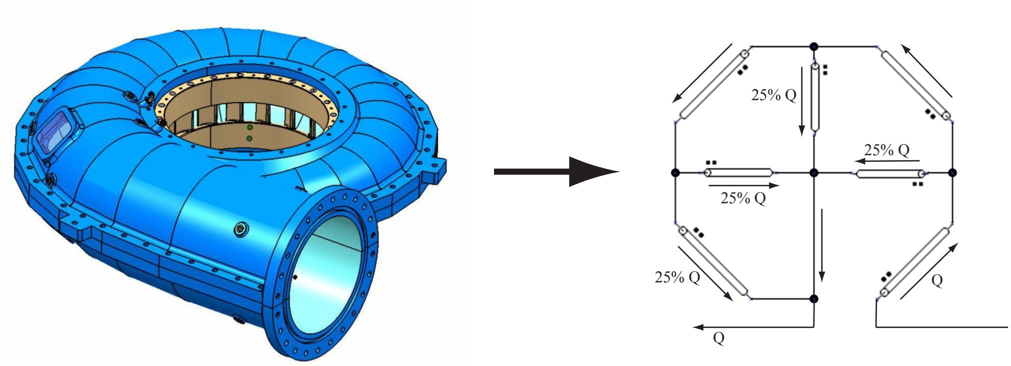

Figure 5.3: Spiral casing modeled by seven viscoelastic pipes.

For the determination of RLC terms of the hydroacoustic model of the viscoelastic pipes, the length L_{sc}, the cross-section A_{sc}, the friction coefficient λ_{sc} and the wave speed a_{sc} must be determined. The determination of the length and the cross-section is done using the structural characteristics of the reduced-scale physical model of the Francis turbine. Friction coefficient of pipes are evaluated with the Darcy-Weisbach equation. Wave speed is defined for a circular pipe as:

$$a^2 = \frac{1}{\rho\left(\frac{1}{E_w} + \frac{1}{A}\frac{dA}{dp}\right)} \simeq \frac{1}{\rho\left(\frac{1}{E_w} + \frac{2}{R_0}\frac{dR}{dp}\right)} \tag{5.9}$$

The E_w parameter represents the bulk modulus of water and $\frac{1}{A}\frac{dA}{dp}$ is the rated area increase due to pressure increase. The second term is experimentally determined for each pipe.

To identify wave speed in the spiral casing, internal pressure of the water is successively increased from 0 to 3 bars by increments of 0.5 bar. For each section shown in Figure 5.4(a), four indicators are installed to measure the deformation of the composite when internal pressure changes, see Figure 5.4(b). Then, internal pressure is decreased in order to verify the effect of hysteresis.

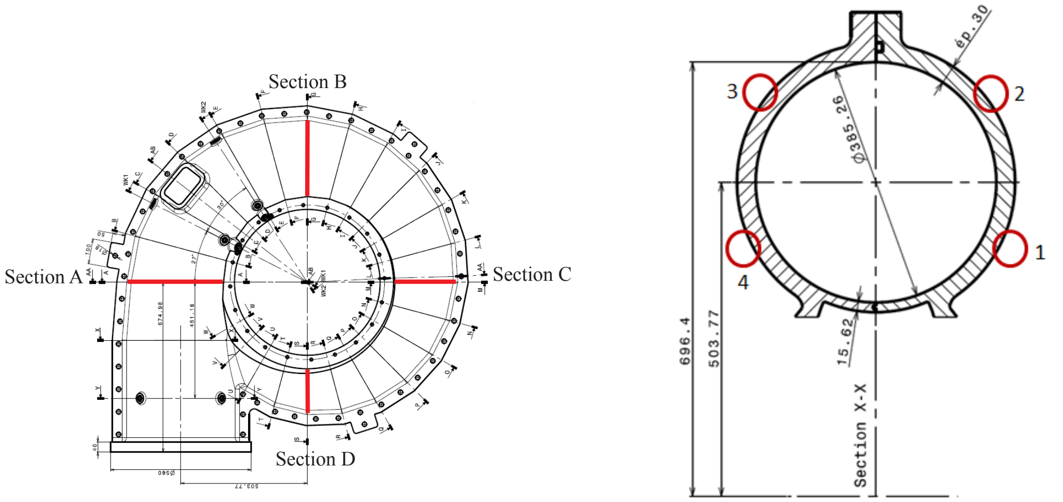

(a) Measurement section in the spiral casing.

(b) Indicator locations for a spiral casing section.

Figure 5.4: Measurement locations in the spiral casing.

For each section, the deformation of the spiral casing wall is carried out four times to check the repeatability of the experiment and to determine measurement error. The values obtained for every section are presented in Figure 5.5.

Finally, with Equation 5.9, the wave speed can be determined for different locations in the spiral casing. Generally, wave speed is increasing from inlet up to the tongue as the cross-section decreases. This result demonstrates a stiffening of the structure where cross-section decreases. Moreover, results indicate that the lower part of the spiral casing undergoes greater deformation than the upper part.

5.4 Energy losses model

Since the one-dimensional model does not take into account geometric variations of the circuit, every elbow is described as a singular specific energy loss and represented by a hydraulic resistance. The singular energy loss coefficient K_v is computed with the Weisbach formulation

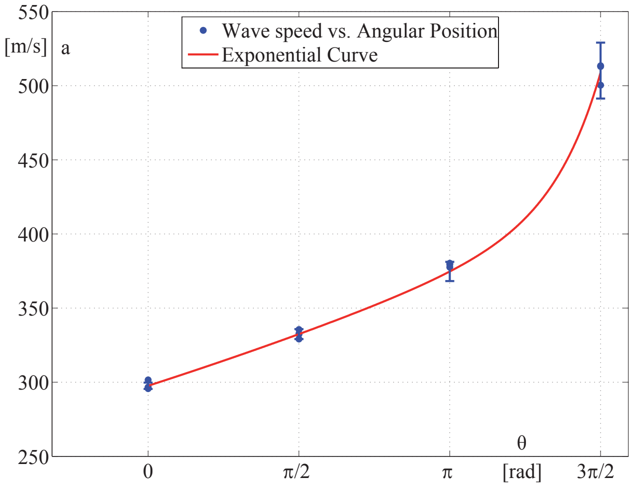

Figure 5.5: Wave speed evolution along the angular position of the spiral casing.

for an elbow [8]:

$$K_v = \left[0.131 + 1.847\left(\frac{D}{2r}\right)^{3.5}\right]\frac{\theta}{90} \tag{5.10}$$

where D is the internal diameter of the elbow, r corresponds to the radius of curvature, and θ defines the elbow angle in degrees.

5.5 Validation of the test rig hydroacoustic model for a steady flow

By using the numerical model of the hydraulic components, the EPFL test rig PF3 model is carried out, as illustrated in Figure 5.6. The numerical model is operated in a closed loop configuration, driven by two centrifugal pumps connected in series. The characteristic curves of the pumps and the reduced-scale physical model of the Francis turbine are experimentally measured and implemented in the numerical model. Moreover, every elbow in the test rig is modeled with a discrete loss and every hydraulic pipe is represented by a viscoelastic pipe. The star connection of the spiral casing model is introduced to model the flow distribution on the runner. Finally, the draft tube is divided into three parts: the cone, the elbow and the diffuser. Each component of the draft tube is modeled by a cavitation vortex rope modeling to take into account the complexity of the two-phase flow.

To validate the accuracy of the model, the numerical values of the torque T, the head H of the Francis turbine and the discharge Q are compared with experimental measurements for a steady flow.

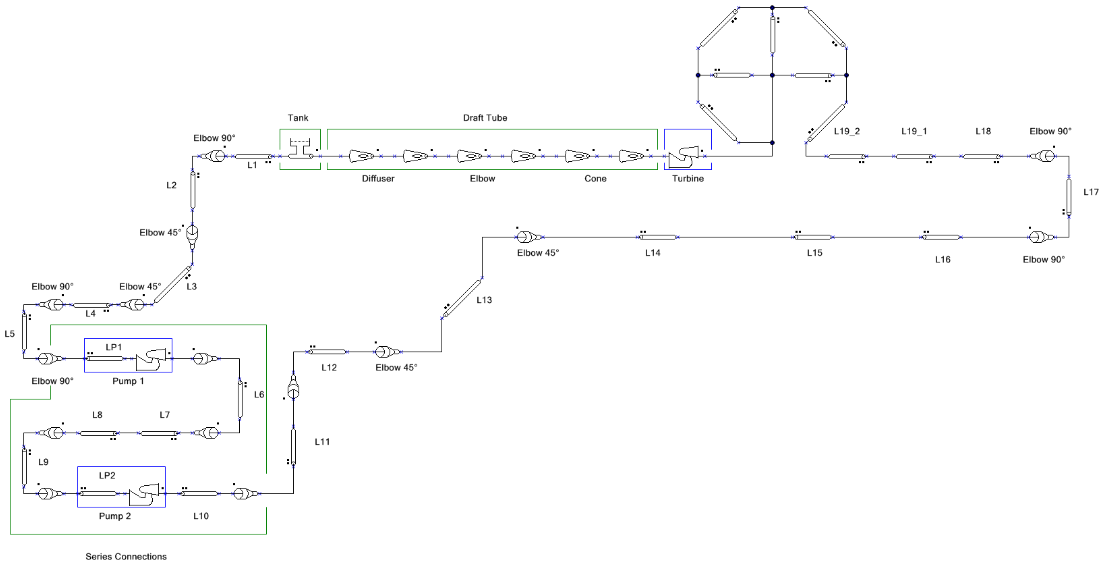
Tank
Draft Tube
Elbow 90°
L1
Diffuser
Elbow
Cone
Turbine
L19_2
L19_1
L18
Elbow 90°
L17
L2
Elbow 45°
Elbow 45°
L14
L15
L16
Elbow 90°
Elbow 90°
Elbow 45°
L3
L13
L4
L5
LP1
Elbow 90°
Pump 1
L12
Elbow 45°
L6
L8
L7
L11
L9
LP2
Pump 2
L10
Series Connections

Figure 5.6: Layout of EPFL test rig PF3 modeled with the SIMSEN software.

Experimentally, the torque is directly measured with a torque meter. The mean value of the discharge is measured using an eletromagnetic flow meter. Finally, the specific hydraulic energy $E = gH$ available to the turbine is given by subtracting the specific energies between the high pressure and low pressure sections of the hydraulic machine. Using a differential pressure measurement, Equation 1.3 can be simplified as:

$$E = \frac{\Delta p}{\rho_w} + \left(\frac{C_1^2}{2} - \frac{C_{\bar{1}}^2}{2}\right) = \frac{\Delta p}{\rho_w} + \frac{Q^2}{2}\left(\frac{1}{A_1^2} - \frac{1}{A_{\bar{1}}^2}\right) \tag{5.11}$$

where A_1 and $A_{\bar{1}}$ correspond to high pressure and low pressure cross-sections.

Experimental and numerical values are compared at operating point *PL2* without cavitation flow with a Froude number equal to 7.66. To stabilize the system to the desired operating condition, guide vane opening, rotational speed of the Francis turbine and hydraulic pumps are indicated. Results presented in Table 5.1 suggest a very good accuracy of the numerical model for a steady flow.

Table 5.1: Comparison of experimental and numerical results for a steady flow.

	Units	Experimental value	Numerical value	Relative error
H/H_{BEP}	[-]	0.7653	0.7768	+ 1.50 %
Q/Q_{BEP}	[-]	0.5608	0.5592	- 0.28 %
T/T_{BEP}	[-]	0.4550	0.4586	+ 0.79 %

5.6 Summary and discussion

A modeling of EPFL test rig PF3 is developed to identify the hydroacoustic parameters of the draft tube model. All hydraulic components of EPFL test rig PF3 are described and their numerical model are presented.

For a cavitation-free pipe, a viscoelastic model is derived from momentum and continuity equations. Unsteady friction induced by significant flow reversal near the wall may be represented by a viscoelastic resistance taking into account both fluid and pipe material viscoelasticity and by an inertia term induced by the phase difference between wall shear stress and mean velocity in pulsatile flow.

For the Francis turbine runner, an equivalent model is described with an inductance, a resistance and a pressure source in series.

The spiral casing consists in a composite material made of fiberglass in an Epoxy resin matrix. The hydroacoustic model of the spiral casing is composed of seven different viscoelastic pipes. The star connection models the flow distribution on the runner. For the determination of RLC terms of the hydroacoustic model of the viscoelastic pipes, the wave speed must be evaluated with Equation 5.9. Since the Young modulus is difficult to quantify for a composite material, experimental measurements of the deformation of the spiral casing wall are performed for different internal pressure. The results demonstrate an increase in the wave speed from inlet up to the tongue as the cross-section decreases.

Moreover, as the one-dimensional model does not take into account the geometric variations of the circuit, every elbow is described as a singular specific energy loss and represented by a hydraulic resistance.

The comparison between the numerical and experimental results suggests very good accuracy of the numerical model for a steady flow. Finally, this accurate numerical model being validated, it can be used to identify the hydroacoustic parameters of the cavitation vortex rope modeling.

6 Identification of the hydroacoustic parameters

The methodology described in Chapter 3 is applied to identify wave speed, bulk viscosity and pressure source for several operating conditions described in Table 4.2. The draft tube is modeled from the general momentum equation 2.10 to have a numerical simulation as close as possible to the physical flow. Values for hydroacoustic parameters will be validated in the frequency domain. Additionally, by knowing the wave speed for different Thoma numbers, the void fraction of the cavitation vortex rope will be computed. This parameter will be compared with the void fraction estimated with high-speed visualization of the cavitation vortex rope in the Plexiglas cone.

Four different numerical draft tube models will be compared to determine the impact of convective and divergent geometry terms of the momentum equation on the identification of the hydroacoustic parameters. Furthermore, to predict the hydroacoustic parameters for non-studied operating conditions and to break free from the dependence upon the level setting of the Francis turbine, dimensionless numbers will be proposed. They will have the advantage of being independent of the selected numerical model and define a behavior law of hydroacoustic parameters when the cavitation volume oscillates at resonance operating conditions.

Finally, to investigate the stability operation of the prototype, the hydroacoustic parameters need to be transposed to the prototype conditions according to similitude laws. By assuming both Thoma similitude and Froude similitude conditions, transposition laws will be developed and hydroacoustic parameters will be predicted for the prototype.

6.1 Identification of wave speed

Identification of eigenvalues is obtained with an excitation system and shown in Figure 4.14. With a numerical model and a dichotomy algorithm, the wave speed value is identified for two discharge factors Q_{ED} and presented in Figure 6.1 (Left) as a function of the Thoma number.

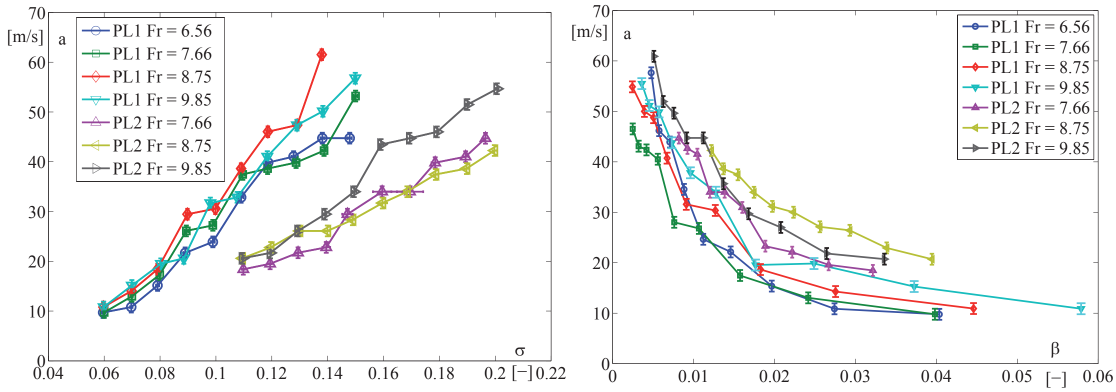

(a) For Thoma number

(b) For void fraction

Figure 6.1: Evolution of wave speed as a function of Thoma number (Left) or void fraction (Right) for different Froude numbers.

Thus, it can be observed that wave speeds drop to values in the range from 10 to 60 m/s when the cavitation vortex rope is present, while the wave speed value is around 400 m/s in cavitation-free conditions in a Plexiglas cone. Such low wave speeds imply that the convective part of the Navier-Stokes equation cannot be simplified anymore when the cavitation vortex rope occurs, and the assumption described by Equation 3.1 is only valid for the simplified model. Moreover, wave speed value increases almost linearly with Thoma number. To break free from this dependence upon the level setting of the Francis turbine, dimensionless numbers will be proposed afterward.

6.1.1 Computation of cavitation volume

By knowing the wave speed for different Thoma numbers, the volume of the cavitation vortex rope V_c, defined as the volume limited by the vapor pressure iso-surface, can be computed.

- First, according to Equation 3.11, the cavitation compliance can be computed and represented in Figure 6.2 (Left) as a function of the Thoma number.
- Then, the values of the cavitation compliance can be interpolated with a power law regression [35]. The quality of the selected mathematical law is reinforced with a regression coefficient R-square close to 1. This feature is applicable to all operating points, see Figure 6.2 (Right), and Equation 3.11 can be rewritten as:

$$C_c = \frac{gAdx}{a_{equ}^2} \approx -\frac{1}{H_{Turb}}\frac{\partial V_c}{\partial \sigma} = A\sigma^B \tag{6.1}$$

where A and B are the constants of power law regression.

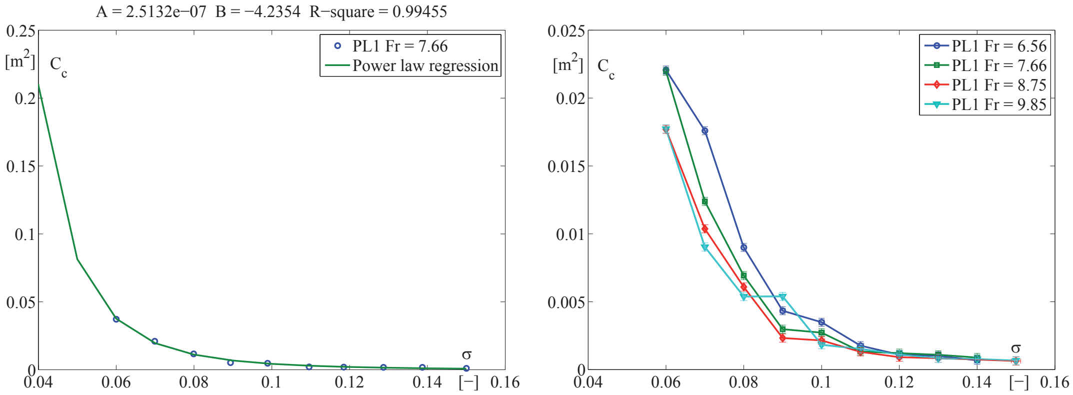

Figure 6.2: Evolution of cavitation compliance as a function of the Thoma number for different Froude numbers.

- Finally, by integrating Equation 6.1, a relation between cavitation volume and Thoma number can be defined as:

$$V_c = -H_{Turb}\frac{A}{B+1}\sigma^{B+1} \tag{6.2}$$

By performing integration of Equation 6.2 for all operating points, it becomes possible to express the wave speed as a function of void fraction β, defined as the fraction of the cone volume that is occupied by the gas phase, see Equation 3.13. Thus, with the help of the void fraction parameter β, the wave speed is determined independently of the Thoma number and, therefore, independently of the setting level of the turbine, see Figure 6.1 (Right). However, a dependence upon the pressure level in the draft tube is still observed and a dimensionless parameter should be introduced to remove this dependence.

6.1.2 Validation of void fraction

In this section, the mean void fraction analytically obtained is compared with the void fraction estimated with a high-speed visualization of the cavitation vortex rope in the Plexiglas cone. The experimental estimation of the vortex rope volume is based on the detection of the edges of the cavity. The accuracy of this analysis relies on proper lighting conditions and, therefore, accuracy depends on sharp contrast between the liquid and the gaseous phase of the flow. The device described in Figure 3.3 produces a good contrast and the vortex rope edge can be therefore simply determined by identifying the black and white pixels.

Thus, for each frame of the video, the image is converted into a black and white frame with an ideal threshold value according to Otsu [47] and Müller [39]. A region of interest in the Plexiglas cone is defined by the vertices of a polygon and is highlighted in Figure 6.3. This region is used to define a binary mask in the image and analyze the part of the flow where the vortex rope is located. Finally, to estimate the volume of the vortex rope $V_{c,local}$ in the region of interest, the local radius for each pixel row $R_x(z)$ is identified. It is assumed that for each pixel row, the local volume of the cavitation vortex rope is delimited by a surface revolution of the local radius around a symmetry axis. The volume in pixels is therefore the sum of the local surfaces in the region of interest.

$$V_{c,local} = \int_0^{2\pi}\int_0^{R_x}\int_{z_1}^{z_2} r \mathrm{d}\theta \mathrm{d}r \mathrm{d}z = 2\pi \int_{z_1}^{z_2} \frac{1}{2} R_x(z)^2 \mathrm{d}z \tag{6.3}$$

where the elevations z_1 and z_2 represent the upper and lower limits of the region of interest. This experimental estimation of the vortex volume has a weakness. The cavitation vortex rope continues well beyond the draft tube cone and only a fraction of the cavitation vortex rope is taken into account. Thus, this result cannot be directly compared with the cavitation volume calculated analytically. Therefore, the cavitation volume estimated with the high-speed visualization is divided by the volume of the region of interest to obtain a local experimental void fraction β_{local} and is compared with the mean void fraction β_{mean} computed analytically, see Figure 6.3. This procedure is applied to several vortex rope revolutions and for different operating conditions described in Table 6.1.

Table 6.1: Selected Francis turbine operating points for high-speed visualization analysis.

		$n_{ED}/n_{ED,BEP}$	$Q_{ED}/Q_{ED,BEP}$	Fr	σ
PL1	Part Load	1	0.80	8.75	[0.06 - 0.10]
PL2	Part Load	1	0.64	8.75	[0.11 - 0.17]

The error on experimental measurements is due to variation of cavitation volume during vortex rope precession. The magnitude of the error is higher for a Thoma number equal to 0.17 because this operating condition corresponds to the hydroacoustic resonance of the hydraulic test rig. Thus, the precession frequency matches the natural frequency of the hydraulic system, induced by the cavitation volume. In this operating condition, all pressure sensors in the cone are in phase, see Figure 6.4, and synchronous pressure pulsations are transmitted to the entire hydraulic test rig, inducing pulsations of the cavitation volume at the natural frequency.

The error in the measurement of the cavitation volume is also higher for a Thoma number equal to 0.11. This results from impacts on the draft tube wall of the vortex rope during its precession [43]. This shock generates a pressure wave propagating in the draft tube and therefore influencing the pressure field and the cavitation volume in the cone.

Generally, the local experimental void fraction is relatively similar to the mean values calculated analytically. However, for Thoma numbers outside the range 0.12 to 0.16, the experimental method shows a local void fraction greater than the mean value calculated analytically.

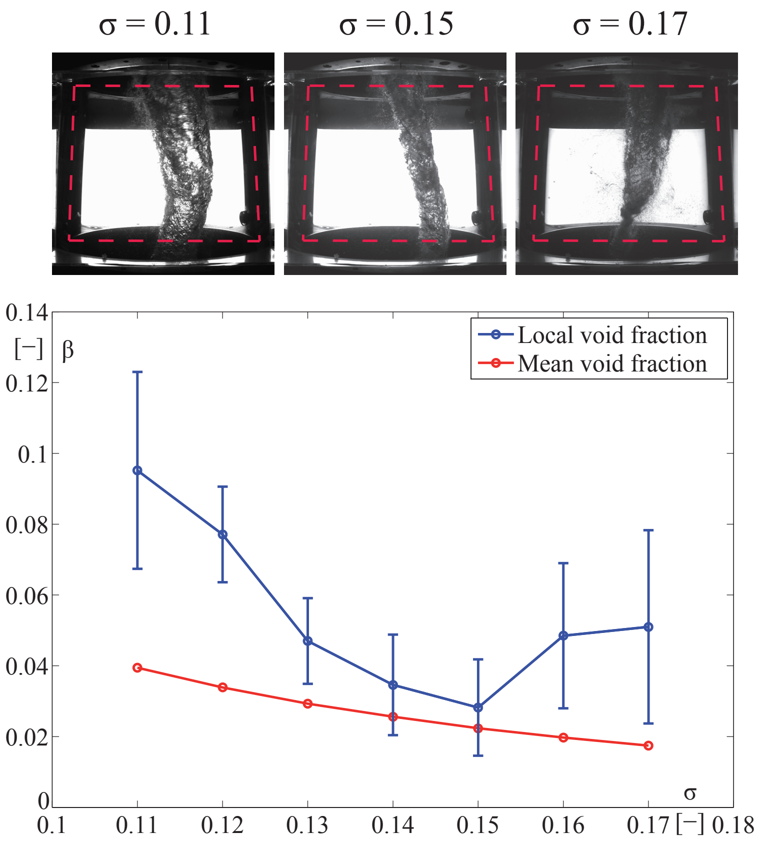

Figure 6.3: Comparison between mean void fraction computed analytically and local void fraction determined with a high-speed visualization.

This difference comes from the local aspect of the measurement. Indeed, with the high speed visualizations, only the part of the cavitation vortex rope visible in the Plexiglas cone is captured. However, observing the evolution of the cross-section of the vortex rope along the cone in Figure 6.3, there is a progressive reduction of its radius. Thus, the mean void fraction in the cone is greater than the mean void fraction along the whole draft tube.

Finally, the analytical method shows a good value of mean void fraction and cavitation volume. In comparison, the experimental method indicates only a local value of the void fraction, which may be slightly greater than the mean value in the draft tube.

6.1.3 Development of a dimensionless parameter for wave speed

A dependence upon the pressure level in the draft tube is still observed in Figure 6.1 (Right). To overcome this characteristic, a dimensionless number is developed. By using the definition of wave speed in a circular pipe without cavitation, see Equation 2.19, and applying the Buckingham-Π theorem, the dimensionless number Π is defined as follows, where the pressure

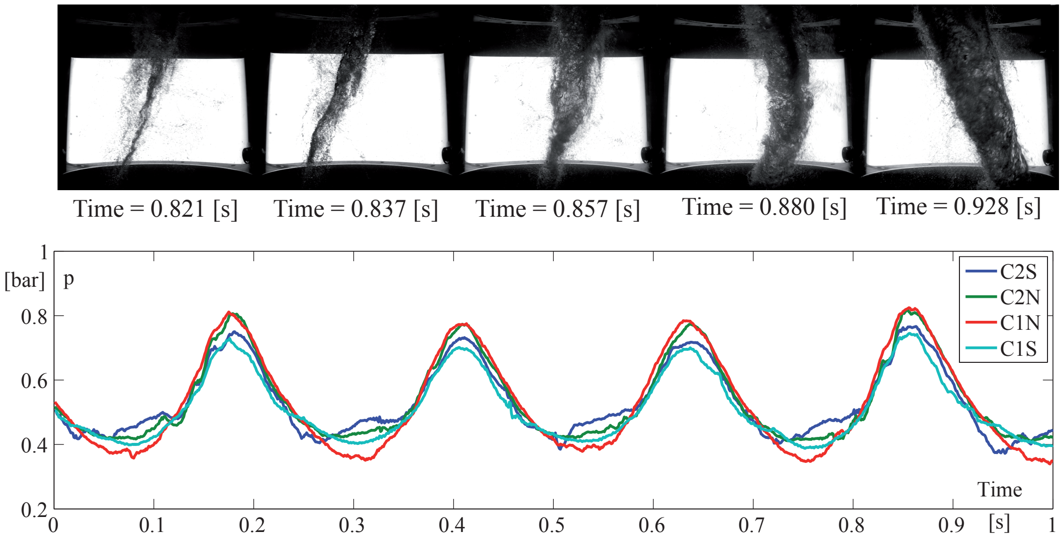

Figure 6.4: Evolution of pressure and vortex rope volume for $Q_{ED} = 0.128$ and Fr = 8.75 at the resonance operating condition.

p_{Outlet} is the mean pressure at the turbine outlet and p_v represents the saturated vapor pressure:

$$\Pi = \frac{\rho_w a^2}{p_{Outlet} - p_v} \tag{6.4}$$

This dimensionless term divides the squared wave speed by pressure energy. A similar dimensionless term C_c' was developed by Dörfler in 1982 [18] [19]. This dimensionless cavitation compliance C_c' is obtained from a reference volume D_{ref}^3 and the velocity head $H_{D,v}$ used as reference pressure, and it is defined as:

$$C_c' = C_c \frac{H_{D,v}}{D_{ref}^3} \qquad \text{where} \qquad H_{D,v} = \frac{1}{2g}\left(\frac{4Q}{\pi D_{ref}^2}\right)^2 \tag{6.5}$$

Using the definition of hydraulic capacitance, see Equation 2.30, the dimensionless cavitation compliance can be rewritten as:

$$C_c' = \frac{Adx}{a^2 D_{ref}^3}\frac{C^2}{2} \tag{6.6}$$

This equation can be simplified by removing the terms with the same dimension.

$$C'_c = \frac{Adx}{D_{ref}^3}\frac{C^2}{2a^2} \approx \frac{C^2}{2a^2} \tag{6.7}$$

Thus, the dimensionless cavitation compliance developed by Dörfler defines a ratio between the squared wave speed and the kinetic energy so that the dimensionless parameter Π defines a ratio between the squared wave speed and the pressure energy.

By using the dimensionless parameter Π, each experimental data set can be approximated by a power function, see Figure 6.5.

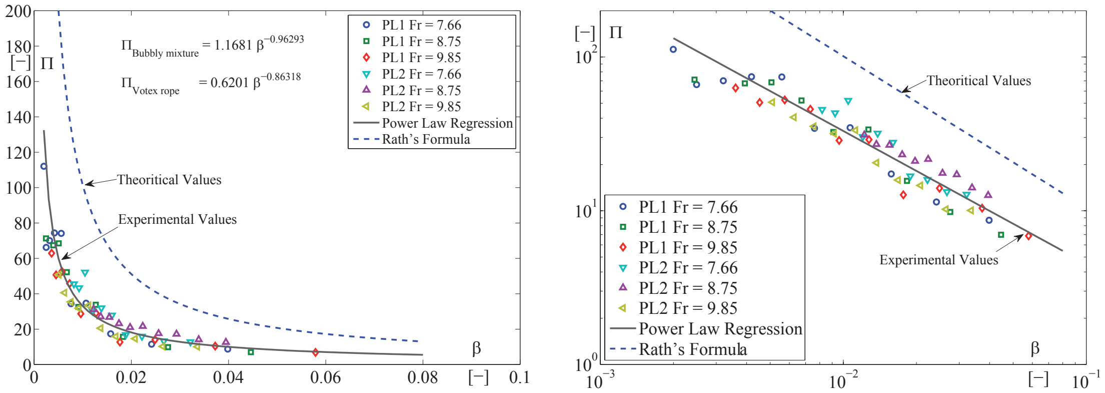

(a) with linear axis

(b) with logarithmic axis

Figure 6.5: Draft tube evolution of dimensionless wave speed as a function of void fraction β.

This trend is validated by comparing the results with a theoretical model developed by Rath in 1981 [50] including the compressibility of gas and liquid, the elasticity of the pipe wall and the surface tension in bubbly air-water mixture. This theoretical model described by Equation 6.8 gives accurate results for wave speeds in a homogenous bubbly flow. ρ_c describes water vapor density, E_w represents the bulk modulus of the liquid phase, E_p is the Young modulus of the pipe wall, D describes the pipe diameter and finally e represents the thickness of the pipe wall.

$$a = \left[\left(\beta\rho_c\frac{p}{p_0} + (1-\beta)\,\rho_w\left(1 + \frac{(p-p_0)}{E_w}\right)\right)\left(\frac{\beta}{p} + \frac{1-\beta}{E_w} + \frac{D}{eE_p}\right)\right]^{-\frac{1}{2}} \tag{6.8}$$

Generally, the cavitation vortex rope does not satisfy bubbly flow assumption and imposes lower wave speeds compared to the value of the theoretical model. The ratio between theoretical values and wave speed inferred from experimental data is a constant C_{Adapt} equal to

1.761, see Figure 6.6. Thus, it is possible to use Rath's equation by dividing the wave speed value by the constant C_{Adapt}. However, the geometry of the machine could play a role and this constant could be different for another hydraulic machine. Therefore, the methodology presented in this thesis should be applied to other turbines to verify the impact of the turbine and draft tube geometry on wave speed.

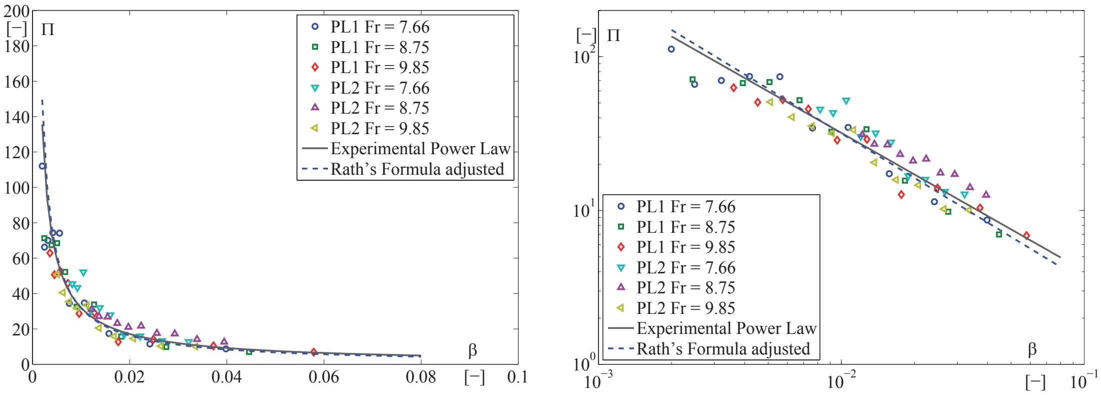

(a) With linear axis

(b) with logarithmic axis

Figure 6.6: Evolution of the dimensionless wave speed in the draft tube as a function of void fraction β.

Moreover, it is also important to note that this power function reaches an upper limit when the void fraction tends to zero. When cavitation disappears, Rath's equation becomes similar to the conventional formula for circular pipes and imposes a finite value on wave speed. Finally, the development of a new law relating the void fraction to the dimensionless parameter Π allows for the determination of wave speed in the draft tube with respect to the cavitation volume and the pressure at turbine outlet. This law derived from Rath's formula can be used in numerical models and allows for simulation of non-linear phenomena such as pulsation of cavitation volume at resonance.

6.2 Identification of bulk viscosity

Identification of bulk viscosity is obtained with an excitation system and a Pressure-Time method. For each operating condition out of resonance, excitation energy is experimentally quantified and is injected in the numerical model. Then, the dissipation term μ'' is adjusted with the dichotomy algorithm to obtain a numerical forced harmonic response equal to the experimental forced harmonic response, see Figure 6.7.

This comparison is focused on circular pipes connecting the upstream reservoir to the Francis turbine to diminish the uncertainty related to experimental measurements. In this case, on the one hand, without draft tube, and therefore without vortex rope, it is not necessary to separate the synchronous from the convective part in experimental measurements. On the other hand,

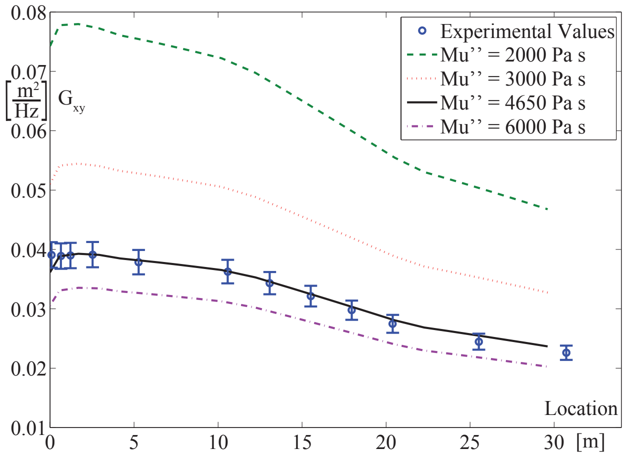

Figure 6.7: Comparison of experimental and numerical responses to an excitation source for different second viscosities at operating point *PL1*, Fr = 6.56 and $\sigma = 0.08$.

without Francis turbine, the pressure gradient associated to the hydraulic machine is not taken into account. Finally, this methodology is applied to different Froude and Thoma numbers described in Table 4.2.

6.2.1 Influence of the degassing procedure on harmonic response

The shape of the forced harmonic response essentially depends on wave speed a_{PF} in the hydraulic pipes. This wave speed is related to the amount of gas dissolved in the water and therefore depends on the quality of the degassing procedure. By knowing the rate of gas dissolved in water, the wave speed is calculated using Rath's equation 6.8. The influence of the gas dissolved in the water is presented in Figure 6.8 as an example for the operating condition *PL2* with Froude and Thoma numbers equal to 7.66 and 0.13, respectively. In this figure, the forced harmonic response is made dimensionless in order to compare the influence of the degassing procedure on the shape of the harmonic response.

Thus, for four different amount values of gas dissolved in the water, the wave speeds in the upstream pipes are computed and the shape of the numerical harmonic response is modified. Moreover, if the gas concentration is unknown, it can be deduced by comparing the numerical dimensionless harmonic response with the experimental data. For low void fraction, the evolution of the wave speed with Rath's equation is strictly decreasing and a dichotomy algorithm can be used.

6.2.2 Development of a dimensionless parameter for bulk viscosity

To compare bulk viscosity values for different Froude numbers, a dimensionless bulk viscosity has to be defined with the Buckingham-Π theorem. In the literature, a bulk viscosity param-

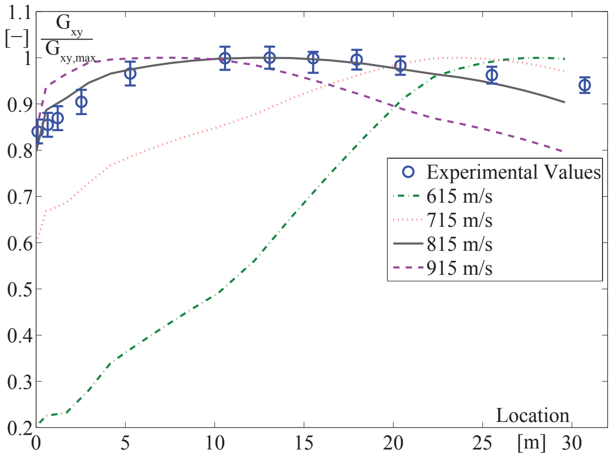

Figure 6.8: Comparison of forced harmonic response for different wave speeds a_{PF} on the test rig at the operating point *PL2*, Fr = 7.66 and σ = 0.13.

eter was developed by Pezzinga [48] in 2003. He validated his model showing that pressure dependent on wave speed and bulk viscosity allows to reproduce results of experimental measurements of water hammer transients with cavitation. The analytical formulation, described by Equation 6.9, has been derived by considering homogeneous bubbly flow.

$$\mu'' = \theta \frac{\left((1-\beta)\rho_w + \beta\rho_c\right)^2 \beta\rho_c R T a^4}{p^2} \tag{6.9}$$

In this equation, θ represents a relaxation time, R is the ideal gas constant and T is the temperature in Kelvin. The relation can be simplified for low void fraction as:

$$\mu'' \approx \theta \frac{(1-\beta)^2 \beta\rho_c\rho_w^2 R T a^4}{p^2} \tag{6.10}$$

By applying the Buckingham-Π theorem to the previous equation, a dimensionless parameter is defined, where the pressure p_{Outlet} is the mean pressure at the outlet of the turbine and p_v represents the saturated vapor pressure:

$$M'' = \frac{\mu'' f_{natural}}{p_{Outlet} - p_v} \tag{6.11}$$

The dimensionless bulk viscosity values computed for different Froude and Thoma numbers are represented in Figure 6.9 as a function of the Thoma number. Thus, it can be observed that all experimental data for a given discharge factor Q_{ED} can be approximated by a power function and that the quality of the selected mathematical law is good with a regression coefficient R-square equal to 0.889.

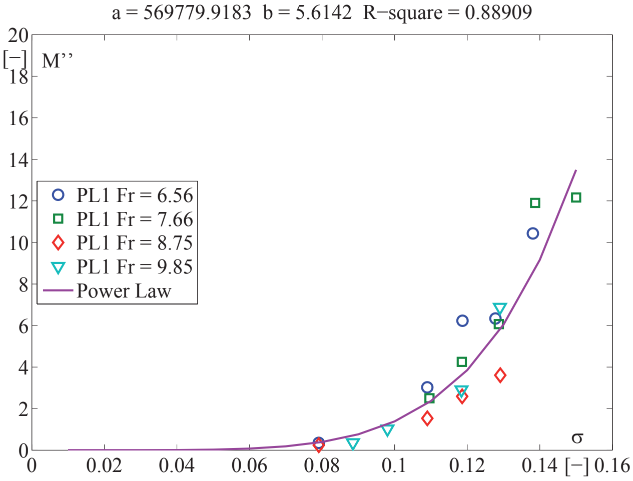

Figure 6.9: Evolution of dimensionless bulk viscosity as a function of Thoma number.

Moreover, the dimensionless bulk viscosity can be represented in Figure 6.10 as a function of the void fraction. The numerical results also follow a power law regression and it becomes possible to extrapolate dissipation values for any operating condition. However, the geometry of the machine could play a role and the constants of power law regression could be different for another hydraulic machine. It would therefore be interesting to develop an analytical formulation to connect the dimensionless bulk viscosity to the void fraction.

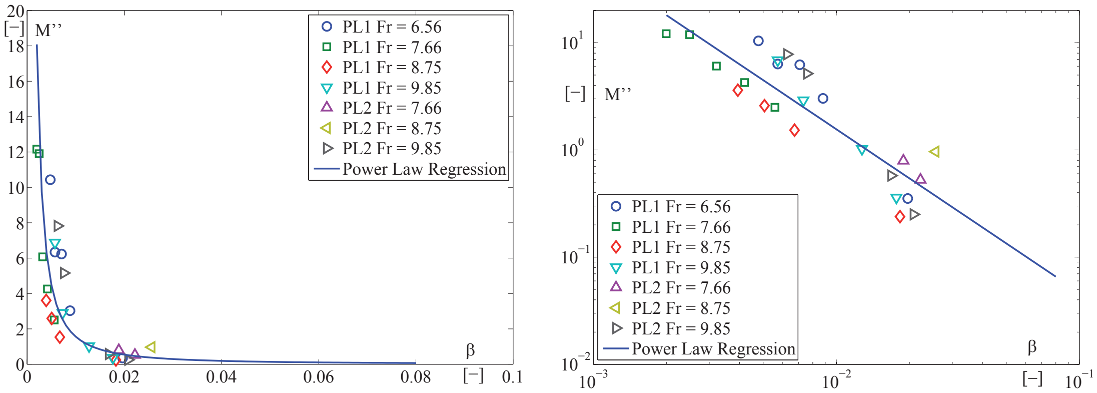

(a) With linear axis

(b) with logarithmic axis

Figure 6.10: Evolution of dimensionless bulk viscosity as a function of the void fraction.

Using the Buckingham-Π theorem, an analytic equation is developed to define the dimensionless bulk viscosity where $p = p_{Outlet} - p_v$.

$$M'' = \Pi^2 (1-\beta)^2 \frac{\rho_c}{\rho_w} = \left(\frac{\rho_w a^2}{p}\right)^2 (1-\beta)^2 \frac{\rho_c}{\rho_w} \tag{6.12}$$

This equation can be compared with the dimensionless form of Pezzinga's equation. Thus, Equation 6.9 can be rewritten as:

$$M'' \approx \frac{\mu''}{\theta p} = \left(\frac{\rho_w a^2}{p}\right)^2 (1-\beta)^2 \frac{\beta \rho_c R T}{p} \tag{6.13}$$

First, it can be seen in Figure 6.11 that the new equation 6.12 is in perfect agreement with the power law regression and it does not depend on specific constants related to the hydraulic machine. Moreover, Equation 6.12 is directly related to the dimensionless number Π as Pezzinga's dimensionless formula suggested. Thus, this new equation depends on the wave speed raised to the power of four and indicates that it is very important to accurately determine the wave speed in the draft tube. Finally, it is important to note that Equation 6.12 does not tend to zero when the void fraction tends to zero, but to a lower dissipation value. Pezzinga's law should therefore be preferred when the cavitation vortex rope disappears almost completely.

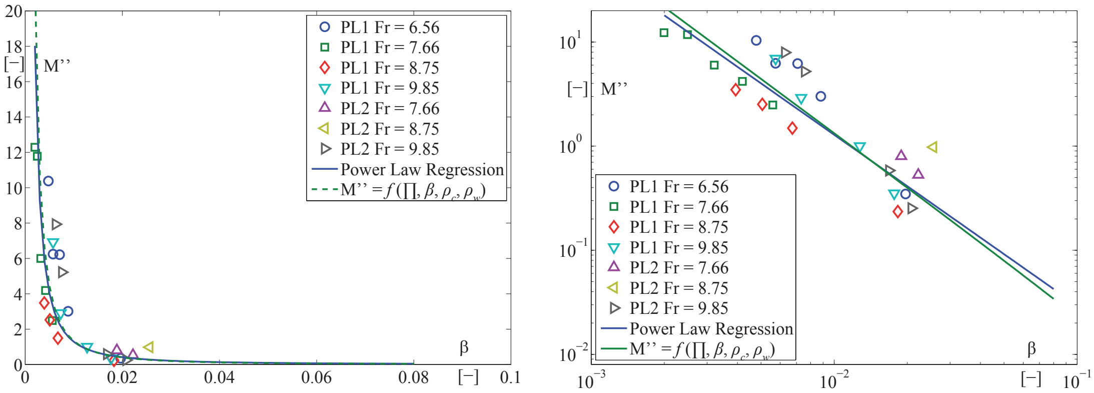

(a) With linear axis

(b) with logarithmic axis

Figure 6.11: Evolution of dimensionless bulk viscosity as a function of the void fraction.

Validation of wave speed and bulk viscosity is shown in Figures 6.12 and 6.13 for several operating conditions. Generally, the forced harmonic response of the experimental system to an external excitation is well reproduced by the numerical model in the frequency domain, independently of the discharge factor, the Froude numbers and the Thoma numbers. The

Francis turbine location is located at L = 0 m. The experimental values having a positive location represent the 12 pressure sensors (P1-P12) distributed along EPFL test rig PF3. The experimental values having a negative location represent the pressure sensors installed in the cone, the elbow and the diffuser of the draft tube.

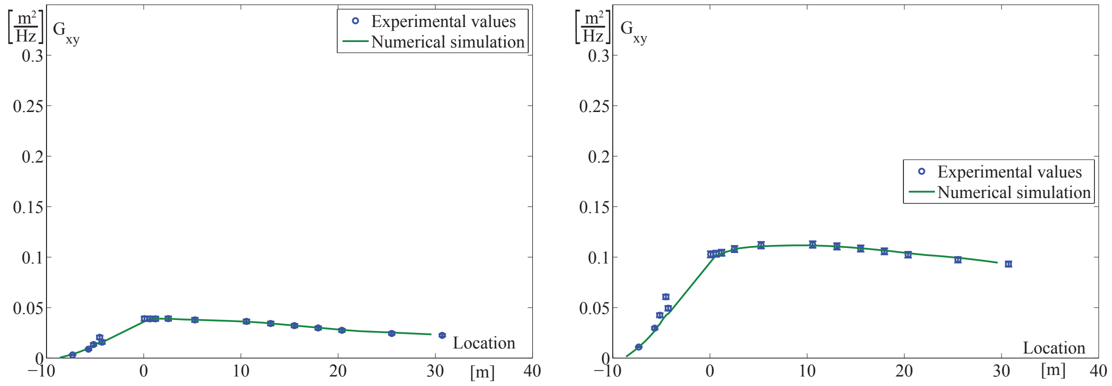

(a) Fr = 6.56, σ = 0.08, natural frequency = 1.709 Hz (b) Fr = 6.56, σ = 0.11, natural frequency = 3.662 Hz

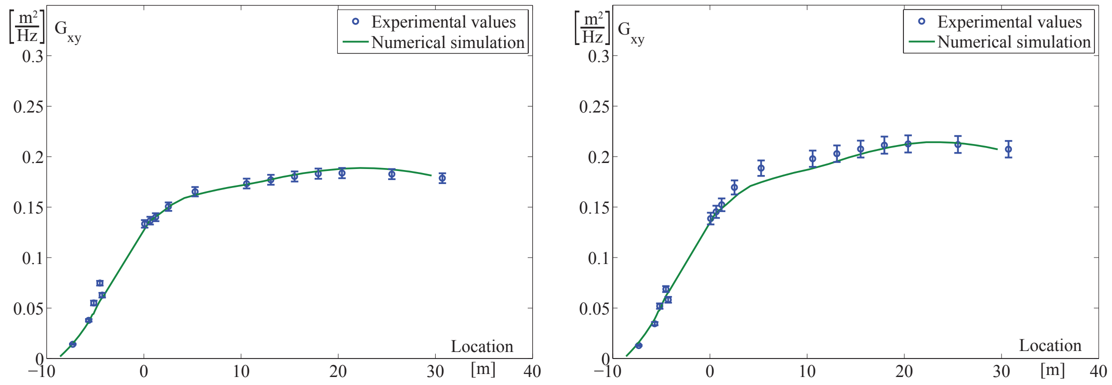

(c) Fr = 6.56, σ = 0.12, natural frequency = 4.394 Hz (d) Fr = 6.56, σ = 0.13, natural frequency = 4.517 Hz

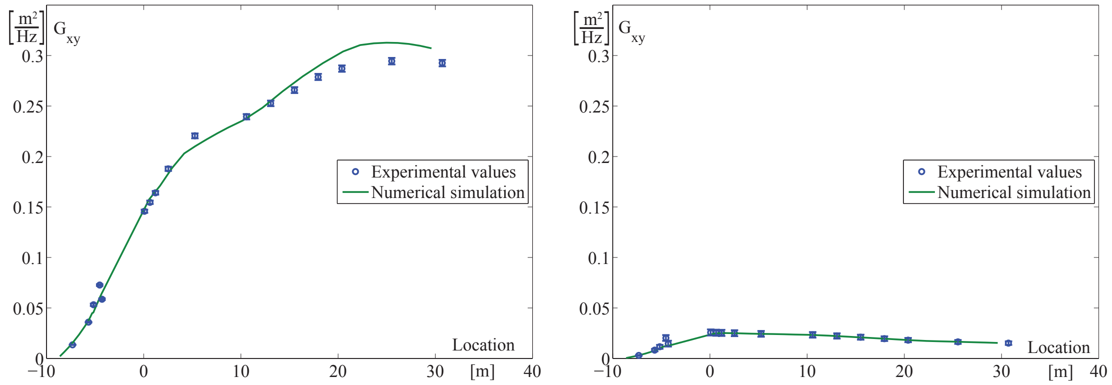

(e) Fr = 6.56, σ = 0.14, natural frequency = 4.883 Hz (f) Fr = 8.75, σ = 0.08, natural frequency = 2.075 Hz

Figure 6.12: Comparison between experimental and numerical forced harmonic responses for the operating condition *PL1* at natural frequency

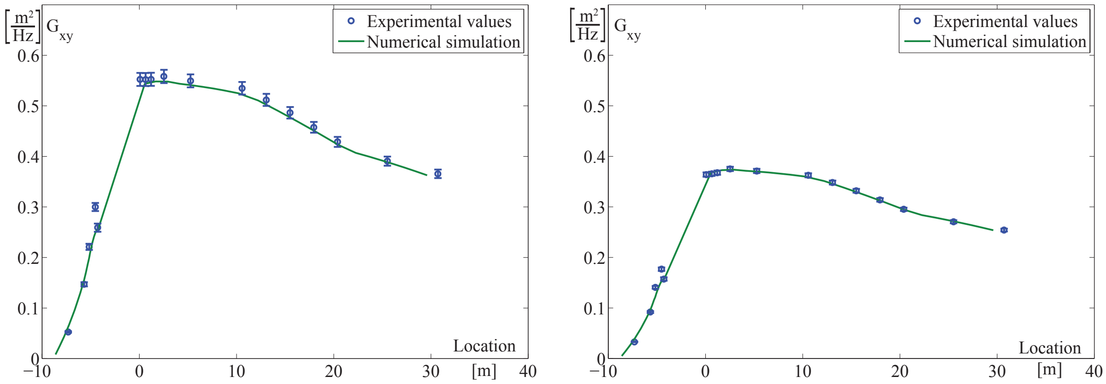

(a) Fr= 7.66, σ = 0.13, natural frequency = 2.441 Hz

(b) Fr= 7.66, σ = 0.14, natural frequency = 2.564 Hz

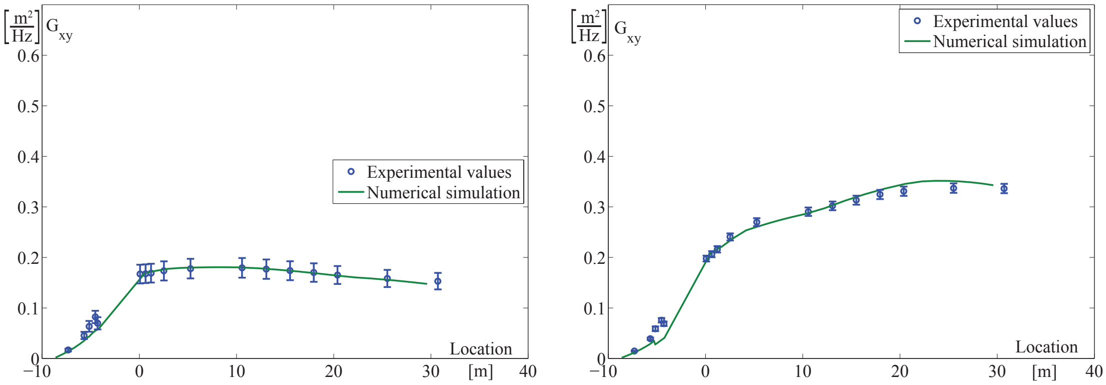

(c) Fr= 7.66, σ = 0.15, natural frequency = 3.296 Hz

(d) Fr= 7.66, σ = 0.18, natural frequency = 4.395 Hz

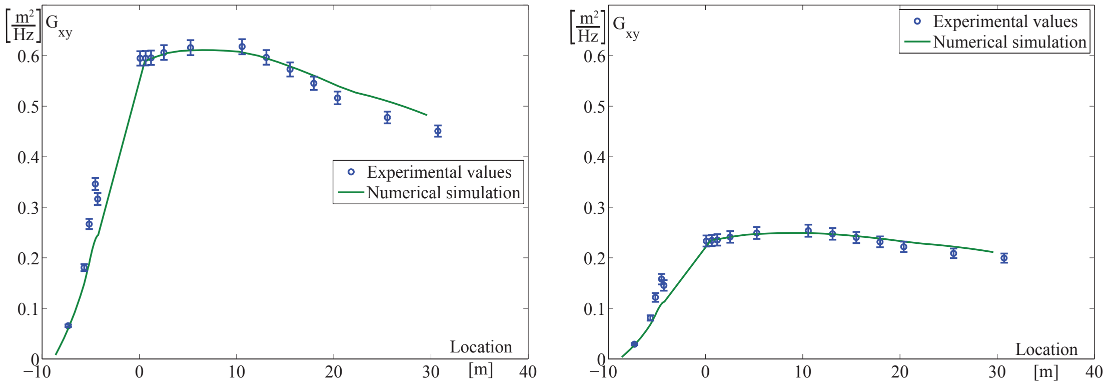

(e) Fr= 8.75, σ = 0.14, natural frequency = 2.930 Hz

(f) Fr= 9.85, σ = 0.14, natural frequency = 3.174 Hz

Figure 6.13: Comparison between experimental and numerical forced harmonic responses for the operating condition *PL2* at the natural frequency

6.3 Identification of pressure source

Identification of the pressure source is based on the excitation generated by the precession of the vortex rope and therefore the use of an external excitation source is not required. The pressure source S_h is modeled by a Gaussian curve characterized by three mathematical parameters: L representing the location of the center of the pressure source, e corresponding to the standard deviation of the Gaussian curve and A defining the amplitude of the Gaussian curve.

These three mathematical parameters are determined with a genetic algorithm minimizing the following four criteria:

- The first objective compares the experimental forced response with the response of the numerical model with a particular focus on circular pipes connecting the upstream reservoir to the Francis turbine.
- The second objective uses four pressure sensors in the first measurement section in the cone. Thus, it is possible to separate the synchronous part from the convective part and compare the synchronous value with the numerical model.
- The third objective is similar to the previous one, but by using the second measurement section in the cone.
- The last objective uses pressure sensors located in the elbow and the diffuser of the draft tube. In the absence of circular sections, the uncertainty of these pressure measurements is high and the weight of this objective is reduced.

This algorithm is applied for different discharge factors Q_{ED} and for various Thoma and Froude numbers to study their impact. However, in order to decrease the number of solutions satisfying the four objectives, it is assumed that the shape of the pressure source is independent of Thoma number. Therefore, the location of the pressure source L and the standard deviation e will be evaluated by minimizing the global error $Error_{global}$ on all Thoma numbers, for constant discharge factor and Froude number, see Equation 6.14.

$$Error_{global} = \frac{1}{Nb} \sum_{\sigma} Error \tag{6.14}$$

where Nb defines the number of studied Thoma numbers at constant discharge factor and constant Froude number. To define the search space and to ensure the convergence of the algorithm to a global minimum, a 3D representation of solutions is performed in Figure 6.14. Thus, for every location L between 0.01 and 0.95 m and for every standard deviation between 0.01 and 0.5 m, the optimal amplitude is computed so as to minimize the global error defined by the previous objectives. The Z-axis represents the minimum global error that exists between the experimental and the numerical values, for all Thoma numbers according to Equation 6.14. Finally, Figure 6.14 confirms the existence of many local minima for different operating conditions and therefore the use of a genetic algorithm. To ensure proper identification of the global minimum, a sensitivity analysis is performed to reduce the search space.

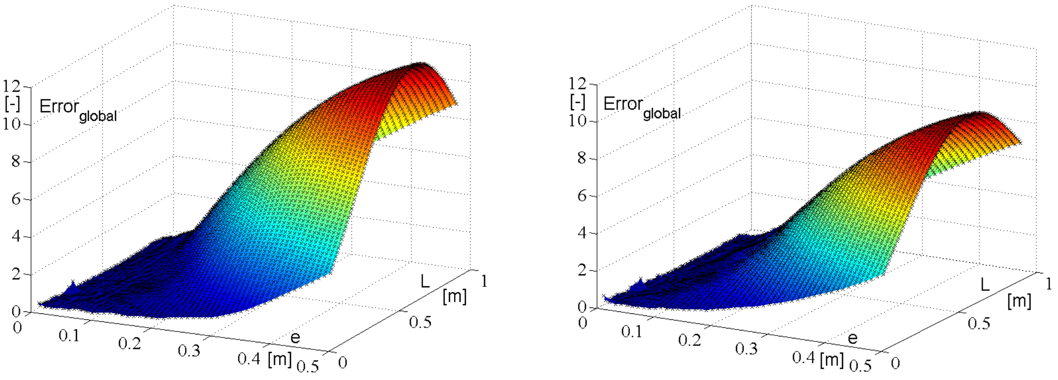

(a) *PL1* Fr = 6.56

(b) *PL1* Fr = 7.66

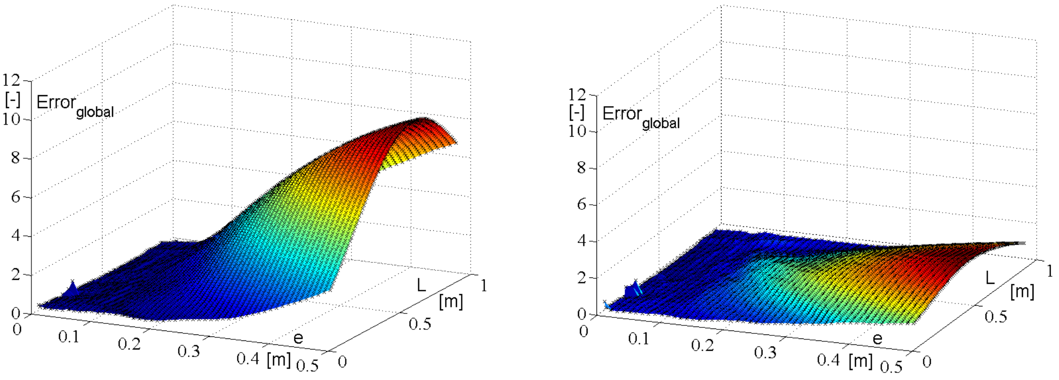

(c) *PL1* Fr = 8.75

(d) *PL1* Fr = 9.85

Figure 6.14: Global error as a function of pressure source location L and standard deviation e.

6.3.1 Study of standard deviation *e* of pressure source

According to Figure 6.14, the standard deviation e should be low to minimize the global error, independently of Froude number. However, a low standard deviation would generate a concentrated pressure source S_h, and a dependence of the pressure source to its relative location. Indeed, according to Figure 6.15, for standard deviations equal to 0.01 and 0.02 m, the optimal amplitude minimizing the global error is very dependent on the location of the pressure source in the numerical model. For instance, when the pressure source is located on a numerical pressure node described by a red circle, the optimal amplitude is minimum. Thus, for this case study, it is appropriate to select higher standard deviations than 0.2 m. Generally, the standard deviation e must be higher than the elementary pipe length dx.

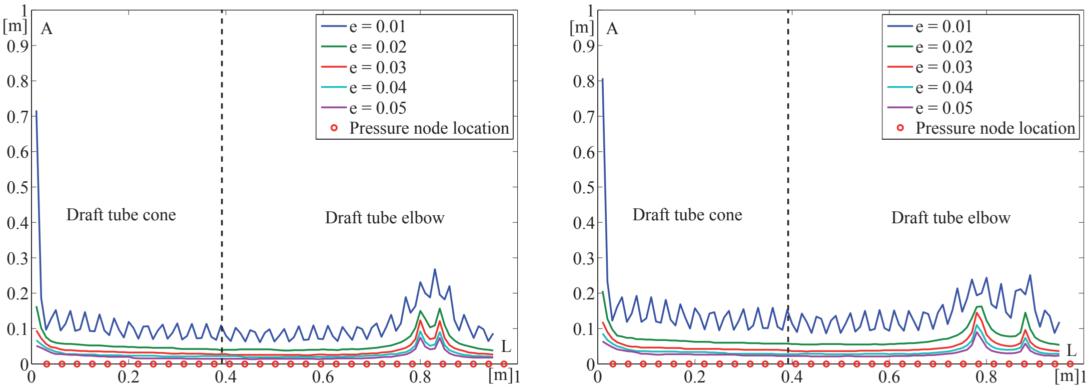

(a) *PL1* Fr = 6.56 (b) *PL1* Fr = 7.66

Figure 6.15: Amplitude of the pressure source as a function of pressure source location L.

Moreover, according to Figure 6.16, for a pressure source located in the elbow (L>0.4), a minimum standard deviation significantly reduces the global error. In contrast, for a pressure source located in the cone (L<0.4), the value of the standard deviation has no influence on the global error. Finally, to minimize global error and ensure convergence of the genetic algorithm to an optimal solution, the standard deviation should be as low as possible, without introducing a dependency on the discretization.

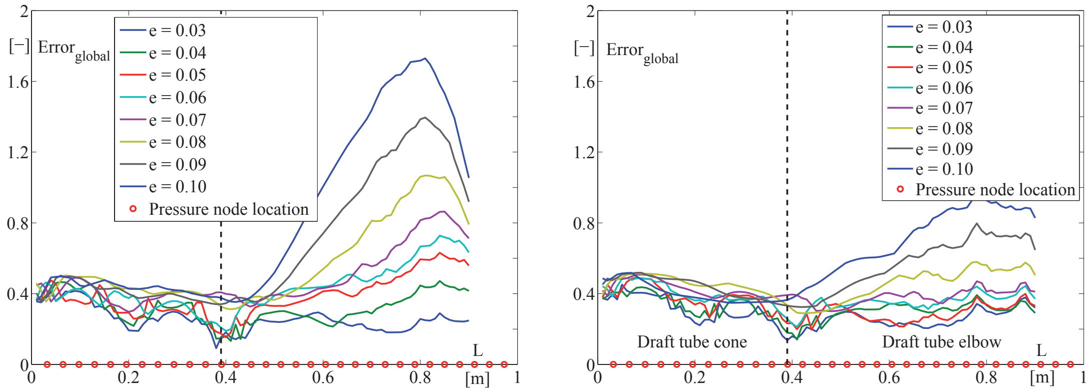

(a) *PL1* Fr = 6.56 (b) *PL1* Fr = 7.66

Figure 6.16: Error for all Thoma numbers as a function of pressure source location L.

6.3.2 Study of pressure source location *L*

Comparing evolution of global error as a function of the pressure source location L in Figure 6.17 for a standard deviation $e = 0.03$ m, the influence of the Froude number is relatively small. Indeed, for a constant discharge factor Q_{ED}, the global error is minimal for a location L = 0.38 m for the operating condition *PL1* and for a location L = 0.43 m for the operating condition *PL2*, independently of the Froude number. Thus, for this case study, the pressure source should be at the entrance of the elbow to minimize the global error, as suggested by Arpe *et al.* [7] and illustrated in Figure 6.18. Of course, this conclusion is not applicable to other study cases and can under no circumstances be generalized. The application of multi-objectives genetic algorithm in a restricted search space confirms identical solutions to minimize the error on all Thoma numbers.

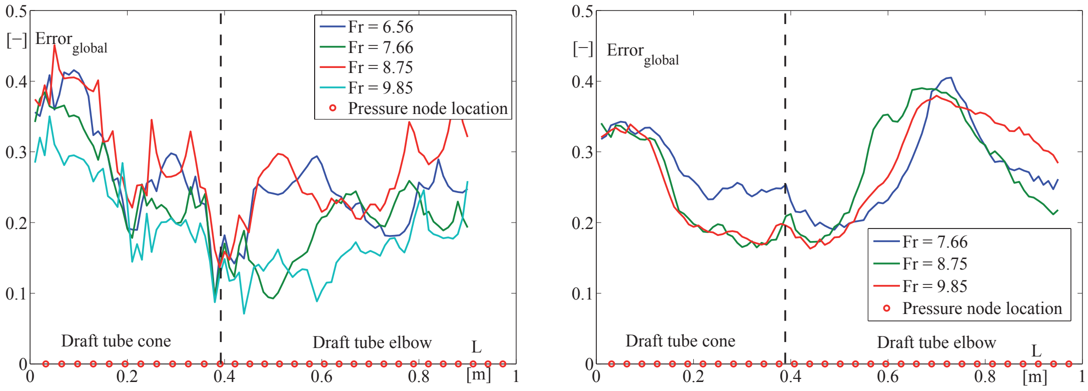

(a) Operating conditions: *PL1*

(b) Operating conditions: *PL2*

Figure 6.17: Global error for $e = 0.03$ m as a function of pressure source location L.

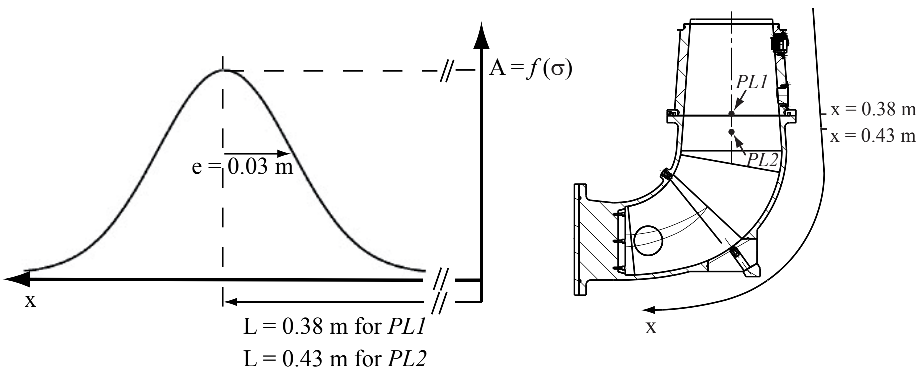

Figure 6.18: Representation of the Gaussian curve (Left) and x-axis along the draft tube (Right).

6.3.3 Study of pressure source amplitude *A*

Sensitivity analysis of the parameter A indicates a dependence of the pressure source amplitude relative to its location. Evolution of this amplitude as a function of its location L is presented in Figure 6.19. This dependence is very significant for low Thoma numbers, *i.e.* for large cavitation volumes. By contrast, for high Thoma numbers, the amplitude remains relatively constant for locations L > 0.4 m. Therefore, Dörfler's assumption is incorrect and the amplitude of the pressure source depends on the Thoma number, but also on the location of the pressure source.

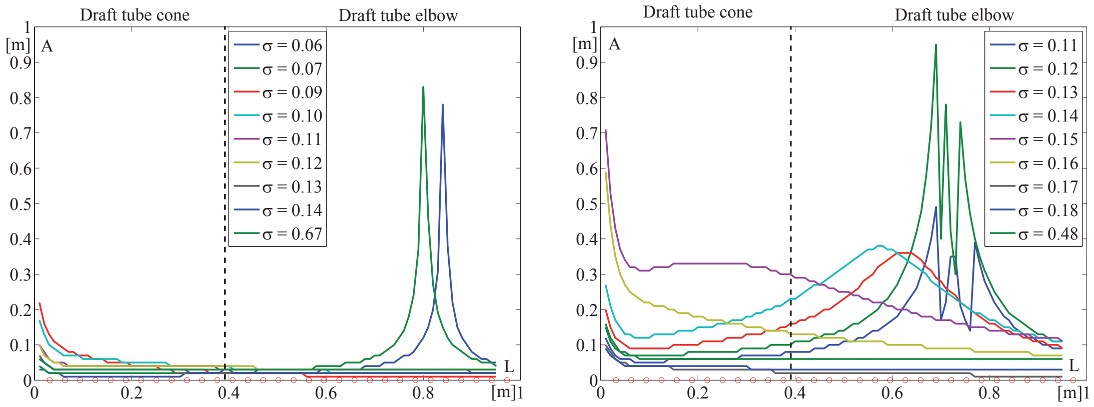

(a) Operating conditions: *PL1* Fr = 6.56

(b) Operating conditions: *PL2* Fr = 7.66

Figure 6.19: Evolution of amplitude as a function of pressure source location L.

For our case study, the sensitivity analysis of parameters L and e has established the location and standard deviation of the pressure source to minimize the global error, see Table 6.2. The amplitude of the pressure source for this location as a function of the Thoma number is shown in Figure 6.20. Generally, the amplitude increases when the Froude number increases and the maximum amplitude is always met at the same Thoma number, independently of the Froude number.

To reduce the impact of the Froude number, the amplitude is divided by the head of the Francis turbine H_{turb}, see Figure 6.21. The dimensionless values of the amplitude for high Thoma numbers are relatively similar. However, for Thoma numbers near resonance σ_{res}, the dimensionless parameter does not allow for a perfect superposition of curves. This difference may result from the error associated with the bulk viscosity, which may have an impact on the amplitude when the operating condition is close to the resonance.

Ultimately, the pressure source is difficult to generalize. A sensitivity analysis has determined that the pressure source location is in the elbow and the standard deviation should be relatively low to reduce the global error. However, the amplitude of the pressure source is very dependent on its location. It then becomes difficult to extrapolate the pressure source to other operating points.

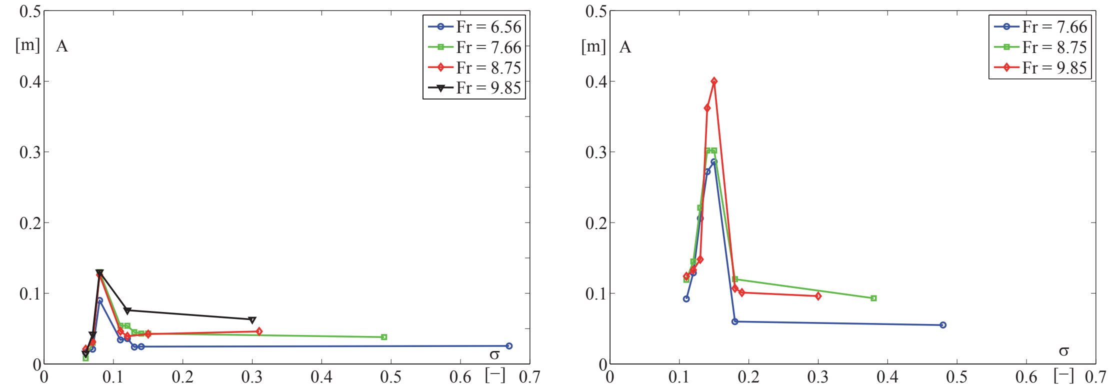

(a) Operating conditions: *PL1*

(b) Operating conditions: *PL2*

Figure 6.20: Evolution of amplitude A as a function of the Thoma number.

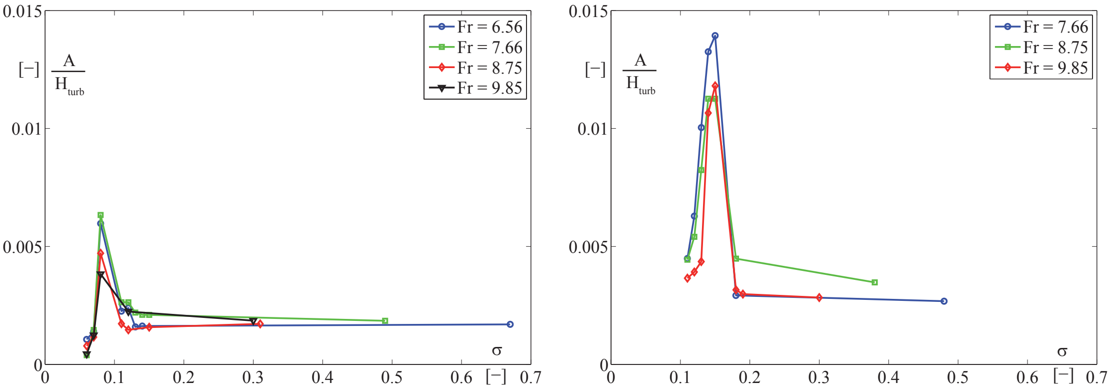

(a) Operating conditions: *PL1*

(b) Operating conditions: *PL2*

Figure 6.21: Evolution of dimensionless amplitude as a function of Thoma number.

The validation of the pressure source in the frequency domain is shown in Figures 6.22 and 6.23 for two Froude numbers. The numerical model reproduces the experimental measurements well, for every Thoma number. The highest uncertainties are exhibited in the elbow and the diffuser, where the sections are not circular. The Francis turbine location is situated at L = 0 m. The experimental values having a positive location represent the 12 pressure sensors (P1-P12) distributed along EPFL test rig PF3. The experimental values having a negative location represent the pressure sensors installed in the cone, the elbow and the diffuser of the draft tube.

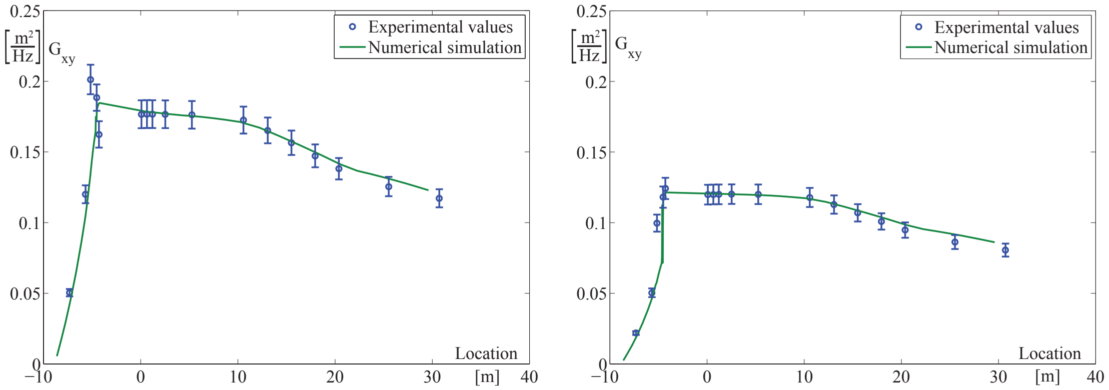

(a) Froude number = 6.56, Thoma number = 0.09 (b) Froude number = 6.56, Thoma number = 0.10

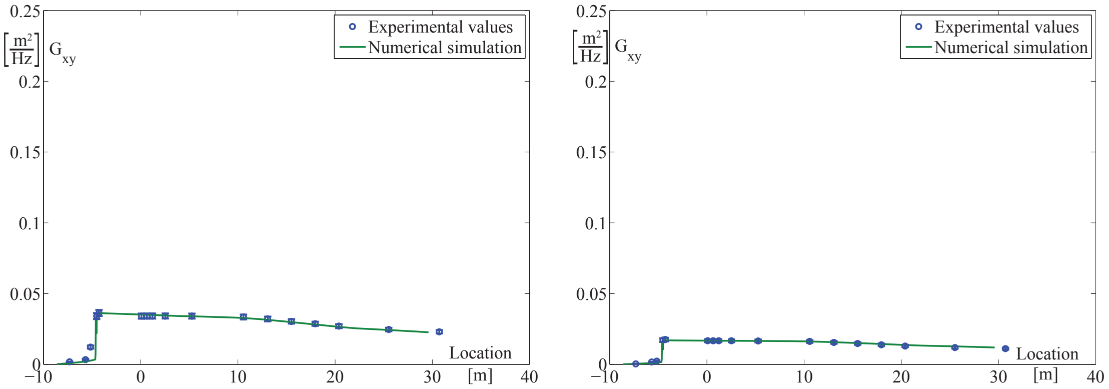

(c) Froude number = 6.56, Thoma number = 0.12 (d) Froude number = 6.56, Thoma number = 0.13

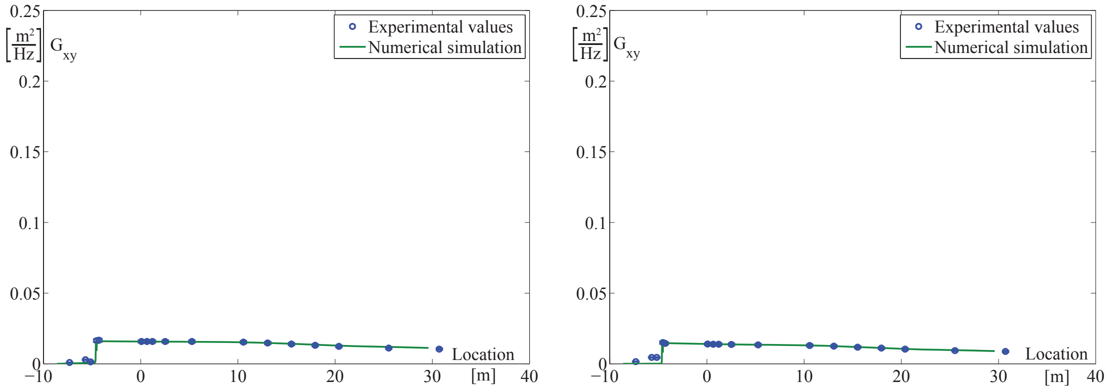

(e) Froude number = 6.56, Thoma number = 0.14 (f) Froude number = 6.56, Thoma number = Atmosphere

Figure 6.22: Comparison between experimental and numerical forced harmonic responses for the operating condition *PL1* at vortex rope frequency $f_{\text{Vortex rope}} = 2.563$ Hz

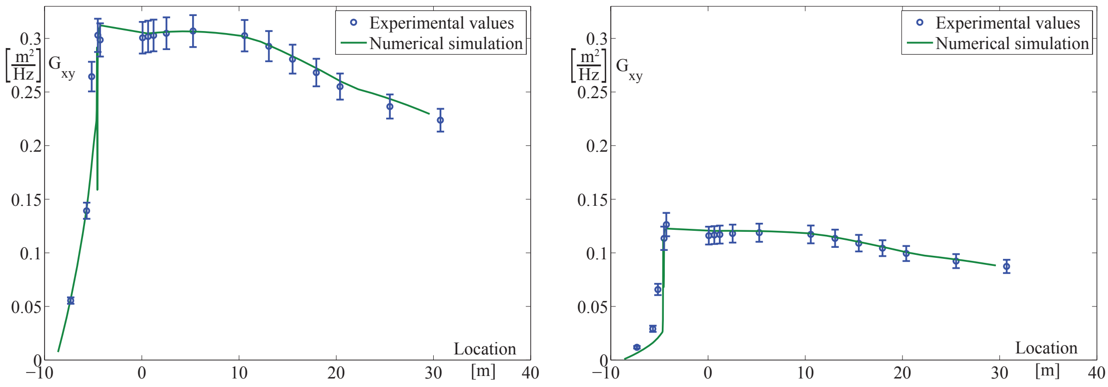

(a) Froude number = 7.66, Thoma number = 0.10

(b) Froude number = 7.66, Thoma number = 0.11

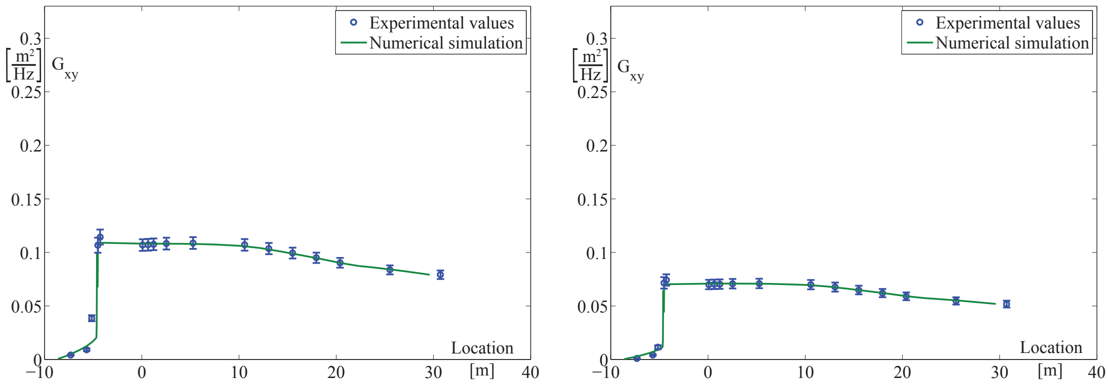

(c) Froude number = 7.66, Thoma number = 0.12

(d) Froude number = 7.66, Thoma number = 0.13

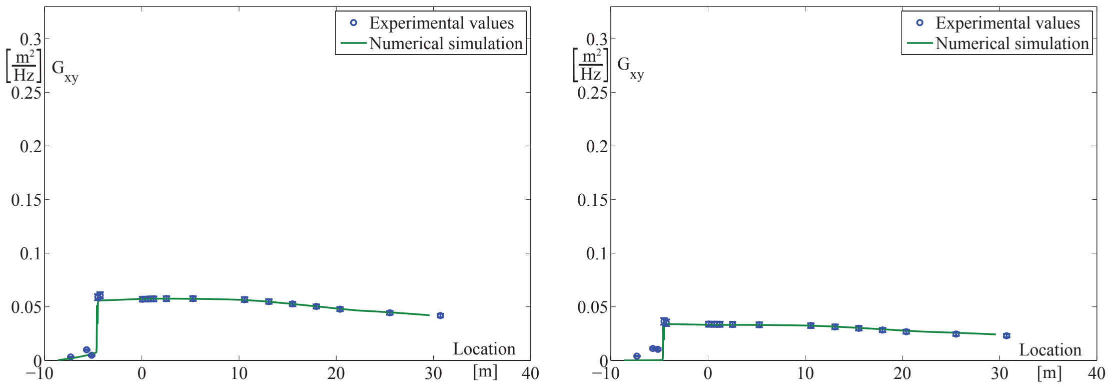

(e) Froude number = 7.66, Thoma number = 0.14

(f) Froude number = 7.66, Thoma number = Atmosphere

Figure 6.23: Comparison between experimental and numerical forced harmonic responses for the operating condition *PL1* at vortex rope frequency $f_{\text{Vortex rope}} = 2.930$ Hz

Table 6.2: Summary of pressure source information.

	L [m]	L/D_{ref} [-]	e [m]	σ_{res} [-]	$\frac{f_{res}}{n}$ [-]
PL1	0.38	1.08	0.03	0.0975	0.256
PL2	0.43	1.23	0.03	0.17	0.325

6.4 Simulation at resonance operating condition

To validate the identified hydroacoustic parameters, a time simulation is performed at resonance conditions and the numerical results are compared with experimental data. Thus, in first step, the evolution of void fraction is estimated using high-speed visualizations presented in Subsection 6.1.2. The evolution of the void fraction for discharge factor $Q_{ED} = 0.128$ and a Froude number $Fr = 8.75$ at the resonance operating condition is presented in Figure 6.24 (Left). From these experimental data, a sine law is formulated and injected into the numerical model of the EPFL test rig PF3. In a second step, the adjusted Rath's equation for the wave speed, the dimensionless bulk viscosity equation, see Equations 6.8 and 6.12, and the pressure source are implemented in the draft tube model. The time evolution of the wave speed and bulk viscosity are shown in Figure 6.24 (Left).

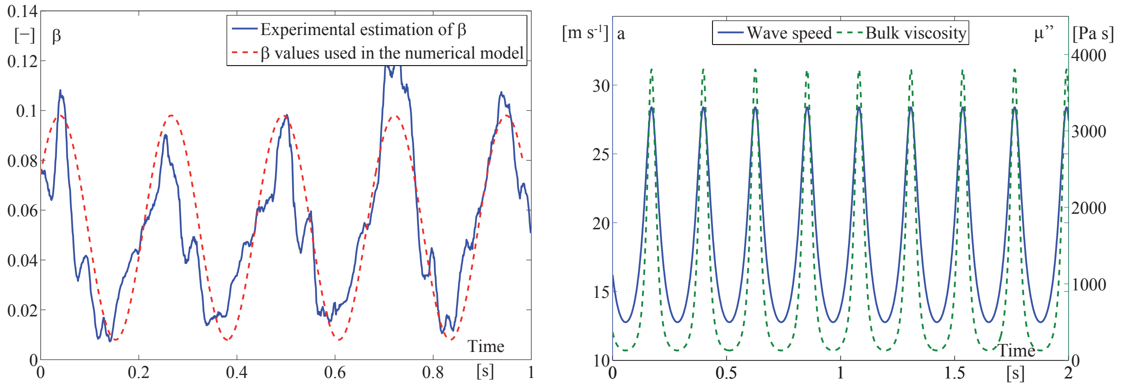

(a) For the local experimental void fraction

(b) For the wave speed and the bulk viscosity

Figure 6.24: Time evolution of the hydroacoustic parameters.

The comparison between the experimental data and the numerical model is performed in two distinct locations. In figure 6.25 (Left), the numerical model is compared with four pressure sensors located in the cone. In figure 6.25 (Right), the numerical results are compared with the reference pressure sensor $P1$ at the turbine inlet. In both cases, the numerical model is in perfect agreement with the experimental measurements. However, the numerical model slightly overestimates the pressure fluctuations on the EPFL test rig PF3. This feature comes from the local measurement of void fraction. As noted in Subsection 6.1.2, the local experimental void fraction measurement slightly overestimates the mean value of the void fraction in the draft tube. Therefore, this error is reflected in the computation of the wave speed and the bulk viscosity, and leads to an underestimation of the damping. Finally, this analysis in time domain validates the dimensionless laws of the hydroacoustic parameters, and certifies the ability of the numerical model to simulate the behavior of the hydraulic turbine in resonance conditions.

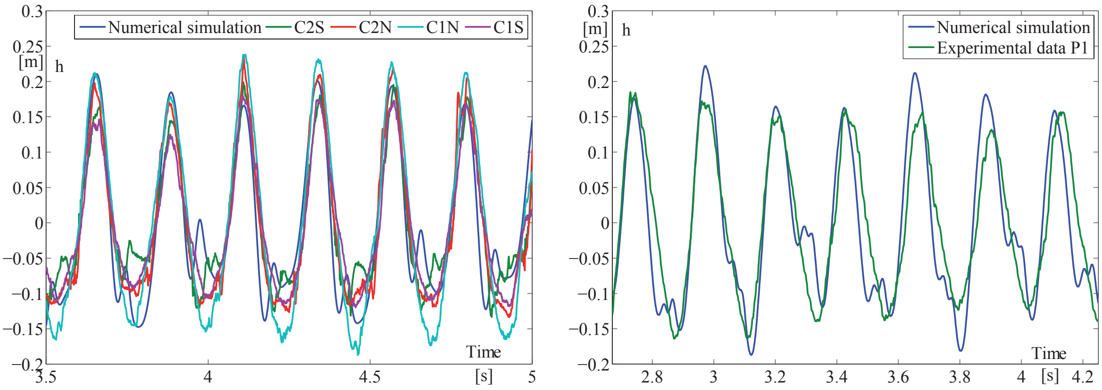

(a) For pressure sensors in the cone

(b) For the pressure sensors P1 at turbine inlet

Figure 6.25: Comparison between the experimental data and the numerical values at resonance operating condition.

6.5 Comparison of different draft tube models

In this section, the various terms of the momentum equation will be analyzed to determine their impact on the identification of hydroacoustic parameters (the wave speed, bulk viscosity and pressure source) and on the dimensionless parameters (void fraction, dimensionless wave speed and dimensionless bulk viscosity). Thus, the draft tube has been modeled using 4 different models:

1. **Viscolelastic pipes:** The various components of the draft tube are modeled with the viscoelastic pipes described in Section 5.1. Thus, the convective term and the divergent geometry are not taken into account. The momentum equation can be rewritten as:

$$\frac{1}{gA}\frac{\partial Q}{\partial t}+\frac{\lambda|Q|}{2gDA^2}Q+\frac{\partial h}{\partial x}-\frac{\mu''}{\rho gA}\frac{\partial^2 Q}{\partial x^2}=0 \tag{6.15}$$

2. **Convective terms:** The various components of the draft tube are modeled with the draft tube modeling described in Chapter 2. In this specific case, the divergent geometry of the draft tube is not taken into account and the section of each element is defined as constant. Thus, the impact of the convective term can be studied. The momentum equation can be rewritten as:

$$\frac{1}{gA}\frac{\partial Q}{\partial t}+\left(\frac{Q}{gA^2}\right)\frac{\partial Q}{\partial x}+\frac{\lambda|Q|}{2gDA^2}Q+\frac{\partial h}{\partial x}-\frac{\mu''}{\rho gA}\frac{\partial^2 Q}{\partial x^2}=0 \tag{6.16}$$

3. **Draft tube Model S:** The various components of the draft tube are modeled with the draft tube modeling described in Equation 2.11. Alligné *et al.* assumed that the dissipation induced by the variation of the cross-section is negligible. Thus, the impact of the divergent geometry can be analyzed.

$$\frac{1}{gA}\frac{\partial Q}{\partial t}+\left(\frac{Q}{gA^2}\right)\frac{\partial Q}{\partial x}+\left(\frac{\lambda|Q|}{2gDA^2}-\frac{K_xQ}{gA^3}\right)Q+\frac{\partial h}{\partial x}-\frac{\mu''}{\rho gA}\frac{\partial^2 Q}{\partial x^2}=0 \tag{6.17}$$

4. **Draft tube Model G:** The various components of the draft tube are modeled with the draft tube modeling described in Equation 2.10. Thus, Alligné's assumption is analyzed and its impact on the identification of hydroacoustic parameters is quantified.

$$\frac{1}{gA}\frac{\partial Q}{\partial t}+\left(\frac{Q}{gA^2}-\frac{2K_x\cdot\mu''}{\rho gA^2}\right)\frac{\partial Q}{\partial x}+\left(\frac{\lambda|Q|}{2gDA^2}-\frac{K_xQ}{gA^3}+\frac{2K_x^2\mu''}{\rho gA^3}\right)Q+\frac{\partial h}{\partial x}-\frac{\mu''}{\rho gA}\frac{\partial^2 Q}{\partial x^2}=0 \tag{6.18}$$

The methodology and algorithms presented in Chapter 3 have been applied to these 4 different models to highlight the impact of the convective term, the divergent geometry and Alligné's assumption on the hydroacoustic parameters and the dimensionless parameters.

6.5.1 Model influence on wave speed

The wave speed is adjusted in the distributed draft tube model to obtain a similar experimental natural frequency. According the results in Figure 6.26, taking into account the convective term does not influence the wave speed value. However, the divergent geometry imposes a reduction of wave speed of 16%. Indeed, since this term tends to destabilize the system [14], the dissipative term in Equation 3.7 decreases and the natural frequency of the numerical model increases. To compensate for this effect, the wave speed value must decrease so that the natural frequency of the numerical model matches the experimental frequency. It is to be noted that the terms neglected by Alligné *et al.* do not influence the identification of the wave speed.

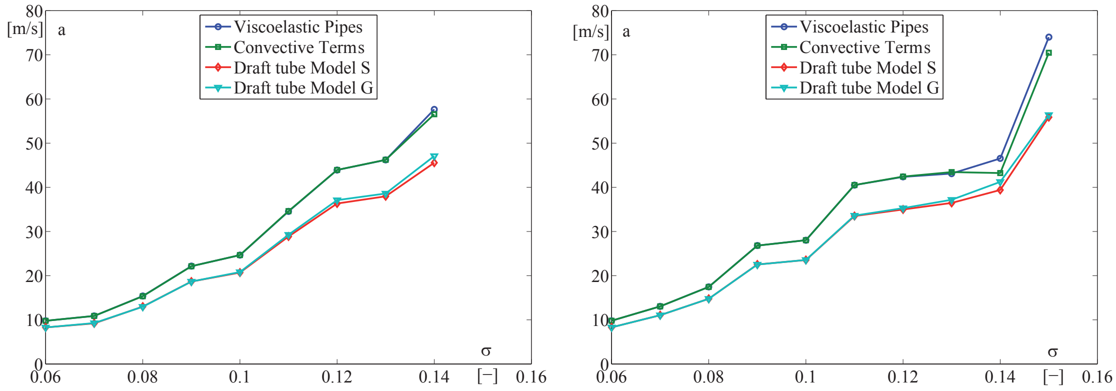

(a) Operating conditions: *PL1* Fr = 6.56

(b) Operating conditions: *PL1* Fr = 7.66

Figure 6.26: Model influence on wave speed.

6.5.2 Model influence on bulk viscosity

The bulk viscosity is adjusted in the draft tube model to obtain the same forced harmonic response measured experimentally. As was observed for the wave speed, the impact of the convective term is also negligible here. Only the divergent geometry has a large impact on the bulk viscosity and requires a reduction in the value of 45 %. Since the divergent geometry is represented by a hydraulic resistance, the dissipation of the energy injected into the numerical model is increased. To compensate for this hydraulic resistance and still maintain a forced harmonic response in good agreement with the experimental results, the dissipation induced by μ'' must be reduced. Finally, Alligné's assumption imposes a significant modification of the dissipation. Since the two additional terms in the *Draft tube model G* depend linearly on the bulk viscosity μ'', the impact is low when the Thoma number is low and increases when the cavitation volume decreases. A sensitivity analysis of these two new terms indicates that the new source term tends to reduce the bulk viscosity while the new hydraulic resistance greatly increases the bulk viscosity. Therefore, Alligné's assumption cannot be taken into account for the identification of the bulk viscosity since it induces an underestimation of this hydroacoustic parameter.

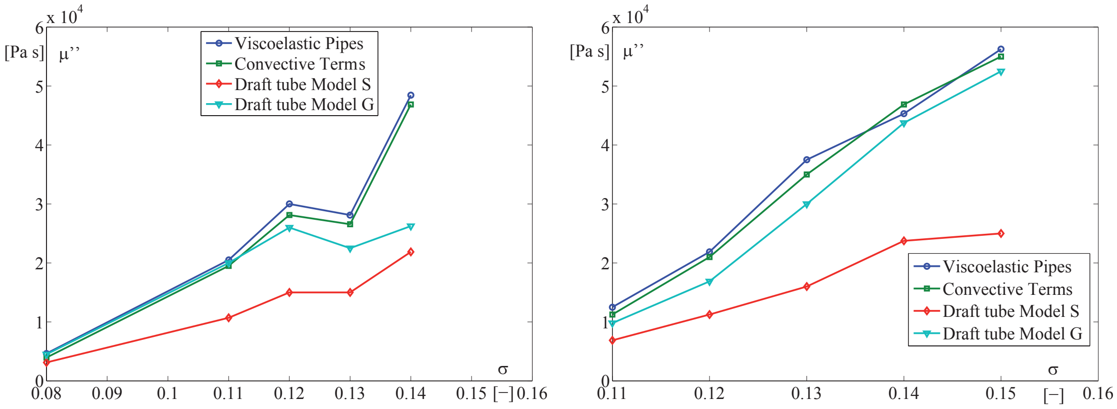

(a) Operating conditions: *PL1* Fr = 6.56

(b) Operating conditions: *PL1* Fr = 7.66

Figure 6.27: Model influence on bulk viscosity.

6.5.3 Model influence on the pressure source

The genetic algorithm applied to the numerical models always converges to the same minimum. This is due to the application of the genetic algorithm to the off-resonance system. Since the frequency of the vortex rope precession does not match the first eigenfrequency of the test rig, the wave speed and bulk viscosity have no direct impact on the pressure source. Thus, as shown in Figure 6.28, the amplitude and location of the pressure source are almost identical, independently of the chosen numerical model.

6.5.4 Model influence on void fraction

The void fraction is analytically computed using the definition of the cavitation compliance and is directly linked with the wave speed, see Equation 3.13. Therefore, similar conclusions than those drawn for wave speed are applicable to the void fraction. The divergent geometry induces an increased of the void fraction of 43 %.

6.5.5 Model influence on dimensionless wave speed

Dimensionless wave speed is a term used to compare wave speeds for different operating conditions and thus predict wave speed values for non-studied operating conditions. For four

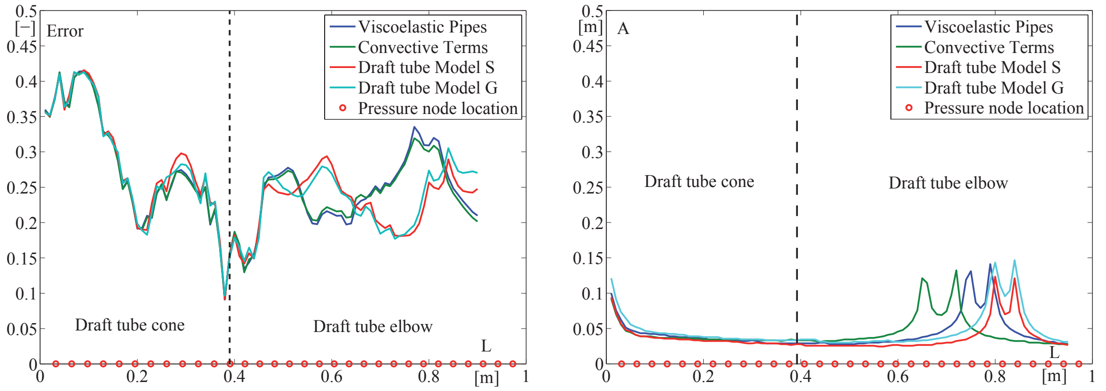

(a) Model influence on the global error

(b) Model influence on the amplitude

Figure 6.28: Model influence on the pressure source with a standard deviation $e = 0.03$ for the operating condition *PL1* and a Froude number Fr = 6.56.

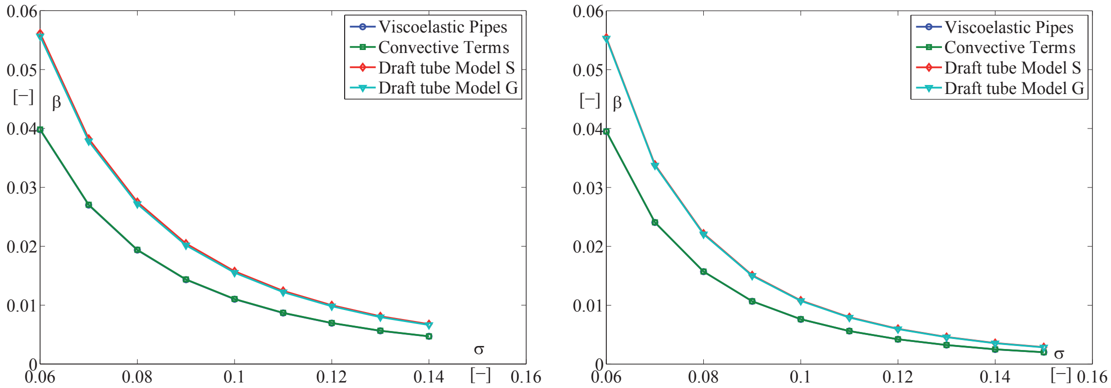

(a) Operating conditions: *PL1* Fr = 6.56

(b) Operating conditions: *PL1* Fr = 7.66

Figure 6.29: Model influence on void fraction.

different models studied, the same regression curve is obtained, indicating an independence of the curve from the numerical model, see Figure 6.30. This observation has been validated by studying the regression curve. The link between the void fraction β_{DTM} and the dimensionless wave speed Π_{DTM} computed with the draft tube model (DTM) can be written as a function of the regression coefficients p_1 and p_2:

$$\Pi_{DTM} = p_1 \cdot \beta_{DTM}^{p_2} \tag{6.19}$$

where $p_1 = 0.6201$ and $p_2 = -0.8632$. According to Equations 3.13 and 6.4, the dimensionless parameters depend on wave speed squared. Moreover, according to previous studies, the wave speed is reduced by 16% when the divergent geometry is taken into account. So there is a linear relation between the wave speed calculated with viscoelastic model a_{visco} and the wave speed calculated with the draft tube model a_{DTM}.

$$a_{visco} = \alpha \cdot a_{DTM} \tag{6.20}$$

Equation 6.19 can be rewritten as:

$$\frac{\Pi_{visco}}{\alpha^2} = p_1 \alpha^{(2p_2)} \cdot \beta_{visco}^{p_2} \tag{6.21}$$

As the results obtained with the viscoelastic model follow a similar regression, the above equation can be rewritten as:

$$\alpha^{2p_2+2} = 1 \tag{6.22}$$

Thus, the superposition of the regression curves is intrinsically linked to the coefficient p_2, confirming independence of the regression curve from the numerical model.

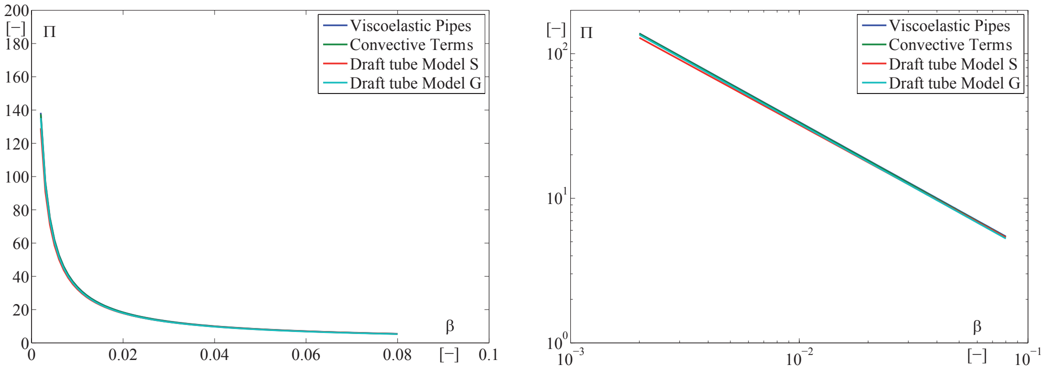

Figure 6.30: Model influence on dimensionless wave speed.

6.5.6 Model influence on dimensionless bulk viscosity

The different conclusions drawn for dimensionless wave speed can be applied to dimensionless bulk viscosity. There is still a slight difference in the coefficients of the regression curves, but it is to be considered as insignificant, see Figure 6.31.

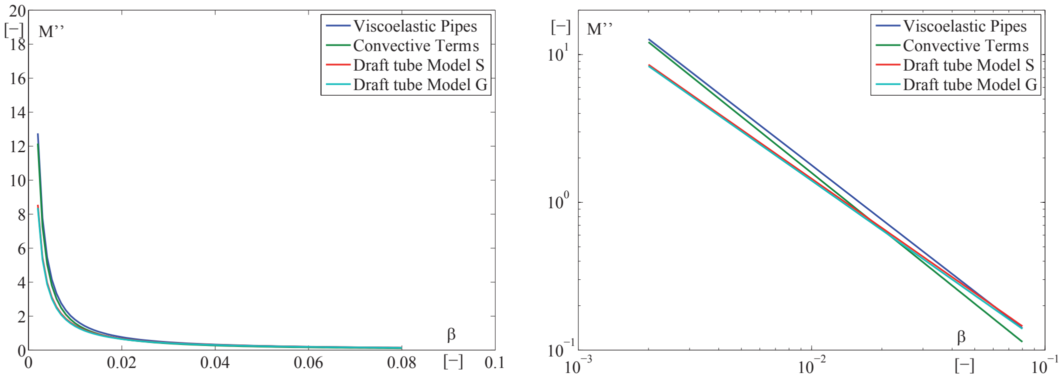

Figure 6.31: Model influence on the dimensionless bulk viscosity.

Finally, the choice of the numerical model for the draft tube influences hydroacoustic parameters. To ensure good accuracy of the hydroacoustic parameters, the draft tube model must be chosen such as to take into account the destabilizing effect imposed by the divergent geometry. Additionally, the convective term does not influence the results and Alligné's assumption induces an underestimation of the bulk viscosity. Finally, the dimensionless curves are independent from the selected numerical model and can be used in every case to link the void fraction to the dimensionless wave speed or the dimensionless bulk viscosity.

6.6 Transposition to the prototype

Using the methodology proposed in Chapter 3, hydroacoustic parameters required for draft tube modeling have been identified. To investigate the stability operation of the prototype, these hydroacoustic parameters need to be transposed to the prototype conditions according to similitude laws.

First, the influence of the Reynolds number on the transposition is assumed to be negligible. Secondly, by assuming both Thoma similitude and Froude similitude conditions, the void fraction, the dimensionless wave speed Π and the dimensionless bulk viscosity M'' are considered identical between the reduced-scale physical model and the prototype. With a dimensionless analysis, transposition relations for the wave speed, the bulk viscosity and the pressure source are developed.

6.6.1 Similitude law of wave speed

By definition, the dimensionless wave speed depends on wave speed, water density and the difference between pressure outlet and saturated vapor pressure. According to the definition of the local cavitation factor χ_E, see Equation 1.4, the definition of the dimensionless wave speed can be rewritten as:

$$\Pi = \frac{\rho_w a^2}{p_{Outlet} - p_v} = \frac{a^2}{\chi_E E} \Leftrightarrow a^2 = \Pi \chi_E E \tag{6.23}$$

Expressing the definition of the speed factor n_{ED}, the specific energy E of the turbine is a function of the reference diameter D_{ref} and the runner frequency n. It is therefore possible to write:

$$E \sim D_{ref}^2 \cdot n^2 \tag{6.24}$$

Hence, the similitude law for wave speed between the prototype and the reduced-scale physical model is:

$$a^P = a^M \left(\frac{D_{ref}^P}{D_{ref}^M} \right) \left(\frac{n^P}{n^M} \right) \tag{6.25}$$

where the superscripts P and M represent values for the prototype and the model, respectively. Additionally, it is important to note that the assumption stating that the compressibility of the pipe is negligible in comparison with the cavitation compliance remains valid for the full-scale turbine.

6.6.2 Similitude law of bulk viscosity

By definition, the dimensionless bulk viscosity depends on the bulk viscosity, the natural frequency and the difference between the pressure outlet and the saturated vapor pressure. According to the definition of the local cavitation factor χ_E, see Equation 1.4, the definition of the dimensionless bulk viscosity can be rewritten as:

$$M'' = \frac{\mu'' f_{natural}}{p_{Outlet} - p_v} = \frac{\mu'' f_{natural}}{\chi_E \rho_w E} \Leftrightarrow \frac{\mu''}{\rho_w} = \frac{M'' \chi_E E}{f_{natural}} \tag{6.26}$$

Expressing the dimensions of the specific energy of the turbine E as a function of the reference diameter and the runner frequency, it can be defined:

$$\frac{\mu''}{\rho_w} \sim \frac{D_{ref}^2 \cdot n^2}{f_{natural}} \tag{6.27}$$

Hence, the similitude law for bulk viscosity between the prototype and the reduced-scale physical model is:

$$\mu''^P = \mu''^M \left(\frac{D_{ref}^P}{D_{ref}^M}\right)^2 \left(\frac{n^P}{n^M}\right)^2 \left(\frac{f_{natural}^M}{f_{natural}^P}\right) \tag{6.28}$$

The natural frequency of the prototype is identified with a numerical model of the complete hydroelectric power plant and the transposed wave speed.

6.6.3 Similitude law of the pressure source

Thoma and Froude similitudes provide an equivalent shape of cavitation vortex rope between the reduced-scale physical model and the prototype. Thus, the interaction between the cavitation vortex rope and draft tube elbow is identical and the location of the pressure source is similar: $L = 1.08 \cdot D_{ref}^P$ for the first operating condition *PL1* and $L = 1.23 \cdot D_{ref}^P$ for the second operating condition *PL2*. Regarding the dimensionless amplitude of the pressure source, the following similitude law can be defined:

$$A^P = A^M \left(\frac{D_{ref}^P}{D_{ref}^M}\right) \tag{6.29}$$

By applying the similitude laws to the reduced-scale physical model presented in Chapter 4, hydroacoustic parameters values are obtained and shown in Table 6.3 for plant values of Thoma and Froude numbers. To validate the similitude laws, transposed draft tube parameters will be injected in a model of the complete hydroelectric power plant to simulate system response. This study will be the second part of the *HYPERBOLE* collaborative research project in association with the world major turbine manufacturers. The validation of the hydropower plant model will be done by comparison of numerical results with experimental measurements of the pressure sensors in time and frequency domains.

Table 6.3: Transposition of the hydroacoustic parameters for operating condition *PL1*.

	a [ms^{-1}]	μ'' [Pa s]	A [m]
Model	28.86	10’700	0.172
Prototype	95.44	$\frac{428'500}{f^{P}_{natural}}$	2.654

6.7 Summary and discussion

The methodology was applied to identify wave speed, bulk viscosity and pressure source for several operating conditions. Results indicate that wave speed value drops in the range from 10 m/s to 60 m/s when the cavitation vortex rope is present. Such low wave speed values imply that the convective part of the Navier-Stokes equation cannot be neglected when the cavitation vortex rope occurs. As a result, it is shown that the formulation developed by Rath to describe the wave speed in bubbly flows can be used in a cavitation vortex rope by dividing the obtained values by an empirical constant C_{adapt}. However, the value of said constant might depend on the turbine design. Therefore, the methodology presented in the current thesis should be applied to other turbines in order to verify the impact of the turbine and draft tube design on wave speed.

An equation was developed to predict the bulk viscosity caused by the cavitation vortex rope. This parameter depends on the wave speed raised to the power of four, as Pezzinga’s formula suggests. Thus, it is crucial to accurately determine the wave speed in the draft tube in order to estimate the dissipation. The presented relations for wave speed and bulk viscosity can be used in numerical models in order to accurately quantify such non-linear resonance phenomena. This will ultimately pave the way to more precise stability analysis of hydraulic machines and, hence, mitigate the issues of draft tube surge and electrical power swings.

A sensitivity analysis has determined that the pressure source location is in the elbow and the standard deviation should be relatively low to reduce the global error. However, the amplitude of the pressure source is very dependent on its location. It then becomes difficult to extrapolate the pressure source to other operating conditions.

The choice of the numerical model for the draft tube influences hydroacoustic parameters. To ensure a good accuracy of the hydroacoustic parameters, the draft tube model must be chosen to take into account the destabilizing effect imposed by the divergent geometry. By contrast, the convective term does not influence the results. Alligné’s assumption imposes a significant reduction of the dissipation. Moreover, it is important to note that the dimensionless curves are independent of the selected numerical model and can be used in every case to link the void fraction to the dimensionless wave speed or the dimensionless bulk viscosity.

Finally, to investigate the stability operation of the prototype, the hydroacoustic parameters need to be transposed to the prototype conditions according to similitude laws. By assuming both Thoma similitude and Froude similitude conditions, similitude laws were developed and the hydroacoustic parameters were predicted for the prototype. To validate the similitude laws, transposed draft tube parameters will be injected into a model of the complete hydroelectric power plant to simulate the system response. This study will be the second part of the *HYPERBOLE* collaborative research project in association with the world major turbine manufacturers. The validation of the hydropower plant model will be done by comparison of numerical results with experimental measurements of pressure sensors in time and frequency domains.

7 Simplified methodology for identification of the hydroacoustic parameters

The purpose of this chapter is to provide a simplified methodology to identify the hydroacoustic parameters. Using the dimensionless curves and sensitivity analyzes developed in Chapter 6, the methodology presented in Chapter 3 can be simplified and applied to any type of hydraulic test rig. Additionally, this chapter is independent of the rest of the document and, therefore, the general context and assumptions are quickly described.

The hydraulic machines subject to off-design operation involve the presence of cavitating flow regimes in the draft tube. The cavitation vortex rope at part load conditions is described as an excitation source for the hydraulic system and interactions between this excitation source and system eigenfrequency may result in resonance phenomena and induce a draft tube surge and electrical power swings. The methodology proposed in the *HYPERBOLE* collaborative research project for assessing pressure fluctuations experienced by the hydraulic turbine or pump-turbine unit in a power plant is given in Figure 7.1. Instead of directly transposed pressure fluctuations measured on the reduced-scale physical model, the purpose is to identify hydroacoustic parameters describing the dynamic flow in a reduced-scale physical model and transpose them to the full-scale turbine. Thus, the numerical simulations of the complete hydroelectric power plant will predict more accurately the pressure fluctuations.

To precisely predict and simulate the pressure fluctuation, proper modeling of the draft tube is critical. The presence of this cavitation vortex rope requires a numerical pipe element taking into account the complexity of the two-phase flow. Among the parameters describing the numerical model of the cavitating draft tube flow, three hydroacoustic parameters requires a special attention: the wave speed, the bulk viscosity and the pressure source.

The simplified methodology still requires the development of a numerical model of the studied hydraulic system, as well as an external excitation system for identifying the natural frequency of the hydraulic system. However, the identification of the bulk viscosity can be directly computed with Equation 6.12. Moreover, with the dimensionless numbers Π and M'', the wave speed and the bulk viscosity can be extrapolated to all operating conditions if the void fraction and the pressure at the turbine outlet are measured.

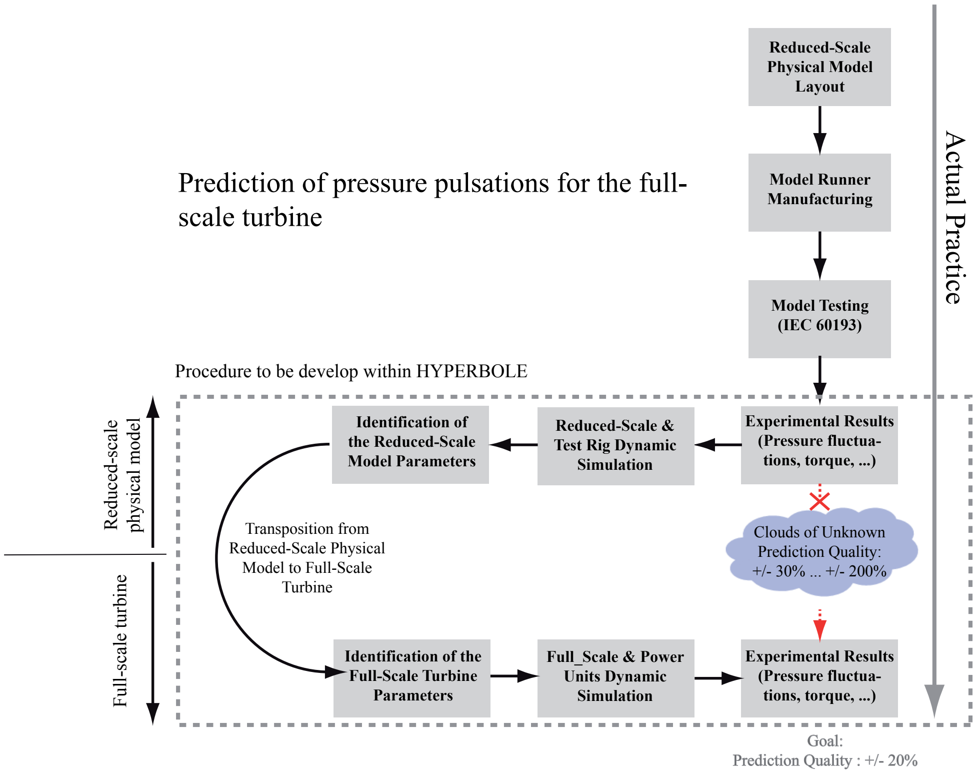
Reduced-Scale Physical Model Layout
Model Runner Manufacturing
Model Testing (IEC 60193)
Actual Practice
Prediction of pressure pulsations for the full-scale turbine
Procedure to be develop within HYPERBOLE
Reduced-scale physical model
Full-scale turbine
Identification of the Reduced-Scale Model Parameters
Reduced-Scale & Test Rig Dynamic Simulation
Experimental Results (Pressure fluctuations, torque, ...)
Transposition from Reduced-Scale Physical Model to Full-Scale Turbine
Clouds of Unknown Prediction Quality: +/- 30% ... +/- 200%
Identification of the Full-Scale Turbine Parameters
Full_Scale & Power Units Dynamic Simulation
Experimental Results (Pressure fluctuations, torque, ...)
Goal:
Prediction Quality : +/- 20%

Figure 7.1: Methodology developed for assessing pressure fluctuations experienced by hydraulic power plant.

First, the important parameters of the numerical model are presented. Then, the experimental instrumentation setup is described to obtain the data necessary for the simplified methodology. Finally, the procedure is presented to identify the wave speed, the bulk viscosity and the pressure source.

7.1 Hydroacoustic model

- A modeling of the test rig is necessary to identify the hydroacoustic parameters of the draft tube model. The one-dimensional model of the hydraulic system is setup with EPFL SIMSEN software.

- The hydraulic pipes of the test rig are modeled with a viscoelastic pipe model. The value of the wave speed is crucial to simulate a correct eigenshape and depends on the degassing procedure. By knowing the rate of gas dissolved in water, the wave speed is computed using Rath's equation 6.8. If the gas concentration is unknown, it can be deduced by comparing the numerical dimensionless harmonic response with experimental data. Additionally, viscoelastic resistance does not influence the numerical forced harmonic response and the second viscosity μ' may be set to zero.

- The wave speed in the spiral casing has little influence on the numerical forced harmonic response. An approximation of this value is more than enough if the length of the spiral casing is small compared to the length of the studied test rig.
- The hydraulic turbine and the feeding pump are modeled with characteristic curves. A good discretization of the hill chart reduces the risk of numerical instability.
- The draft tube should be modeled using the *Draft tube Model G* to take into account the divergent geometry.

7.2 Test installation

- A minimum of five pressure sensors are located along the test rig pipe. The location of the pressure sensors is deliberately concentrated on the first part of the test rig to reduce the error of the eigenshape measurements. These measurements are synchronized with the test rig parameters measurement, such as Thoma number, head, discharge and torque.
- A minimum of three pressure sensors are located in the same cross-section of the cone to separate the convective part from the synchronous part.
- An excitation system is necessary to inject or extract a periodical discharge at a given frequency in the upstream pipe. This system is composed of a rotating valve, a variable speed pump to control the amplitude of the excitation and an air-vessel to ensure hydroacoustic decoupling between the injection pump and the entire hydraulic circuit.
- The rotating valve is driven by a variable speed motor to excite the hydraulic test rig at frequencies ranging from 1 Hz to 15 Hz.
- Two optional pressure sensors can be installed on the excitation system pipe to measure the fluctuating discharge with a Pressure-Time method. However, this information is not necessary for this simplified method.
- Pressure sensors can be added to the elbow and the diffuser of the draft tube to improve the spatial resolution of the eigenshape. However, due to the non-circular sections, the uncertainty of the pressure measurements is high.

7.3 Acquisition and processing of the data

- Dynamic wall pressure measurements are carried out by making use of flush-mounted piezoresistive pressure sensors.
- The sampling frequency is set to 1000 Hz to capture all physical phenomena that could influence hydroacoustic parameters.

- Output signals are simultaneously acquired during three-minute runs on a acquisition device.
- Since pressure signals for a part load operating condition are not perfectly periodic, a Hamming window is applied to the spectral analysis with a 50% overlap.

7.4 Test procedures

- For a given operating condition, the natural frequency is identified with the excitation system. The excitation frequency is generated by the rotation of a cylindrical valve and the amplitude is controlled by a feeding pump. For each excitation frequency, the forced harmonic response of the hydraulic system is measured with pressure sensors densely located along the hydraulic circuit. A spectral analysis of the forced harmonic response for all excitation frequencies is used to identify the natural frequency of the hydraulic system.
- The wave speed is adjusted in the distributed draft tube model to obtain a similar experimental natural frequency. Injecting the value of the wave speed in Equation 3.1, the cavitation compliance can be determined.
- By identifying the wave speed for five Thoma numbers, the value of the cavitation volume and the void fraction can be deduced from a power law regression with Equation 6.1 and 6.2. By studying more than five Thoma numbers, the quality of the regression can be improved.
- With the mean pressure at the turbine outlet, the dimensionless wave speed can be computed. The ratio between the theoretical values given by Rath and the wave speed inferred from experimental data is computed. With this constant, the value of the wave speed can be extrapolated to different void fractions.
- With the void fraction, the wave speed and the pressure at the turbine outlet, the bulk viscosity can be directly computed with Equation 6.12. For high value of bulk viscosity, the natural frequency of the numerical model must be verified. If the natural frequency is modified by the bulk viscosity, then the wave speed is adapted to match the natural frequency measured experimentally.
- With the dimensionless numbers Π and M'', the wave speed and the bulk viscosity can be extrapolated to all operating conditions if the void fraction and the pressure at the turbine outlet are measured. An approximation of the cavitation volume of the vortex rope can be achieved with a high-speed visualization of the cavitation vortex rope in the Plexiglas cone. This non-intrusive method may slightly overestimated the cavitation volume and therefore underestimated the wave speed and the bulk viscosity. If this method is not possible, then the natural frequency has to be identified with the excitation system for all required operating conditions and the wave speed will be deduced with the numerical model.

- The methodology used to identify the pressure source is based on the excitation generated by the precession of the vortex rope. The external excitation system is not required. The three parameters describing the Gaussian curve are identified with a multi-objectives algorithm. To reduce the search space, the standard deviation should be low to reduce the global error, without causing a dependency of the numerical discretization. Thus, the standard deviation should be higher than the elementary pipe length *dx*. Additionally, the pressure source is usually located in the draft tube elbow.

  With these restrictions of the search space, the genetic algorithm can converge to a global minimum. The algorithm compares the experimental forced harmonic response of the hydraulic system excited by the precession of the vortex rope with the response of the numerical model. The comparison is quantified according to the objectives defined in Section 3.5.

This simplified method can be applied to any type of hydraulic test rig and requires little additional resources. By assuming both Thoma similitude and Froude similitude conditions, the hydroacoustic parameters can be transposed to the prototype conditions according to similitude laws 6.25, 6.28 and 6.29. The natural frequency of the prototype is identified with a numerical model of the complete hydroelectric power plant and the transposed wave speed.

8 Conclusions and Perspectives

8.1 Conclusions

The present work contributes to the modeling of the draft tube of a Francis turbine at part load conditions. The cavitation vortex rope is described as an excitation source for the hydraulic system. Interactions between this excitation source and system eigenmodes may result in resonance phenomena and induce a draft tube surge and electrical power swings. To precisely predict and simulate a part load resonance, proper modeling of the draft tube is critical. The presence in it of a cavitation vortex rope requires a numerical pipe element taking into account the complexity of the two-phase flow. From the momentum and continuity equations describing a cavitating draft tube flow, three hydroacoustic parameters require a special methodology to be quantified: wave speed, bulk viscosity and pressure source.

Several numerical models have been developed in the past to identify wave speed and bulk viscosity for bubbly air-water mixtures. However, significant differences between bubbly flow, slug flow and stratified flow indicate that the theoretical formulations are inappropriate for the case of a cavitation vortex rope. Therefore, an alternative method based on experimental data from reduced-scale physical model testing of a Francis turbine and a one-dimensional numerical model was developed to identify the three hydroacoustic parameters. The methodology is based on the direct link that exists between the natural frequency of the hydraulic system and wave speed in the draft tube. Wave speed and bulk viscosity are identified in the frequency domain and require the development of an external excitation source and the characterization of the experimental natural frequency. A sensibility analysis justified the existence of a global minimum and therefore the use of a simple and robust algorithm such as the dichotomy. The pressure source is modeled by a Gaussian curve characterized by three parameters. To identify the global minimum, the three parameters are identified with a multi-objective genetic algorithm. However, to decrease the number of solutions satisfying the different objectives, it is assumed that the location of the pressure source L and the standard deviation e are independent from the Thoma number. The major results of the present work can be summarized as follows:

- Wave speed values drop in the range from 10 m/s to 60 m/s when the cavitation vortex rope is present. With the dimensionless number Π, the dependence upon the pressure level in the draft tube is removed and all experimental values of the wave speed follow the same power law regression. The comparison with the theoretical formulation developed by Rath for bubbly flows indicates that the bubbly flow equation can be used for a cavitation vortex rope by dividing the obtained values by a constant C_{adapt}. Additionally, by knowing the wave speed for different Thoma numbers, the mean void fraction of the cavitation vortex rope V_c can be computed. The mean void fraction obtained analytically was validated with the local experimental void fraction estimated with a high-speed visualization of the cavitation vortex rope in the Plexiglas cone.

- A new equation was developed to predict the bulk viscosity caused by the cavitation vortex rope. This parameter is directly related to the dimensionless number Π, as the bubbly flow formula suggested. Thus, a fourth power dependence for the wave speed indicates that it is important to accurately determine the wave speed in the draft tube.

- A sensitivity analysis has determined that the pressure source location is in the elbow of the draft tube. This location depends on the discharge factor Q_{ED} but not the Froude number. Additionally, the amplitude of the pressure source is very dependent on its location and change as a function of the Thoma number. Therefore it becomes difficult to extrapolate the pressure source to other operating conditions. Dörfler's statement assuming that the pressure source is independent from the number of Thoma is thus erroneous. Finally, to minimize the global error and ensure the convergence of the genetic algorithm to an optimal solution, the standard deviation should be as low as possible, without causing a dependency of the numerical discretization.

- Validation of the hydroacoustic parameters identification was performed in time and frequency domains. Generally, the forced harmonic response of the experimental system is well reproduced in the frequency domain by the numerical model, independently of the discharge factor, the Froude number or Thoma number. Additionally, an analysis in time domain validates the dimensionless laws of the hydroacoustic parameters, and certifies the ability of the numerical model to simulate the behavior of the hydraulic turbine under resonance conditions.

- The choice of the numerical model for the draft tube influences the identification of hydroacoustic parameters. To ensure a good accuracy of the hydroacoustic parameters, the draft tube model must be chosen to take into account all physic terms of the momentum equation, such as the destabilizing effect imposed by the divergent geometry or the dissipation. Only the convective term does not influence the results. Alligné's assumption allows for a good identification of the wave speed, but underestimates the bulk viscosity. Moreover, it is important to note that the dimensionless curves are independent from the selected numerical model and can be used in every case to link the void fraction to the dimensionless wave speed or the dimensionless bulk viscosity.

- By assuming both Thoma similitude and Froude similitude conditions, transposition laws were developed and the hydroacoustic parameters were predicted for the prototype.

8.2 Perspectives

The aim of this thesis was to develop a simple methodology to identify critical hydroacoustic parameters for the numerical model. The influence of Froude and Thoma numbers, and discharge factor were quantified. Moreover, sensitivity studies have allowed for generalization and prediction of these parameters for any part load operating condition. For future investigations, several strategies should be considered in light of the above findings.

- The dimensionless laws developed in Chapter 6 are independent from the numerical model and the level setting of the Francis turbine. The influence of the speed factor n_{ED} remains to be determined before using these dimensionless laws for all operating conditions at part load. Thus, the methodology presented in this thesis should be applied to different speed factors to quantify its impact.
- The dimensionless wave speed depends on the parameter C_{adapt}, which is experimentally quantified. The application of the methodology presented in this thesis for other Francis turbines would identify the impact of the hydraulic machine geometry on the parameter C_{adapt}. The ultimate goal would be to predict the value of this parameter from easily quantifiable data, without having to use an external excitation system.
- The methodology used to identify the pressure source has determined its location and its amplitude. Nevertheless, the amplitude is very dependent on its location and this location depends on the discharge factor Q_{ED}. Therefore its prediction remains very difficult to quantify.
- The mass flow gain factor has been neglected in this study because its importance is minimal at part load operating conditions. However, to extrapolate the results to full load operating conditions, it would be important to quantify this parameter. Currently, the use of measurement techniques, such as Laser Doppler Velocimetry (LDV), fluorescent Particle Image Velocimetry (PIV) and high-speed flow visualization as well as the development of appropriate signal processing tools grants access to the mass flow gain factor value, but these experimental devices are expensive and of complex use. A new goal would be to develop a simple and inexpensive method to quantify and predict this hydroacoustic parameter.
- The similitude laws developed in this thesis have to be validated with experimental measurements on prototype. In the *HYPERBOLE* collaborative research project, transposed draft tube parameters will be injected into a numerical model of the complete hydroelectric power plant to simulate system response. The validation of the hydropower plant model will be done by comparison of numerical results with experimental measurements of pressure sensors in time and frequency domains.

Globally, this thesis is part of a collaborative research project to develop powerful tools for a holistic analysis of the interactions between the hydropower plant and its connected power system. Thus, research in multiple areas of expertise such as hydrodynamics, power electronics or mechanical structure dynamics are needed:

- Complementary three-dimensional unsteady numerical two-phase flow simulations are carried out at full load, part load and deep part load to determine the driving parameters of the transient behavior of the Francis turbine.
- Experimentally, a particular interest is focused on measurements of instantaneous velocity field survey by means of PIV and LDV in order to derive the instantaneous discharge in the draft tube cone.
- The modal characteristics of the Francis turbine are also calculated with the influence of the surrounding water.
- The detailed representation and modeling of the dynamic behavior of hydro units is also crucial to identify the most adequate control strategies to be included in this type of units, regarding the provision of specific services to the electric power grid.

These multidisciplinary studies are widely supported by the main hydro equipment suppliers in order to acquire detailed understanding of the dynamic loads experienced by the hydro-electrical equipment during transient operation of a hydropower plant. The technological developments that may emerge from such research may constitute a powerful tool in the grid regulation and probably impact the 20-20-20 strategic energy policy adopted by the European Union.

A Hill chart of the reduced-scale model

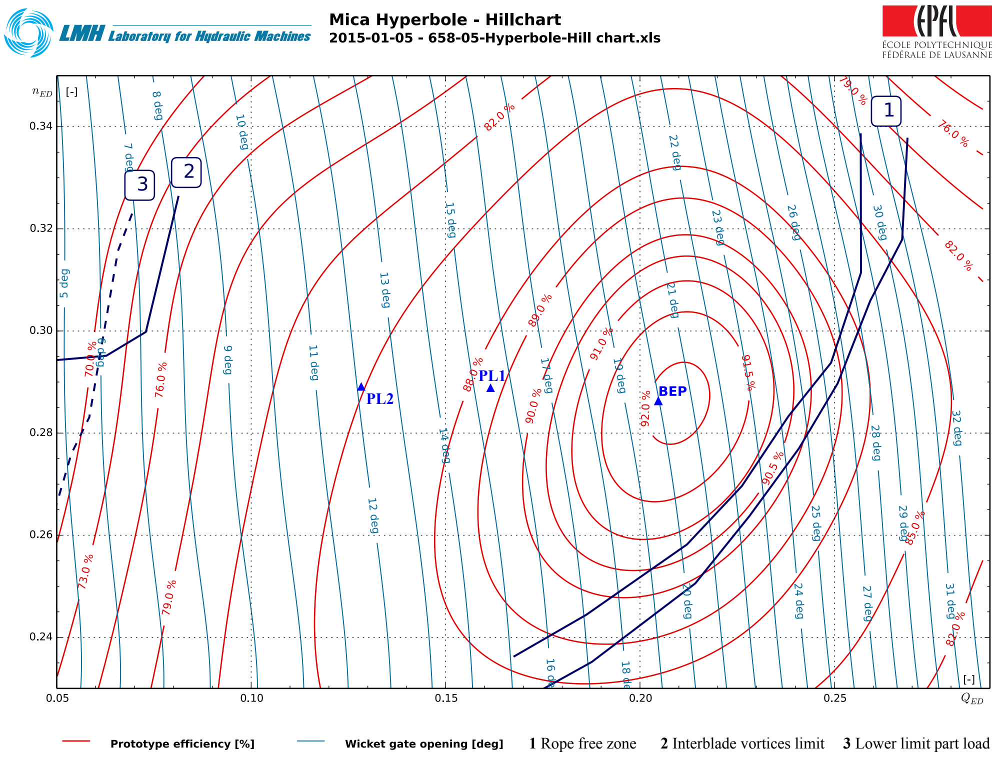

Figure A.1: Hill chart of the reduced-scale Francis turbine physical model on the EPFL test rig PF3 as a function of n_{ED} and Q_{ED}

B Dynamic pressure sensors location

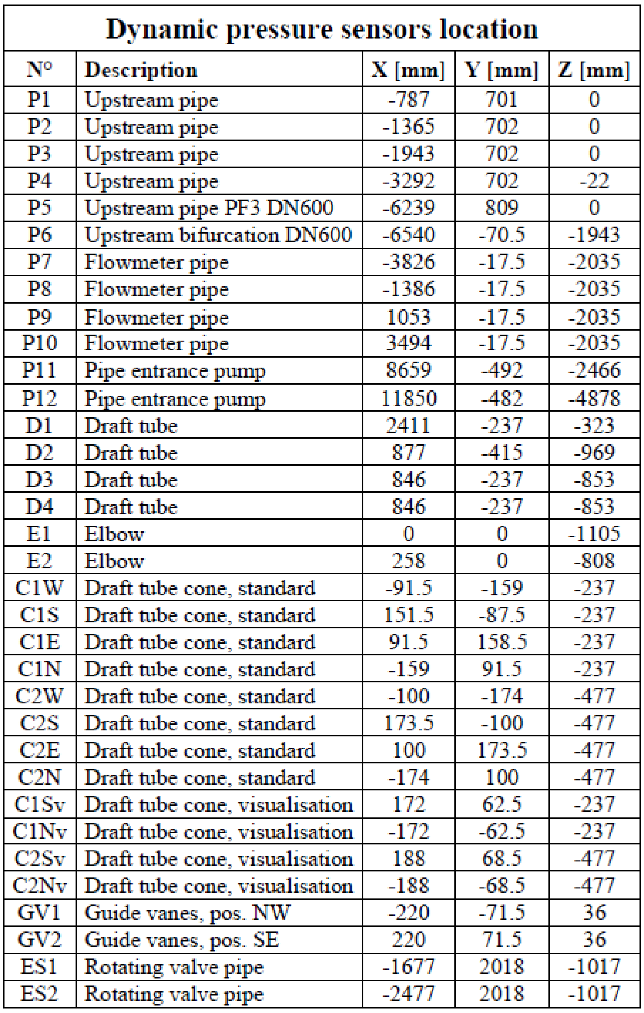

Dynamic pressure sensors location

N°	Description	X [mm]	Y [mm]	Z [mm]
P1	Upstream pipe	-787	701	0
P2	Upstream pipe	-1365	702	0
P3	Upstream pipe	-1943	702	0
P4	Upstream pipe	-3292	702	-22
P5	Upstream pipe PF3 DN600	-6239	809	0
P6	Upstream bifurcation DN600	-6540	-70.5	-1943
P7	Flowmeter pipe	-3826	-17.5	-2035
P8	Flowmeter pipe	-1386	-17.5	-2035
P9	Flowmeter pipe	1053	-17.5	-2035
P10	Flowmeter pipe	3494	-17.5	-2035
P11	Pipe entrance pump	8659	-492	-2466
P12	Pipe entrance pump	11850	-482	-4878
D1	Draft tube	2411	-237	-323
D2	Draft tube	877	-415	-969
D3	Draft tube	846	-237	-853
D4	Draft tube	846	-237	-853
E1	Elbow	0	0	-1105
E2	Elbow	258	0	-808
C1W	Draft tube cone, standard	-91.5	-159	-237
C1S	Draft tube cone, standard	151.5	-87.5	-237
C1E	Draft tube cone, standard	91.5	158.5	-237
C1N	Draft tube cone, standard	-159	91.5	-237
C2W	Draft tube cone, standard	-100	-174	-477
C2S	Draft tube cone, standard	173.5	-100	-477
C2E	Draft tube cone, standard	100	173.5	-477
C2N	Draft tube cone, standard	-174	100	-477
C1Sv	Draft tube cone, visualisation	172	62.5	-237
C1Nv	Draft tube cone, visualisation	-172	-62.5	-237
C2Sv	Draft tube cone, visualisation	188	68.5	-477
C2Nv	Draft tube cone, visualisation	-188	-68.5	-477
GV1	Guide vanes, pos. NW	-220	-71.5	36
GV2	Guide vanes, pos. SE	220	71.5	36
ES1	Rotating valve pipe	-1677	2018	-1017
ES2	Rotating valve pipe	-2477	2018	-1017

Figure B.1: Location of the dynamic pressure sensors on the EPFL test rig PF3.

Bibliography

[1] European Parliament and Council of the European Union. Directive 2009/28/EC. *Official Journal of the European Union*, 52:L140/16–62, 2009.

[2] Worldwide electricity production from renewable energy sources. *Obser'ER et la Fondation Energies pour le Monde*, Fifteenth inventory, 2013.

[3] S. Alligné. *Forced and Self Oscillations of Hydraulic Systems Induced by Cavitation Vortex Rope of Francis Turbines.* PhD thesis, EPFL, Lausanne, 2011.

[4] S. Alligné, C. Nicolet, P. Allenbach, B. Kawkabani, J. J. Simond, and F. Avellan. Influence of the francis turbine location under vortex rope excitation on the hydraulic system stability. *International Journal of Fluid Machinery and Systems*, 2, 2009.

[5] S. Alligné, C. Nicolet, Y. Tsujimoto, and F. Avellan. Cavitation surge modelling in francis turbine draft tube. *Journal of Hydraulic Research*, 52(3):399–411, May 2014.

[6] G. Angelico, F. Muciaccia, and G. Rossi. Part load behaviour of a turbine: a study on a complete model of a hydraulic power plant. *Proceedings of the 13th IAHR Symposium on Hydraulic Machinery and Systems, Beijing, China*, 1986.

[7] J. Arpe, C. Nicolet, and F. Avellan. Experimental evidence of hydroacoustic pressure waves in a francis turbine elbow draft tube for low discharge conditions. *Journal of Fluids Engineering*, 131(8):081102, 2009.

[8] F. Avellan. *Turbomachines hydrauliques: pertes énergétiques.* EPFL, Lausanne, 2007.

[9] P. Bartolini and F. Siccardi. A proposal to evaluate the energy dissipation in an unsteady two phase bubbly flow with low gas-liquid ratio. *L'Energia Electrica*, pages 387–392, 1975.

[10] J. S. Bendat and A. G. Piersol. *Random data: analysis and measurement procedures*, volume 729. John Wiley and Sons, 2011.

[11] G. Blommaert. *Etude du comportement dynamique des turbines Francis : contrôle actif de leur stabilité de fonctionnement.* PhD thesis, EPFL, Lausanne, Switzerland, 2000.

[12] U. Bolleter, E. Buehlmann, J. Eberl, and A. S. B. L. Stirnemann. Hydraulic and mechanical interactions of feedpump systems. Technical Report EPRI-TR-100990, Electric Power

Research Inst., Palo Alto, CA (United States); Sulzer Bros. Ltd., Winterthur (Switzerland), Sept. 1992.

[13] C. Brennen and A. J. Acosta. Theoritical, quasi-static analysis of cavitation compliance in turbopumps. *Journal of Spacecraft and Rockets*, 10(3):175–180, 1973.

[14] C. Chen, C. Nicolet, K. Yonezawa, M. Farhat, F. Avellan, and Y. Tsujimoto. One-dimensional analysis of full load draft tube surge. *Journal of Fluids Engineering*, 130(4):041106, 2008.

[15] M. Couston and R. Philibert. Partial load modelling of gaseous francis turbine rope. *The international journal on Hydropower and Dams*, 1:525–533, 1998.

[16] D. Covas, I. Stoianov, J. F. Mano, H. Ramos, N. Graham, and C. Maksimovic. The dynamic effect of pipe-wall viscoelasticity in hydraulic transients. part II—model development, calibration and verification. *Journal of Hydraulic Research*, 43(1):56–70, 2005.

[17] P. K. Doerfler. Modèle mathématique des oscillations excitées à charge partielle par la torche de cavitation dans les turbines francis. *Bulletin Escher Wyss*, 1980.

[18] P. K. Doerfler. Saugrohrschwingungen in systemen mit francisturbinen bei anregung durch den teillast-wirbelzopf. Technical Report WT-83-641, Escher Wyss, Zürich, Oct. 1982.

[19] P. K. Doerfler. System dynamics of the francis turbine half load surge. *11th IAHR Symposium on the Hydraulic Machinery and systems, Amsterdam, Netherlands*, 1982.

[20] P. K. Doerfler. Evaluating 1d models for vortex-induced pulsation in francis turbines. *3rd IAHR International Meeting of the Workgroup on Cavitation and Dynamic Problems in Hydraulic Machinery and Systems*, 2009.

[21] P. K. Doerfler and N. Ruchonnet. A statistical method for draft tube pressure pulsation analysis. In *IOP Conference Series: Earth and Environmental Science*, volume 15, page 062002. IOP Publishing, 2012.

[22] P. K. Dörfler, M. Keller, and O. Braun. Francis full-load surge mechanism identified by unsteady 2-phase CFD. *IOP Conference Series: Earth and Environmental Science*, 12:012026, Aug. 2010.

[23] H. Duan, M. Ghidaoui, P. Lee, and Y. Tung. Relevance of unsteady friction to pipe size and length in pipe fluid transients. *Journal of Hydraulic Engineering*, 138(2):154–166, 2012.

[24] D. Ewing. Allowing for free air in waterhammer analysis. *Proceedings of the 3rd International Conference on Pressure Surges, Canterbury, UK*, pages 127–146, 1980.

[25] M. Farhat, S. Natal, F. Avellan, F. Paquet, P. Lowys, and M. Couston. Onboard meausrements of pressure and strain fluctuations in a model of low head francis turbine - part 1: Instrumentation. In *Proceedings of the 21st IAHR Symposium on Hydraulic Machinery and Systems*, Lausanne, Switzerland, 2002.

[26] A. Favrel, C. Landry, A. Mueller, K. Yamamoto, and F. Avellan. Hydro-acoustic resonance behavior in presence of a precessing vortex rope: The observation of a lock-in effect at partial load francis turbine operation. *27th IAHR Symposium on Hydraulic Machinery and Systems, Montrea, Canadal*, 2014.

[27] J.-P. Franc, F. Avellan, B. Belhadji, J.-Y. Billard, L. Briançon-Marjolet, D. Fréchou, D. H. Fruman, A. Karimi, J.-L. Kueny, and J.-M. Michel. *La Cavitation: Mécanismes Physiques et Aspects Industriels.* Collection Grenoble Sciences. Presse Universitaires de Grenoble, Grenoble, 1995.

[28] N. R. Gibson. The Gibson method and apparatus for measuring the flow of water in closed conduits. *ASME Power Division*, pages 343–392, 1923.

[29] F. Hachem. *Monitoring of Steel Lined Pressure Shafts Considering Water-Hammer Wave Signals and Fluid-Structure Interaction.* PhD thesis, EPFL, Lausanne, 2011.

[30] R. E. Henry, M. A. Grolmes, and H. K. Fauske. Propagation velocity of pressure waves in gas-liquid mixtures. *Cocurrent Gas-Liquid Flow*, pages 1–18, 1969.

[31] D.-Y. Hsieh and M. S. Plesset. On the propagation of sound in a liquid containing gas bubbles. *Physics of Fluids*, 4(8):970, 1961.

[32] T. Jacob. *Évaluation sur modèle réduit et prédiction de la stabilité de fonctionnement des turbines Francis.* PhD thesis, EPFL, Lausanne, 1993.

[33] A. Jenkins. Self-oscillation. *Physics Reports*, 525(2):167–222, 2013.

[34] A. Kashima, P. J. Lee, M. S. Ghidaoui, and M. Davidson. Experimental verification of the kinetic differential pressure method for flow measurements. *Journal of Hydraulic Research*, 51(6):634–644, Dec. 2013.

[35] J. Koutnik, C. Nicolet, G. A. Schohl, and F. Avellan. Overload surge event in a pumped-storage power plant. *23th IAHR Symposium on the Hydraulic Machinery and systems, Yokohama, Japan*, 2006.

[36] J. Koutnik and L. Pulpitel. Modeling of the francis turbine full-load surge modeling. *Testing and Monitoring for Hydro Power Plants*, 1996.

[37] P. Kundur. *Power System Stability And Control*, volume 7. N.J. Balu & M.G. Lauby, New-York, McGraw-hill, 1994.

[38] C. Landry, C. Nicolet, A. Bergant, A. Mueller, and F. Avellan. Modeling of unsteady friction and viscoelastic damping in piping systems. In *26th IAHR Symposium on Hydraulic Machinery and Systems*, Beijing, Chine, 2012.

[39] A. Mueller. *Physical Mechanisms governing Self-Excited Pressure Oscillations in Francis Turbines.* PhD thesis, EPFL, 2014.

[40] A. Mueller, M. Dreyer, N. Andreini, and F. Avellan. Draft tube discharge fluctuation during self-sustained pressure surge:fluorescent particle image velocimetry in two-phase flow. *Experiments in Fluids*, 54:1–11, 2013.

[41] C. Nicolet. *Hydroacoustic Modelling and Numerical Simulation of Unsteady Operation of Hydroelectric Systems*. PhD thesis, EPFL, Lausanne, Switzerland, 2007.

[42] C. Nicolet, S. Alligné, B. Kawkabani, J. Koutnik, J. J. Simond, and F. Avellan. Stability study of francis pump-turbine at runaway. *3rd IAHR International Meeting of the Workgroup on Cavitation and Dynamic Problems in Hydraulic Machinery and Systems*, 2009.

[43] C. Nicolet, J. Arpe, and F. Avellan. Identification and modeling of pressure fluctuations of a francis turbine scale model at part load operation. In *Proceedings of the 22nd IAHR Symposium on Hydraulic Machinery and Systems*, 2004.

[44] M. Nishi, S. Matsunaga, S. Kubota, and Y. Senoo. Surging characteristics of conical and elbow-type draft tubes. *12th IAHR Symposium on hydraulic Machinery and Systems*, pages 272–283, 1984.

[45] M. Nishi, S. Matsunaga, T. Kubota, and Y. Senoo. Flow regimes in an elbow-type draft tube. *11th IAHR Symposium on hydraulic Machinery and Systems, Amsterdam, Netherland*, 38:13–17, 1982.

[46] M. Nishi, X. Wang, M. Okamoto, and S. Matsunaga. Further investigation on the pressure fluctuations caused by cavitated vortex rope in an elbow draft tube. *Cavitation and Gas Fluid Flow in Fluid Machinery and Devices*, pages 63–70, 1994.

[47] N. Otsu. A threshold selection method from gray-level histograms. *IEEE Trans Syst Man Cybern*, 11(285-296):23–27, 1979.

[48] G. Pezzinga. Second viscosity in transient cavitating pipe flows. *Journal of Hydraulic Research*, 6:656–665, 2003.

[49] R. Philibert and M. Couston. Francis turbines at part load. matrix simulating the gaseous rope. *Proceedings of the 19th IAHR Symposium on Hydraulic Machinery and Cavitation, Singapore*, page 441, 1998.

[50] H. J. Rath. Unsteady pressure waves and shock waves in elastic tubes containing bubbly air-water mixtures. *Acta Mechanica 38*, pages 1–17, 1981.

[51] P. Rudolf and A. Skoták. Unsteady flow in the draft tube with elbow, part b - numerical simulation. *Proceedings of the 10th IAHR WG1 meeting, Trondheim, Norway*, 2001.

[52] A. Ruprecht, T. Helmrich, T. Aschenbrenner, and T. Scherer. Simulation of pressure surge in a hydro power plant caused by an elbow draft tube. In *10th International Meeting of the work group on the behaviour of hydraulic machinery under steady oscillatory condition, Trondheim, Norway*, 2001.

[53] A. Sapin. *Logiciel modulaire pour la simulation et l'étude des systèmes d'entraînement et des réseaux électriques*. PhD thesis, EPFL, Lausanne, Switzerland, 1995.

[54] A. Skotak, J. Mikulasek, and L. Lhotakova. Simulation of pressure surge in a hydro power plant caused by an elbow draft tube. In *Proceedings of the 21st IAHR Symposium on Hydraulic Machinery and Systems, Lausanne, Switzerland*, pages 294–311, 2002.

[55] I. standards. *60193: Hydraulic Turbines, Storage Pumps and Pump-Turbines - Model acceptance Tests*. International Electrotechnic Commission, 2nd Edition, 1999.

[56] Y. Tsujimoto, K. Kamijo, and Y. Yoshida. A theoretical analysis of rotating cavitation in inducers. *Journal of fluids engineering*, pages 135–141, 1993.

[57] Y. Tsujimoto, S. Watanabe, K. Kamijo, and Y. Yoshida. A non-linear calculation of rotating cavitation in inducers. *Journal of fluids engineering*, 118:589–594, 1996.

[58] L. v. Wijngaarden. *Heat Mass Transfer 6*. Enschede, The Netherlands: Twente Institute of Technology, 1972.

[59] A. E. Vardy and J. M. B. Brown. Transient turbulent friction in smooth pipe flows. *Journal of Sound and Vibration*, 259(5):1011–1036, Jan. 2003.

[60] A. E. Vardy and K.-L. Hwang. A characteristics model of transient friction in pipes. *Journal of Hydraulic Research*, 29(5):669–684, Sept. 1991.

[61] J. Vítkovský, A. Bergant, A. Simpson, and M. Lambert. Systematic evaluation of one-dimensional unsteady friction models in simple pipelines. *Journal of Hydraulic Engineering*, 132(7):696–708, 2006.

[62] A. B. Wood. *A Textbook of Sound*. G. Bell and Sons Ltd, London, Great Britain, 1941.

[63] E. B. Wylie, V. L. Streeter, and L. Suo. *Fluid transients in systems*. Prentice-Hall, Inc., Englewood Cliffs, New Jersey, 1993.

[64] K. Yamamoto, A. Mueller, A. Favrel, C. Landry, and F. Avellan. Pressure measurements and high speed visualizations of the cavitation phenomena at deep part load condition in a francis turbine. In *27th IAHR Symposium on Hydraulic Machinery and Systems*, Montreal, Canada, 2014.

[65] W. Zielke and H. Hack. Resonance frequencies and associated mode shapes of pressurized piping systems. *Proceedings of the International Conference Pressure Surges, Cranfield, UK*, G1:1–13, 1972.

[66] A. Zobeiri. *Investigations of Time Dependent Flow Phenomena in a Turbine and a Pump-Turbine of Francis Type: Rotor-Stator Interactions and Precessing Vortex Rope*. PhD thesis, EPFL, N°4272, Lausanne, 2009.

Christian Landry

Mechanical engineer
Born in 1985, Swiss citizen
1904 Vernayaz, Switzerland
E-mail : christian.landry@a3.epfl.ch

Education

2011 - 2015 **PhD**
École Polytechnique Fédérale de Lausanne (EPFL), Switzerland

2008 – 2010 **Master of Science MSc** (mechanical engineering)
École Polytechnique Fédérale de Lausanne (EPFL), Switzerland

2005 - 2008 **Bachelor of Science BSc** (mechanical engineering)
École Polytechnique Fédérale de Lausanne (EPFL), Switzerland

Professional Experience

2011 – 2015 **Doctoral assistant –** EPFL Laboratory for Hydraulic Machines (LMH)
Development of a hydroacoustic modeling of a cavitation vortex rope for a Francis turbine based on reduced-scale physical model experiments.

Teaching activities – EPFL Laboratory for Hydraulic Machines (LMH)

- Master courses: Hydraulic turbomachines, acoustic hydrodynamic.
- Bachelor courses: Introduction to turbomachinery
- Coordination of Master projects
- Preparation of exercises and exam sessions

Research Projects – HYPERBOLE ERC/FP7-ENERGY-2013-1-Grant 608532

- Industrial partners: Andritz Hydro, Voith Hydro, Alstom Hydro, Power Vision Engineering Sàrl, INESC Porto
- Academic partners: EPFL-LMH, UPC, University of Stuttgart, University of Applied Science HES SO Valais

2010 (6 months) **Master thesis -** Alstom Power Hydro (Grenoble, France)
Development of a new measurement system to determine the flow velocity field in Francis turbine. The acquisition time was reduced by nine and the accuracy of the measurement data was greatly improved.

Skills and Endorsements

Theory: Hydraulic turbomachinery, Fluid dynamics, Experimental mechanics, Signal processing
Programming: Matlab, C, C++, C#, Delphi

Languages

French	Native proficiency
English	Professional working proficiency
German	Elementary proficiency

Journal papers

C. Landry, A. Favrel, A. Müller, C. Nicolet, and F. Avellan (2014), *Part load cavitation vortex rope in Francis turbines: Experimental determination of local wave speed and bulk viscosity*, Journal of Hydraulic Research, (article under revision)

Conference papers

C. Landry, A. Favrel, A. Müller, C. Nicolet, K. Yamamoto and F. Avellan, *Experimental investigation of the local wave speed in a draft tube with cavitation vortex rope*. 27th IAHR Symposium on Hydraulic Machinery and Systems, Montréal, Canada, September 22-26, 2014

A. Favrel, C. Landry, A. Müller, K. Yamamoto and F. Avellan. *Hydro-acoustic resonance behavior in presence of a precessing vortex rope: observation of a lock-in phenomenon at part load Francis turbine operation*. 27th IAHR Symposium on Hydraulic Machinery and Systems, Montréal, Canada, September 22-26, 2014.

A. Müller, A. Favrel, C. Landry, K. Yamamoto and F. Avellan. *On the physical mechanisms governing self-excited pressure surge in Francis turbines*. 27th IAHR Symposium on Hydraulic Machinery and Systems, Montréal, Canada, September 22-26, 2014.

C. Landry, C. Nicolet, S. Giacomini and F. Avellan. *Influence of the Hydraulic System Layout on the Stability of a Mixed Islanded Power Network.* IOP Conference Series: Earth and Environmental Science, vol. 15, page 052030

C. Landry, C. Nicolet, A. Bergant, A. Müller and F. Avellan. *Modeling of Unsteady Friction and Viscoelastic Damping in Piping Systems.* 26th IAHR Symposium on Hydraulic Machinery and Systems, Beijing, China, August 19-23, 2012.

A. Favrel, C. Landry, A. Müller and F. Avellan. *Experimental Identification and Study of Hydraulic Resonance Test Rig with Francis Turbine operating at Partial Load.* 26th IAHR Symposium on Hydraulic Machinery and Systems, Beijing, China, August 19-23, 2012.

A. Müller, A. Bullani, M. Dreyer, S. Roth, A. Favrel, C. Landry and F. Avellan, *Interaction of a pulsating vortex rope with the local velocity field in a Francis turbine draft tube.* 26th IAHR Symposium on Hydraulic Machinery and Systems, Beijing, China, August 19-23, 2012.

C. Landry, S. Alligné, V. Hasmatuchi, S. Roth, A. Müller and F. Avellan, *Non-Linear Stability Analysis of a Reduced Scale Model Pump-Turbine at Off-Design Operation.* 4th IAHR International Meeting on Cavitation and Dynamic Problems in Hydraulic Machinery and Systems, Belgrade, Serbia, October 26-28, 2011.

A. Müller, S. Alligné, F. Paraz, C. Landry and F. Avellan. *Determination of Hydroacoustic Draft Tube Parameters by High Speed Visualization during Model Testing of a Francis Turbine.* 4th International Meeting on Cavitation and Dynamic Problems in Hydraulic Machinery and Systems, Belgrade, Serbia, October 26-28, 2011.